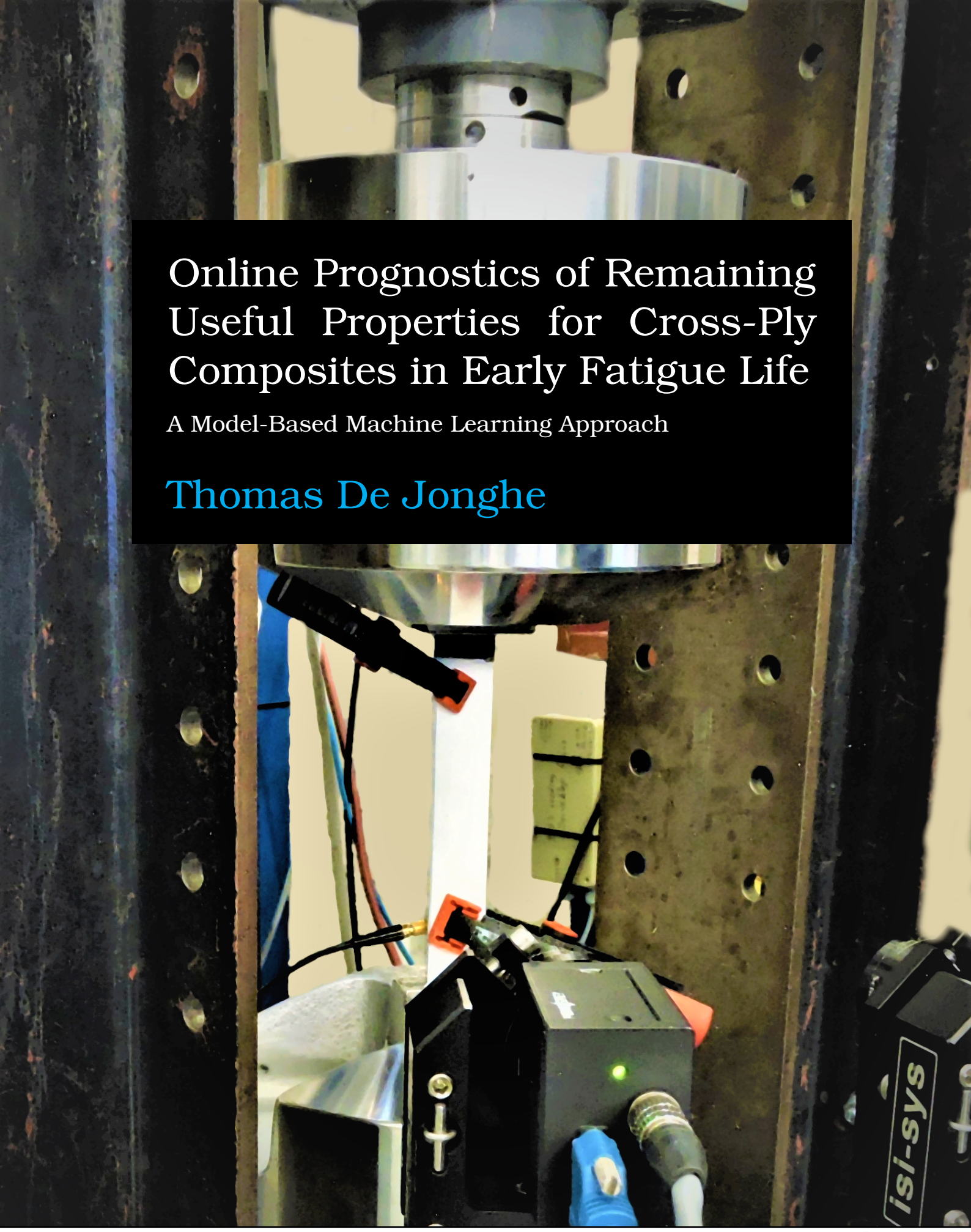

Online Prognostics of Remaining Useful Properties for Cross-Ply Composites in Early Fatigue Life

A Model-Based Machine Learning Approach

Thomas De Jonghe

TU Delft Delft University of Technology

Online Prognostics of Remaining Useful Properties for Cross-Ply Composites in Early Fatigue Life

A Model-Based Machine Learning Approach

Master of Science Thesis

For obtaining the degree of Master of Science in Aerospace Engineering
at Delft University of Technology

Thomas De Jonghe

17 December 2020

Faculty of Aerospace Engineering · Delft University of Technology

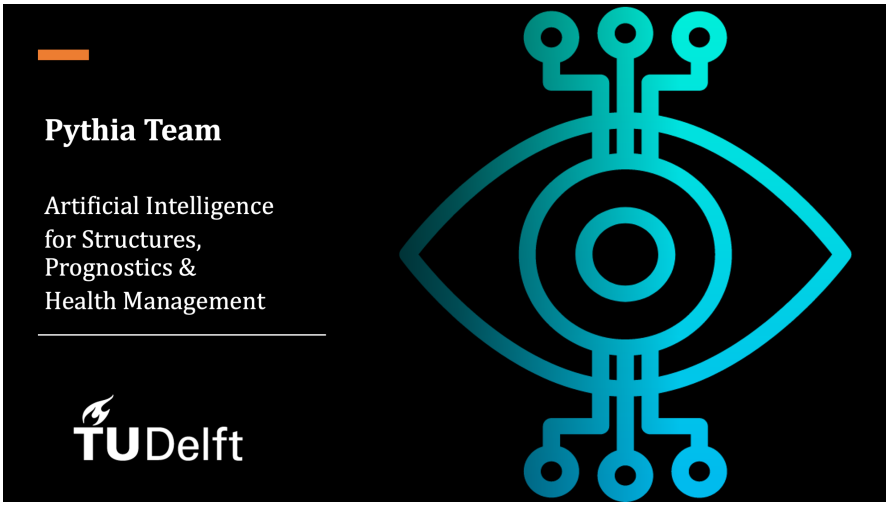

The work in this thesis was supported by Dimitrios Zarouchas and the Faculty of Aerospace Engineering at Delft University of Technology. Their cooperation is gratefully acknowledged.

TU Delft Delft University of Technology

Delft University of Technology
Faculty of Aerospace Engineering
Department of Aerospace Structures and Materials

GRADUATION COMMITTEE

Dated: 17 December 2020

Chair holder:

Dr.Ir. C.D. Rans

Committee members:

Supervisor: Dr.Ir. D. Zarouchas

Dr.Ir. J.E.E. Teuwen

Dr.Ir. B. Chen

Preface

This report is the result of my master thesis at the Faculty of Aerospace Engineering of Delft University of Technology. The thesis, including a literature study, covered a period of approximately 45 weeks starting February 2020 and ending December 2020. It is part of the curriculum to obtain the Master of Science in Aerospace Engineering at Delft University of Technology.

The main purpose of this thesis is to set up a framework, and to investigate the capability of a model-based machine learning model for online remaining useful life and properties prognostics of cross-ply composites in early fatigue life. This includes research in the field of structural health monitoring and (failure) mechanics of composites as well as machine learning and statistics. Different existing techniques and models are reviewed and a particle filtering algorithm is developed. A case study based on the data and phenomenological relations of "Unfolding the Early Fatigue Damage Process for CFRP Cross-Ply Laminates" from Li et al. (2020), a colleague of mine from the Pythia team at Delft University of Technology, is presented as a proof of concept.

I would like to extend my greatest gratitude to my supervisor Dimitrios Zarouchas for guiding me through this thesis in pursuit of a successful result. Furthermore, a distinct acknowledgment goes to Xi Li for the valuable case study dataset and providing additional information on measurement uncertainties. I would also like to thank Robert and Michiel for their fruitful feedback on the draft, and to all other staff members at Delft University of Technology that are providing the resources and services required to effectively work on the thesis at the faculty.

Finally, my sincere gratitude to my parents Peter and Annick, my sister Margot and my girlfriend Emma for their unmatched love, help and support. I am forever beholden to my parents for offering the opportunities that shaped me to who I am. Last but not least, I am very grateful to my family and close friends for always being there for me through thick and thin.

Thomas De Jonghe
Delft, 17 December 2020

Abstract

High performance continuous fiber-reinforced composites are becoming increasingly important in the aerospace industry. In these structures, internal damage is often created and propagated throughout the lifetime, having a negative impact on the structural properties. In order to allow for condition-based maintenance, there is a need for reliable prognostics to predict future damage states. Therefore, a model-based machine learning approach is developed in this thesis to perform prognostics of the remaining useful life (RUL) and remaining useful properties (RUP) of cross-ply composites to end-of-early-fatigue-life (EOEFL). In-situ transverse matrix crack density and dynamic stiffness data are available, as well as offline delamination ratio and damage induced stiffness degradation data. To account for the multicausality and non-linearity in stiffness degradation, the evolution of cracks and delaminations is modeled using separate phenomenological relations that are pre-trained with high variance using non-linear least squares (NLS) on a separate training set. These damage properties are then combined into a normalized stiffness prediction using NLS pre-trained phenomenological relations that express the induced stiffness degradation for each of the aforementioned properties. A particle filter (PF) trains the model parameters, initialized in a high variance uniform distribution, for the phenomenological models in real-time (i.e. online). This is done with the in-situ crack density and normalized stiffness measurements of the testing specimen only. A random walk on the model parameters, which declines towards EOEFL with a given rate of convergence, is added to allow for continuous adaptivity. By propagating each particle to future states beyond the online time step in the PF, the prognostics are obtained. This encompasses the RUP and RUL to EOEFL using a weighted sum of the particles. After applying this methodology to the case study data, it is concluded that the potential of PF to offer adaptivity required for RUP prognostics of composites is identified, definitely for damage properties showing early characteristic behavior. However, reliable RUL estimation to EOEFL with the methodology set out in this thesis remains difficult. Especially the stiffness degradation model and the failure criterion for EOEFL generate difficulties. Therefore, a promising recommendation would be to combine similar phenomenological relations to end-of-life for crack and delamination growth with an alternative stiffness model. A feasible approach would be to train a surrogate model on synthetic data generated with finite element modeling simulations. Finally, a sensitivity analysis is done on three PF hyperparameters: sample size, threshold effective sample size, and rate of convergence. The first shows that a minimum sample size can be distinguished after which no improvement occurs when the sample size increases. The second indicates a 'sweet spot' that balances the sample impoverishment and weight degeneracy drawbacks. The latter makes it plausible that a moderate rate of convergence is preferable.

Contents

List of Tables

List of Figures

List of Abbreviations

Abbreviation	Definition
CBM	Condition-Based Maintenance
CDS	Characteristic Damage State
CFRP	Carbon Fiber-Reinforced Polymer
CRA	Cumulative Relative Accuracy
DIC	Digital Image Correlation
EOEFL	End-of-Early-Fatigue-Life
EOL	End-of-Life
GL	Gauge Length
IPR	Inter-Percentile Range
IS	Interactive Scheme
MAPE	Mean Absolute Percentage Error
MCMC	Markov Chain Monte Carlo
NIS	Non-Interactive Scheme
NLS	Non-linear Least Squares
pdf	Probability Density Function
PF	Particle Filter(ing)
PI	Prediction Interval
RMAD	Relative Median Absolute Deviation
RMAD*	Target Relative Median Absolute Deviation for Random Walk
RMSE	Root Mean Squared Error
RUL	Remaining Useful Life
RUP	Remaining Useful Properties
SHM	Structural Health Monitoring
SIS	Systematic Importance Sampling
SIR	Systematic Importance Resampling
SMC	Sequential Monte Carlo
SSE	Sum of Squared Errors
UD	Unidirectional
UTS	Ultimate Tensile Strength

List of Symbols

Latin Symbols

Symbol	Definition
a	Phenomenological model parameter for relation ρ vs. N
b	Phenomenological model parameter for relation ρ vs. N
c	Phenomenological model parameter for relation ρ vs. N
d	Phenomenological model parameter for relation d_r vs. N
d_r	Delamination ratio
D	Total stiffness degradation of stage I
D_{del}	Delamination induced stiffness degradation of stage I
D_{tc}	Transverse crack induced stiffness degradation of stage I
e	Phenomenological model parameter for relation d_r vs. N
E_I	Longitudinal dynamic stiffness at the end of stage I
E_m	Error between RUL prediction and actual RUL
$\frac{E_N}{E_0}$	Normalized longitudinal stiffness
$\frac{E_N}{E_0}$	Normalized longitudinal stiffness measurement for updating
E_n	Longitudinal dynamic stiffness at time step n
$E_{initial}$	Longitudinal dynamic stiffness at time step 0
f	Phenomenological model parameter for relation d_r vs. N
$\boldsymbol{F}$	Failure vector
g	Phenomenological model parameter for relation d_r vs. N
h	Phenomenological model parameter for relation D_{tc} vs. ρ
i	Phenomenological model parameter for relation D_{tc} vs. ρ
I_r	Inter-laminar crack ratio
j	Phenomenological model parameter for relation D_{del} vs. d_r
k	Phenomenological model parameter for relation D_{del} vs. d_r
l	Time steps ahead in PF prognostics process
$L_{l,1}$	Total length of inter-laminar cracks on left-hand interface 1
$L_{l,2}$	Total length of inter-laminar cracks on left-hand interface 2
$L_{r,1}$	Total length of inter-laminar cracks on right-hand interface 1

$L_{r,2}$	Total length of inter-laminar cracks on right-hand interface 2
m	Phenomenological model parameter for relation $\frac{E_N}{E_0}$ vs. D
n	Time step in PF filtering process
N	Number of fatigue cycles
N_{eff}	Effective sample size
N_s	Number of samples in a particle filter
$N_{threshold}$	Threshold effective sample size to trigger resampling
P^*	Rate of convergence for random walk shrinkage
q_ρ	Normally distributed measurement error of $\bar{\rho}$
$q_{\frac{E_N}{E_0}}$	Normally distributed measurement error of $\frac{\bar{E_N}}{E_0}$
$\boldsymbol{q}$	Measurement error vector $\left[\sigma_{q,\rho}, \sigma_{q,\frac{E_N}{E_0}}\right]$
t	Time step
$\boldsymbol{t}$	Transition function x_n
$v_{D_{del}}$	Normally distributed model error of D_{del} prediction
v_{d_r}	Normally distributed model error of $\Delta\rho$ prediction
$v_{D_{tc}}$	Normally distributed model error of D_{tc} prediction
v_ρ	Normally distributed model error of Δd_r prediction
$\boldsymbol{v}$	Model error vector $[\sigma_{v,\rho}, \sigma_{v,d_r}, \sigma_{v,D_{tc}}, \sigma_{v,D_{del}}]$
w	Normalized weight
$\hat{w}$	Un-normalized weight
$\boldsymbol{w}$	Weight vector
$\boldsymbol{x}$	Damage state vector $\left[\rho, d_r, \frac{E_N}{E_0}\right]$
$\boldsymbol{y}$	Measurement vector $\left[\bar{\rho}, \frac{\bar{E_N}}{E_0}\right]$
$\boldsymbol{z}$	State vector $[\boldsymbol{x}, \boldsymbol{\theta}, \boldsymbol{v}]$

Greek Symbols

Symbol	Definition
$\bar{\epsilon}_{xx}$	Average axial strain measured by DIC
ΔN	Progression of cycles for a single time step
$\Delta\rho$	Growth of transverse matrix crack density over ΔN cycles
Δd_r	Growth of delamination ratio over ΔN cycles
$\boldsymbol{\theta}$	Model Parameter vector $[a, b, c, d, e, f, h, i, j, k, m]$
ν	In-situ measured Poisson ratio of cross-ply outer ply
$\boldsymbol{\xi_n}$	Random walk vector
ρ	Transverse matrix crack density of cross-ply 90° sub-laminate
$\bar{\rho}$	Transverse matrix crack density measurement for updating
σ	Standard deviation of normal distribution
σ_{xx}	Axial stress measured by fatigue machine

Chapter 1

Introduction

High performance fiber-reinforced composites are becoming increasingly important in the aerospace industry. These lightweight structures offer the potential to reduce airframe weight, which in turn leads to fuel savings. Next to this, manufacturing costs decrease with new composite manufacturing technologies being developed over the years (Mangalgiri, 1999; Knab et al., 2018). Apart from fuel economy, composites offer advantages with superior corrosion resistance compared to metals (Shufeng et al., 2015). However, there are downsides to the use of composites. Most importantly, internal damage can be created and propagated throughout the lifetime, which has a negative impact on the structural properties (Khan et al., 2019).

Different maintenance strategies exist to guarantee airworthiness of the structural component, thus to overcome the downside of internal damage. Traditionally, corrective maintenance is planned with fixed time intervals based on the experience of technicians (Marseguerra et al., 2002). In contrast to corrective maintenance, condition-based maintenance facilitates dynamic planning of maintenance using structural health monitoring measurements. Because condition-based maintenance needs real-time information on the damage state and expected damage evolution, prognostic modeling is required to estimate future damage states along with the remaining useful life up to a pre-defined critical damage level (Farrar and Lieven, 2006). For this purpose, Elattar et al. (2016) distinguish four types of prognostics: a reliability-based, physics-based, data-driven, and hybrid approach. While these approaches have been used in numerous industrial applications, research in the field of prognostics for composites is still rather limited (Eleftheroglou et al., 2018).

Lately, Chiachío et al. (2015a), Chiachío et al. (2015b) and Corbetta et al. (2018) made use of particle filtering (model-based approach) to update model parameters of physics-based damage models with structural health monitoring measurements to predict the end-of-life of composites. These models express damage evolution between states by a modified Paris law for composites and shear lag models. On the other hand, purely data-driven methodologies use information from observed data, on which model training is performed to predict the future states by identifying degradation patterns. Data-driven methodologies can be classified

into two major groups: the artificial intelligence approaches (i.a. neural networks and fuzzy logic) and statistical approaches (i.a. gaussian process regression, least squares regression, support vector machines and hidden Markov models). As a downside, these methods require a larger number of observed training data to provide sufficient accuracy (Kim et al., 2016).

Next to the model-based and data-driven approaches, a third hybrid category exists to combine the advantages and to alleviate the drawbacks of both. Recently, Cadini et al. (2019) developed a neural network (data-driven approach) embedded within a particle filter (model-based approach), which was showcased on aeronautical metallic stiffened skin panels. This allows sequential updating of the remaining useful life prediction model every time structural health monitoring data become available. While this approach eliminates the need for a large set of training data and a reliable physics-based model, it suffers from volatile behavior and divergence of confidence intervals close to end-of-life. However, as Eleftheroglou (2020) identifies, the proposed methodology in Cadini et al. (2019) can be valuable for prognostics of composites once more reliable phenomenological models become available.

With the very recent introduction of phenomenological relations based on experimental observations by Li et al. (2020) describing fatigue damage accumulation in the early fatigue life of cross-ply carbon fiber-reinforced polymers, new opportunities arise. These phenomenological relations also describe how both transverse matrix cracking and delaminations contribute to the damage accumulation process. Where one first believed that damage in the early fatigue life of composites, often referred to as stage I, is dominated by matrix crack formation and propagation (Jollivet et al., 2013), the recent observations show that in fact delamination is responsible for a larger stiffness degradation than transverse matrix cracks in this stage. Considering the significant stiffness degradation in early fatigue life, it is of great interest to emphasize at first on the prognostics of remaining useful properties in early fatigue life, paving the way for future extensions to predict the actual remaining useful life up to failure using model-based methodologies that encapsulate the damage accumulation process. Therefore, this thesis aims at developing a model-based machine learning algorithm for remaining useful life prognostics of cross-ply continuous fiber-reinforced composites in early fatigue life.

1.1 Research Objective and Research Questions

Given the research gaps and opportunities identified in the introduction, the objectives and research questions of this thesis can be specified. The research objective is formulated as such:

Research Objective

The research objective of this thesis is to develop a model-based machine learning model for prognostics of the remaining useful life and properties of cross-ply composites in early fatigue life. This model-based approach shall allow the construction of a reliable model without the availability of a large dataset nor a reliable physics-based model. Doing so, the machine learning model shall be able to predict future states, keeping in mind multicausality of stiffness degradation, while offering real-time adaptivity of the model parameters based on information from multiple structural health monitoring measurements. Throughout the project, special attention shall be paid to introducing, propagating and monitoring uncertainties to improve validity of the model.

A dataset collected and analyzed by Li et al. (2020), a colleague from the Pythia team at Delft University of Technology, is available as case study data for this research. This dataset consists of seven cross-ply $[0_2/90_4]_s$ carbon-fiber reinforced polymer specimens. Tests were ended at 10^5 cycles, which is well beyond early fatigue life. Every 500 cycles, the specimen was unloaded and information on the crack density, the delamination ratio and the dynamic stiffness was extracted. Using this dataset, and keeping in mind the research objective statement, research questions can be formulated. The novel machine learning model shall be constructed and assessed using the available case study data and the following identified research question and sub-questions:

Research Question

To what extent can the remaining useful life and properties of cross-ply composites in early fatigue life be predicted using online sequential training of phenomenological model(s) embedded into a particle filter?

This research question encompasses the following sub-questions:

- Which measurable damage properties can be used to construct phenomenological relations for damage evolution of composites in early fatigue life?
- How can the multicausality of stiffness degradation in early fatigue life be accounted for in a particle filtering algorithm?
- How well does the model behave on case study data to predict the remaining useful life in terms of prognostic evaluation metrics (precision, root mean squared error, mean absolute percent error, cumulative relative accuracy and convergence)?
- Which influence do the input parameters of the particle filtering algorithm have on the model performance?

The 'to what extent' in the research question is not an absolute measure, but it encompasses a qualitative analysis for each of the sub-questions. The qualitative answers to the research questions are supported by quantitative results of the case study presented in this thesis. Therefore, in the case study methodology and the case study results, the sub-questions are dealt with along the way. In the conclusions, each question is reflected on including the most relevant details.

1.2 Report Structure

This report elaborates on the research objective, and answers the research (sub-)questions using the following report structure:

- Chapter 2 introduces the general background of this thesis, along with key findings and recent developments in the field of composites and machine learning. First, the properties and damage evolution of continuous fiber-reinforced composites are discussed. After this, the principles behind usage monitoring and structural health monitoring are elaborated upon. Finally, background is provided on the fundamentals and applications of model-based machine learning.
- Chapter 3 familiarizes the reader with the case study data from Li et al. (2020) used throughout the next chapters. The properties and manufacturing processes are elaborated upon for these specific specimens. Additionally, the methods used for gathering structural health monitoring data as well as the damage properties recorded in the dataset are introduced.
- Chapter 4 establishes the methodology to construct the model-based machine learning model for this research. First, the phenomenological relations and pre-training of model parameters are focused on to develop a state transition model for the particle filter. Following on this, the three major building blocks of the particle filtering algorithm for adaptive prognostics are discussed: initialization, filtering and prognostics. A last section in this chapter focuses on the evaluation of performance of these models when applied to a case study.
- Chapter 5 details the results of the case study showcasing the model on the case study data. Additionally, the results of the remaining useful life and properties prognostics of cross-ply continuous fiber-reinforced composites in early fatigue life are discussed. Here, the results for the strong performing specimen 1-4 and the weak performing specimen 2-2 are detailed extensively. Lastly, the sensitivity of input parameters on model performance is investigated.
- Chapter 6 concludes this thesis by pointing out the most significant findings as well as restating answers to the research questions. Additionally, recommendations for future research are formulated.

Chapter 2

Literature

This chapter introduces background information for this thesis, along with recent developments in the field of continuous fiber-reinforced composites and machine learning. First, the properties and damage evolution of composites are discussed in section 2.1. After this, section 2.2 focuses on usage monitoring and structural health monitoring (SHM) for prognostics. It is important to know that SHM techniques do not measure damage directly. Finally, in section 2.3, background is provided on fundamentals of model-based machine learning.

2.1 Continuous Fiber-Reinforced Composites

Continuous fiber-reinforced composites, as considered in this thesis for high-performance applications, consist of two or more phases, for which the combined performance and properties can be superior to the characteristics of each of the constituents individually. Their backbone exists of fibers having a high length-to-diameter ratio (Daniel and Ishai, 2006). First, the properties of these composites are discussed with their constituents and imperfections (subsection 2.1.1). A key take-away of this subsection is that the complexity and high number of interactions make composite failure a stochastic process. Subsequently, fatigue damage accumulation is elaborated upon in subsection 2.1.2, in which it becomes clear that fatigue damage accumulation is a multi-scale phenomenon.

2.1.1 Structural Properties

Continuous fiber-reinforced composites consist of two separate phases on the microscale level: a dispersed phase with continuous fibers and a polymer matrix phase. As Figure 2.1 shows, both phases are combined to a composite ply (mesoscale level). Within the composite, the main purpose of the matrix phase is to bind the fibers together, and to distribute applied stresses among the fibers (Callister and Rethwisch, 2014). However, a single composite ply barely offers sufficient strength for high-end applications. Therefore, multiple composite plies are combined into a laminate (macroscale level). The number of plies and their orientation makes it possible to tailor laminate properties based on the structural requirements.

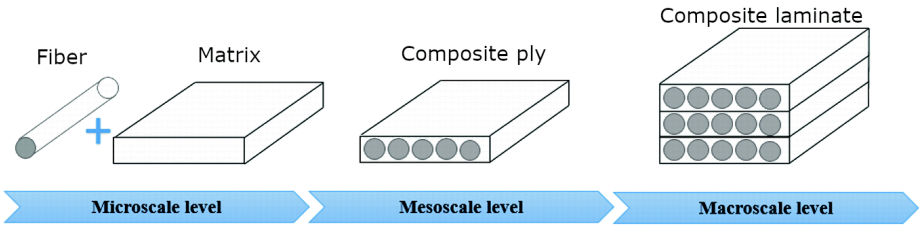

Figure 2.1: Schematic representation of a continuous fiber-reinforced composite and its constituents from micro- to macroscale level (Ageyeva et al., 2019).

Dispersed Phase: Fibers

The fibers in continuous fiber-reinforced composites are the load-carrying elements. In high-performance composites, glass fibers and carbon fibers are commonly used. The glass fibers have a relatively low cost and still offer considerable strength. However, their low specific stiffness and susceptibility to surface flaws makes them less suitable as structural components for advanced applications. Therefore, carbon fibers are commonly preferred as they retain excellent mechanical properties such as a high specific stiffness and strength at higher temperatures, along with good chemical resistance. One should note that a wide variety of carbon fibers with differing mechanical and physical characteristics exists, which gives the possibility to tailor properties to the needs for a specific application (Callister and Rethwisch, 2014; Pusch and Wohlmann, 2018). It is clear that a stiffer fiber prevents damage from initiating prematurely. This is the direct effect of a smaller allowed deformation of the matrix. However, fatigue behavior is not only dependent on the type of fiber, and must be assessed on different levels (Wicaksono and Chai, 2013).

Matrix Phase: Polymers

The matrix phase in continuous fiber-reinforced composites binds the fibers together and distributes applied stresses among the fibers. This means that little load is carried by the matrix phase itself, but that its function is essential to activate the load-bearing fibers. Aside from transferring loads, the matrix is essential to prevent the occurrence of surface damage on the fibers, which could lead to crack formation. Additionally, the matrix phase is very ductile compared to the dispersed phase, serving as a barrier for propagation of cracks between fibers until a cluster of adjacent fibers fails. The choice of matrix depends partly on the aforementioned stiffness considerations, but also on the properties of the interface when combined with a select fiber (Callister and Rethwisch, 2014). As mentioned previously, a higher resin ductility acts as a barrier for crack propagation between fibers. On the other hand, Wicaksono and Chai (2013) mentions that a higher resin toughness results in an increased inter-laminar fracture toughness to resist delamination.

Composite Laminate: Stacking Sequences

Composite plies consisting of the selected matrix and fiber type occur frequently as unidirectional (UD) plies, with fibers aligned in one direction. Given the ply properties and the required laminate properties, the composite laminate is constructed by stacking in a sequence

of ply orientations relative to a reference axis (Kassapoglou, 2013). Four categories, illustrated in Figure 2.2, are commonly used laminates: UD, cross-ply, angle-ply and multi-directional.

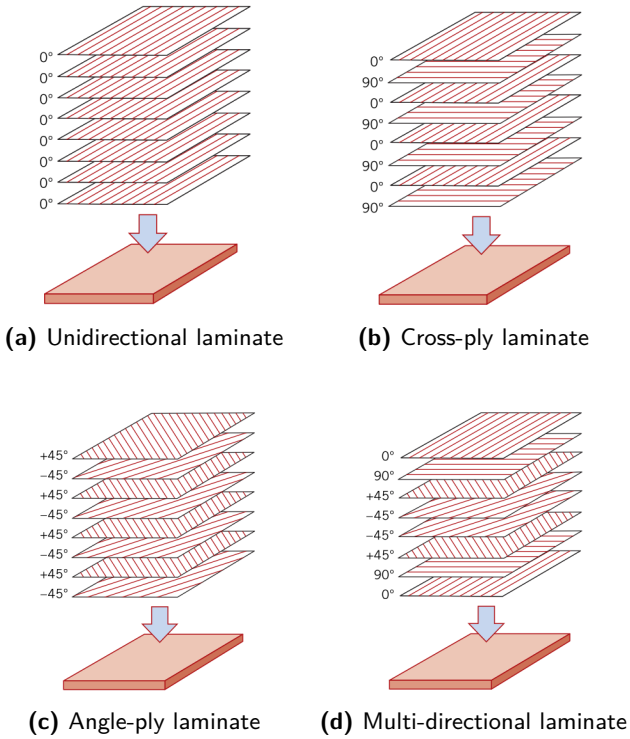

(a) Unidirectional laminate **(b)** Cross-ply laminate

(c) Angle-ply laminate **(d)** Multi-directional laminate

Figure 2.2: Illustration of composite laminate stacking sequences (Callister and Rethwisch, 2014).

In this research, the focus is on cross-ply composites as displayed in Figure 2.2b. These laminates are composed of plies oriented at 0° and 90°. Symmetric cross-ply laminates have decoupling between in-plane loading and out-of-plane deformation, while anti-symmetric cross-ply laminates have coupling between in-plane loading and out-of-plane deformation (Daniel and Ishai, 2006). For both cases, extension-shear, bending-twist and extension-twist coupling is not existent (Kollár and Springer, 2003). Specific effects of this lay-up on damage initiation and accumulation are discussed in more detail in subsection 2.1.2.

Imperfections

While classical laminate theory can predict mechanical properties of composite, and while fatigue life diagrams can be used as a baseline to assess properties of a composite based on its constituents, uncertainty in the exact constituent properties causes significant scatter. Talreja (2003) describes composite failure as a rather stochastic process in comparison to metal failure due to its complexity and the number of interactions. Scatter can be broken down into intrinsic sources and extrinsic sources.

Extrinsic scatter partly deals with the uncertainty of measurements. SHM measurements also have an uncertainty associated, which is discussed in more detail with explanatory axioms in section 2.2 and specifically for machine learning for prognostics in subsection 2.3.3.

Additionally, environmental conditions such as temperature, moisture and corrosion have an impact on the fatigue life of composites (Wicaksono and Chai, 2013). On the other hand, intrinsic scatter arises due to the variability and uncertainty in micro-, meso- and macroscale properties of continuous fiber-reinforced composites. This type of variability is unavoidable and is dependent on the manufacturing of the laminate as well as processing and shaping of the test specimen. Commonly encountered intrinsic defects include porosity, in-homogeneous fiber volume fractions, fiber misalignment and fiber-matrix debonding. Additionally, residual stresses can be present after the manufacturing process influencing delamination behavior due to interference with global stresses while testing (Brunner, 2018).

Both sources of uncertainty in composites are often mitigated by adopting safety factors. While this avoids unexpected failures, it also results in costly and unnecessary conservatism as Chiachío Ruano and Rus Carlborg (2014) stress. Therefore, adaptive prognostics are required to account for the inherent level of variability in the damage and failure behavior of composites.

2.1.2 Fatigue Damage Initiation and Accumulation

Despite the favorable mechanical properties for high-end applications, composites are prone to internal damage on ply and intra-ply level. Therefore, it is important to predict the evolution and/or accumulation of common damage parameters on the fatigue life of composites to prevent macroscopic failure (McCarthy and Vaughan, 2015). Tension-tension fatigue loading is the most studied phenomenon for composites, for which buckling does not occur. The general degradation of cross-ply composites under tension-tension loading is therefore elaborated upon first, after which the major differences with tension-compression loading are introduced. Due to the complexity introduced by non-linear and brittle behavior under compression-compression loading, this is considered out of scope for this thesis (Ribeiro et al., 2011).

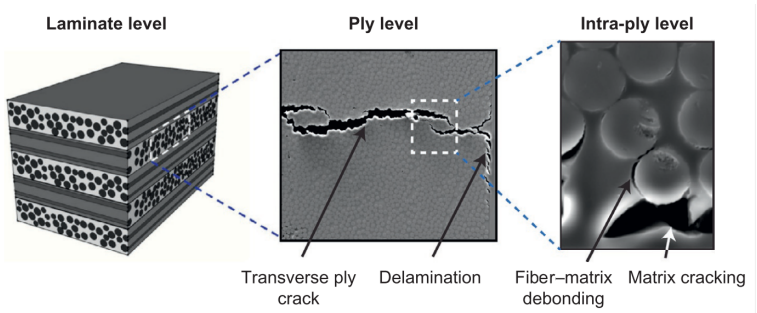

Figure 2.3: Multi-scale nature of delamination as a result of intra-ply failure mechanisms (McCarthy and Vaughan, 2015).

Tension-Tension Fatigue Loading

Considering tension-tension loading in cross-ply composites, fiber-matrix debonding and matrix micro-cracking are commonly studied. As shown on the right in Figure 2.3, fiber-matrix debonding and matrix micro-cracking are initiated on the intra-ply level. Under persistent loading, the created intra-ply damage evolves to transverse ply cracks on ply level.

Eventually, McCarthy and Vaughan (2015) describe the occurrence of delamination as a result of stress concentrations at the transverse crack tips on ply level. However, damage evolution in composites is highly dependent on the exact lay-up, mechanical properties and loading conditions (Loutas et al., 2017). The following load levels are distinguished by Giurgiutiu (2020), each showing different damage accumulation to failure:

- **Low cyclic loading:** In case of sufficiently low cyclic loading, matrix cracking occurs, but does not propagate once reaching the fiber-matrix interface. Therefore, no additional fracture surfaces appear and the lifetime is determined by the fatigue life of the fibers.
- **Average cyclic loading:** At higher cyclic loading, if a matrix crack reaches the fiber-matrix interface, damage is propagated to other interfaces with two mechanisms. The first involves a high stress concentration at the matrix crack tip reaching the fiber, which leads to fiber breakage and a larger crack. The second involves a lower stress concentration, where interfacial (fiber-matrix) debonding occurs along the interface. As a result of the propagated intra-ply damage, stress concentrations between plies increase significantly in areas with a large degree of matrix cracking, leading to local delaminations. After the presence of delaminations, damage grows to macroscopic failure.
- **High cyclic loading:** For high cyclic loading, meaning close to ultimate strength, fiber breakage will happen early in the lifetime due to statistical spread in fiber strength. Once fibers fail, load redistribution among fibers propagates damage to other fibers until large cracks are present leading to macroscopic failure.

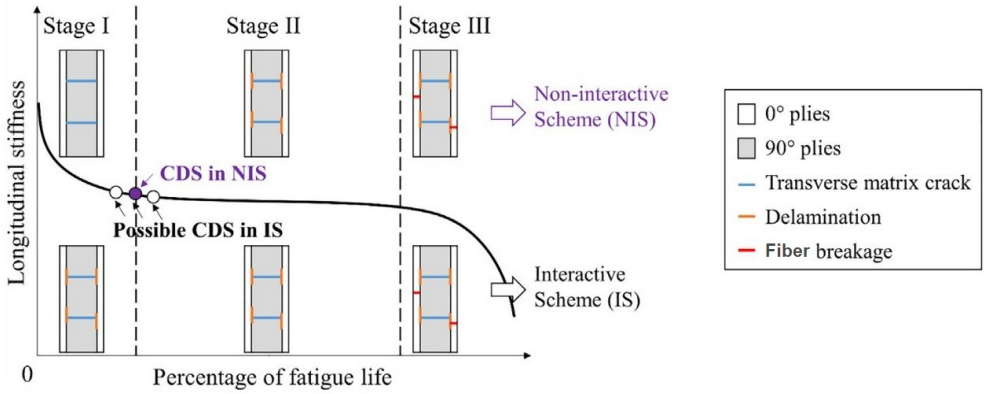

Figure 2.4: Damage accumulation of a cross-ply composite subjected to cyclic loading (Li et al., 2020).

When a composite is subjected to average cyclic loading with the aforementioned damage mechanics, three stages are distinguished. These are observable in Figure 2.4 with the accompanying longitudinal stiffness degradation. The different stages are defined below along with their corresponding damage accumulation behavior:

- **Stage I:** This stage is often referred to as early fatigue life, which is very recently studied by Li et al. (2020) on CFRP cross-ply composites. Keeping in mind the new insights and considerable stiffness degradation (about 8-11%), the focus of this thesis on prognostics

in stage I. Where one first believed that damage in the early fatigue life of composites is dominated by matrix crack formation and propagation (Jollivet et al., 2013), recent observations by Li et al. (2020) show that in fact delamination is responsible for a larger stiffness degradation than transverse matrix cracking. This is attributed to the observed linear increase in stiffness degradation due to matrix cracking, compared to a growing trend up to a threshold in stiffness degradation due to delamination. The findings are quantified in more detail in chapter 3 and are used as phenomenological model throughout the case study to perform prognostics in early fatigue life.

The characteristic damage state (CDS) defines the end of stage I (Giurgiutiu, 2020). Ideally, in case of damage models without interaction, CDS would be exactly at matrix crack saturation. At this point, the crack spacing becomes small enough to eliminate load transfer from fibers to matrix through shear, meaning no additional cracks are created. However, given the introduced interaction between off-axis matrix cracks and delamination, CDS can either belong to stage I or stage II as shown in Figure 2.4. Therefore, stage I to stage II transition is defined as the plateau region in $E_N/E_0(N)$.

- **Stage II:** The majority of the composite life is described by stage II, which can be identified as a plateau region in the longitudinal stiffness degradation as visible in Figure 2.4. In this stage of the composite fatigue life, debondings and matrix cracks line up causing delaminations along the inferfaces between plies (Eleftheroglou, 2020).
- **Stage III:** Apart from delaminations, fiber bundles fail more often in stage III and accelerate the induced damage. This is visible in a sudden drop in longitudinal stiffness in Figure 2.4, which eventually leads to macroscopic failure (Eleftheroglou, 2020).

Tension-Compression Fatigue loading

The aforementioned damage behavior is valid for tension-tension loading. However, in-service composites also deal with tension-compression loading. This type of loading is known to be deteriorate more than tension-tension fatigue with rapid degradation and a shorter fatigue life. This is explained by the compressive load cycle that is more prone to cause delamination due to out-of-plane buckling once a transverse crack occurs in the composite (Figure 2.5b). Additionally, similar to tension-tension loading, adjacent plies suffer from fiber breakage when subjected to tensile load cycles (Figure 2.5a) (Gamstedt and Sjögren, 1999).

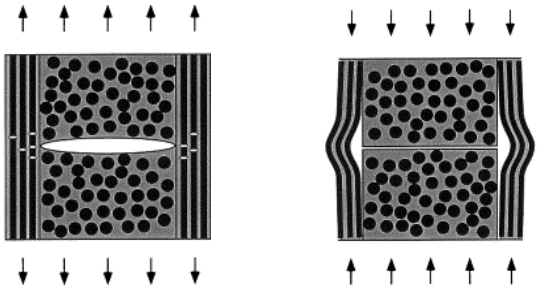

(a) Tensile fiber breakage **(b)** Compressive delamination

Figure 2.5: Illustration of composite damage under tension-compression loading (Gamstedt and Sjögren, 1999).

2.2 Damage Prognostics for Composites

As Farrar and Lieven (2006) identify, SHM will be integrated increasingly into damage prognostics. This means that, apart from assessing the current state of a system, prognostics of the remaining useful life (RUL) in view of condition-based maintenance (CBM) can be done. Such online RUL predictions are directly associated to future damage states, also referred to as remaining useful properties (RUP) in this thesis. Given the complex damage evolution of continuous fiber-reinforced composites due to multi-scale influences (section 2.1), a reliable model for online RUL and RUP prognostics of composites is still nonexistent. It is the scope of this thesis project to investigate a machine learning approach, for which the damage state of the composite is used as an input. The damage prognostics process consists of three main pillars: usage monitoring, SHM and the prognostics itself (Farrar and Lieven, 2006). These parts are dealt with in the upcoming subsections respectively.

2.2.1 Usage Monitoring

Usage monitoring comprises the process of obtaining operational data about the system or structure. This includes observations such as environmental conditions, and observations of operational variables (Farrar and Lieven, 2006). The latter could include, in case of aircraft, take-off/landing weights etc. On a laboratory scale, this process remains limited to capturing environmental conditions (i.a. temperature) and the pre-defined loading conditions (i.a. frequency, stress ratio etc.) during fatigue testing. Specifically in this thesis, constant amplitude loading is applied as explained in chapter 3. This means that the focus will rather be on integrating SHM information in prognostics than on usage monitoring.

2.2.2 Structural Health Monitoring

SHM is defined by Derriso et al. (2016) as automated methods for determining adverse changes in the integrity of mechanical systems. The purpose of an SHM system is to automatically assess the capability of a composite structure to serve its function in real-time. SHM techniques allow to capture the damage state at different levels in real-time, ranging from laminate to intra-ply level, making it possible to detect, localize, and assess damage (Hamdan et al., 2019; Ghoshal et al., 2000). However, no matter which SHM technique is used, uncertainties remain in the measurements as well as the structure. Therefore, one shall be aware of the following selected axioms of SHM proposed by Worden et al. (2007):

- **Axiom 1:** "All structures have inherent flaws or defects."
- **Axiom 2:** "The assessment of damage requires a comparison between two system states."
- **Axiom 3:** "Identifying the existence and location of damage can be done in an unsupervised learning mode, but identifying the type of damage present and the damage severity can generally only be done in a supervised learning mode."
- **Axiom 4a:** "Sensors cannot measure damage. Feature extraction through signal processing and statistical classification is necessary to convert sensor data into damage information."

- **Axiom 4b:** "Without intelligent feature extraction, the more sensitive a measurement is to damage, the more sensitive it is to changing operational and environmental conditions."
- **Axiom 6:** "There is a trade-off between sensitivity to damage of an algorithm and its noise rejection capability."

Axiom 1 indicates the need for SHM techniques to capture inherent flaws and defects, which have been discussed in subsection 2.1.1. This could include voids on macroscale level, down to impurities on the microscale level. Without reliable online SHM techniques in combination with prognostics to perform CBM, a safety factor, which depends on the manufacturing process, is applied to include potential defects for certification purposes (EASA, 2017). Where inherent flaws cause intrinsic scatter, axiom 4 and 6 stress the presence of noise on sensor measurements (extrinsic scatter). When doing prognostics, it is important to be able to quantify these uncertainties for the SHM technique used in specific operational conditions. Four different damage features can be extracted: damage detection and localization, and damage type and severity. From these categories, the first two can be done using unsupervised learning, while the others shall be done with a supervised learning approach as suggested by axiom 3. In case of composites, the focus would be to detect delaminations and transverse matrix cracks in order to predict damage accumulation (Tibaduiza et al., 2018). On a macrosale level, the stiffness of a composite structure can be measured indirectly using for instance digital image correlation (DIC). In subsection 2.3.3, it is discussed how the aforementioned measurement uncertainties and additional uncertainties can be accounted for when doing RUL prognostics.

2.2.3 Prognostics

With the usage monitoring data and SHM data, one can move to prognostics of the RUP and RUL of composite structures. However, a critical piece of information is future operational and/or loading conditions, which are often unknown. These future loading conditions can therefore be estimated using future loading modeling tools. In that respect, Farrar and Lieven (2006) mention that state-space representations are a feasible option to track previous loading and to predict future loading. In this thesis, constant amplitude loading will be assumed, eliminating the need for a dedicated model for future loading conditions. This means the focus is rather on the use of online SHM measurements to adapt underlying phenomenological model parameters that describe damage evolution in composite structures. However, it is important to support state-space usage monitoring information and forecasting in the presented framework. In that respect, particle filtering (PF) shows great potential to capture aforementioned uncertainties, related to composite damage evolution, in a state-space model. More background information on model-based machine learning is therefore provided in section 2.3.

2.3 Machine Learning for Prognostics

As mentioned in section 2.2, it is not sufficient to assess only the present capability of a composite structure to serve its function, but it is also required to make prognostics of the RUL in view of CBM. For that purpose, PF has recently been used by Chiachío et al. (2015a), Chiachío et al. (2015b) and Corbetta et al. (2018) to ensure adaptivity of model parameters for physics-based damage models based on SHM measurements to estimate end-of-life (EOL) of composites. Via an updated Paris law for composites and shear lag models, these approaches express damage evolution between states. On the other hand, solely data-driven methodologies use data from model training carried out on observed data through detection of deterioration trends to forecast future states. However, a drawback of these methods is that they require a greater number of observed data (Kim et al., 2016).

A hybrid model that exists of a neural network (data-driven approach) embedded inside a PF (model-based approach) was recently developed by Cadini et al. (2019), which was displayed on aeronautical metallic stiffened skin panels. This approach combines the adaptivity of model parameters from PF with the predictive capabilities of a neural network. Each time SHM data become available, sequential updating of the RUL prognostics model is done. Although the need for a large collection of training data and a reliable physics-based model is removed by this method, it suffers from unpredictable behavior and confidence interval divergence close to EOL. However, as Eleftheroglou (2020) describes, more reliable phenomenological models would make the suggested approach by Cadini et al. (2019) useful for prognostics of composites.

With the very recent introduction of phenomenological relationships based on experimental observations by Li et al. (2020) that explain the early fatigue life of cross-ply carbon fiber-reinforced polymers, new opportunities exist. More details on damage mechanics behind these findings are incorporated in section 2.1. Most importantly, it is observed that delamination in stage I is responsible for a greater stiffness degradation than matrix cracks. This directly introduces multicausality in stiffness degradation, which should be accounted for in the machine learning model. Additionally, it is important to be aware of the size of the case study dataset available. This dataset, which will be introduced in chapter 3 consists of seven specimens. In general, it is also desirable to limit the required size of a dataset to a minimum due to the considerable time and cost associated to testing campaigns. This makes model-based approaches, which require less data, a feasible option.

Therefore, the prognostics elaborated upon in this section focus on model-based approaches. The principle of non-linear least squares (NLS) in view of fitting a phenomenological model to observed data is discussed in subsection 2.3.1. As stated in the research objective, the machine learning model shall be able to offer real-time adaptivity of the model parameters based on information from SHM measurements. Therefore, the principles and theory behind PF are treated in subsection 2.3.2. Along with this, special attention is paid to introducing, propagating and monitoring uncertainties where required to improve validity of the model. For this purpose, uncertainties inherent to prognostics of composites are summarized in subsection 2.3.3.

2.3.1 Non-Linear Least Squares

NLS is a degradation model in which model parameters relate non-linearly to the predicted property. In NLS, parameter fitting is a deterministic optimization process, resulting in a single set of parameters with the lowest weighted sum of squared errors as given by Equation 2.1. In this equation, y_k represents the k'th measurement point, and z_k the k'th simulation output of n_y measurement points. Each of those has a weight w_k (Kim et al., 2016).

$$SSE_W = \sum_{k=1}^{n_y} \frac{(y_k - z_k)^2}{w_k^2} \tag{2.1}$$

To minimize SSE_W, several methods can be used. These all start from an initial value as a function argument and calculate the next 'more optimal' value using an optimization algorithm. Once an optimum is reached, the algorithm stops and the last used arguments are the NLS fit. However, one should note that very often an algorithm stops at only a local minimum as many functions are not globally concave. While methods like simulated annealing exist to prevent this, they are still computationally expensive and hard to implement (Kuan, 2004). Therefore, this is out of the scope of this thesis, and a suitable local optimization shall be used for the specific application. For unconstrained search, Levenberg-Marquardt is a well known and studied method with reliable results. The Levenberg-Marquardt is a hybrid method that updates variables adaptively. This means that for small values of a damping parameter, Gauss-Newton updating is used, while for larger values of the same damping parameter, gradient descent is used. Once the solution improves, Levenberg-Marquardt approaches a Gauss-Newton method, which makes the solution accelerate to a local minimum (Gavin, 2019).

Despite the dependency of NLS on training data and the lack of uncertainty propagation, it is investigated how the result is when embedded in a PF algorithm. This means that a damage (evolution) model could be fit using NLS, and that a feasible range of model parameters can be updated using PF. Therefore, the PF algorithm is elaborated upon below and opportunities of the NLS model embedded in the PF are explored in the remainder of this report.

2.3.2 Particle Filtering

In order to give the NLS model the ability to adapt, it can be used within a Bayesian model. A Bayesian model makes use of the principle of Bayesian inference. An example of such technique is Markov chain Monte Carlo (MCMC) sampling. In this method, initial samples are generated from a proposal distribution. Each of the particles is then propagated to a posterior distribution as visualized in Figure 2.6. However, in this case, online prediction is not possible as particles are not updated throughout the degradation process. Therefore, several papers suggest to use MCMC sequentially as a state-space model. This is often referred to as sequential Monte Carlo (SMC), or PF (Kim et al., 2016; Hu et al., 2019; Andrieu et al., 2010). The big advantage of using the PF is that the state-space model can be non-linear and non-Gaussian, while keeping computational cost limited according to Chiachío et al. (2015a).

A PF is a method for prognostics in which the probability density function (pdf) of parameters is represented by samples/particles. At each time step, three adjustments are performed on

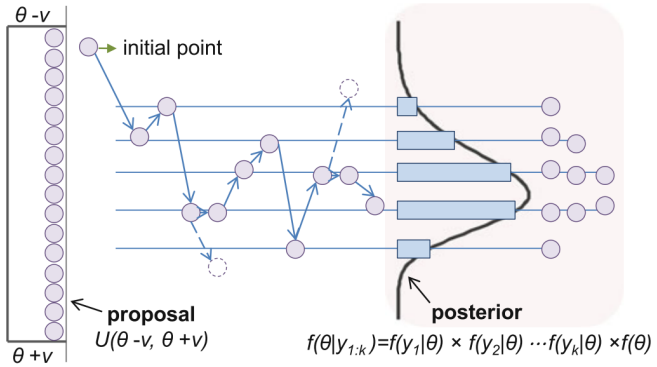

Figure 2.6: Visualization of Markov chain Monte Carlo process (Kim et al., 2016).

the posterior set of particles of the previous time step. First, a prior distribution at time step t_n is predicted through state transition of the damage properties of the posterior distribution at time step t_{n-1}. After this, the weights of each particle are updated by judging how close the prior degradation property at step t_n is to the measurement (likelihood) at step t_n. Finally, depending on the PF architecture, resampling can be performed to normalize the weights and obtain a posterior distribution at time step t_n. All of these steps are illustrated in Figure 2.7 (Kim et al., 2016).

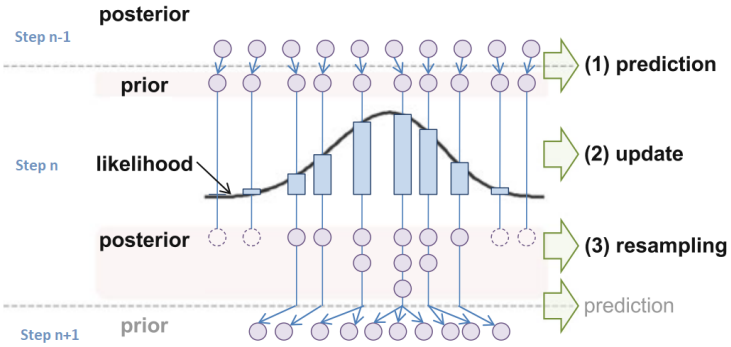

Figure 2.7: Visualization of particle filtering process (Kim et al., 2016).

Particle Filtering Algorithms

In case resampling is used, the PF approach is often called systematic importance resampling (SIR), while PF without resampling is referred to as systematic importance sampling (SIS). The major reason that SIR is often preferred over SIS is because after some time only a few samples would dominate the estimate as only those have a significant weight compared to the others. This problem of SIS is called weight degeneracy. While SIR (with resampling every time step) mitigates the weight degeneracy problem, it introduces sample impoverishment. Sample impoverishment indicates the issue that samples with high weights are likely to be drawn multiple times during resampling, and that samples with small weights are not likely to be drawn at all. This means that the diversity of samples decreases and collapses eventually to

a single sample or a set of unique samples. Therefore, a regularization is used, the regularized PF, that only resamples whenever the effective sample size falls below a pre-defined threshold (Orhan, 2012).

Particle Filtering Resampling Techniques

Different resampling techniques exist, of which multinomial resampling, systematic resampling and residual resampling are the most common. The first uses resampling with replacement, which selects particles in the posterior distribution based on a multinomial distribution for parameters in the vector containing the corresponding probability of success in the weight vector. This process is presented visually in Figure 2.8, where the length of the rectangles represents the weight of a particle represented by letters. N iterations are performed, for which each particle with a higher weight has a higher probability to be picked. This means N random variables are required for each pick, resulting in low computational efficiency of this method. On the other hand, in systematic resampling, N_s ordered variates are uniformly distributed. In each sub-interval, the same position is picked randomly from each of the boundaries. Therefore, in systematic resampling, only a single random variable is required, adding computational efficiency compared to multinomial resampling (Li et al., 2015; Candy, 2016).

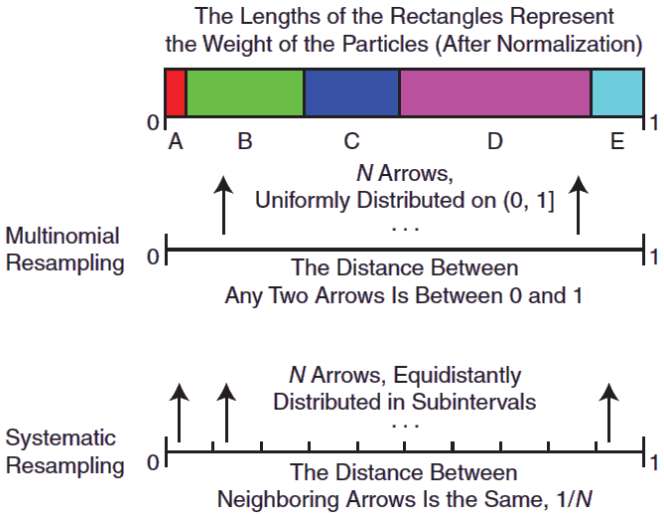

Figure 2.8: Visualization of multinomial and systematic resampling process (Li et al., 2015).

Finally, residual resampling is an alternative for standard resampling methods. In this approach, each particle with a weight larger than the integer value $\frac{1}{N_s}$ is replicated. All residuals with the remainder of the weights are subjected to a resampling approach, being multinomial resampling for traditional residual resampling. However, if a constant sample size is preferred, residual resampling proves not suitable according to Li et al. (2013). This is the case as branch kill procedures, required to provide sufficient computational efficiency, cannot be used without a decrease in sample size. As it is preferred in this thesis to keep the sample size constant, systematic resampling can be considered the most suitable strategy.

2.3.3 Uncertainty in Remaining Useful Life Prognostics

While making RUL prognosis of continuous fiber-reinforced composites, uncertainties are present. The subjective uncertainty of the RUL prognostics arises due to variability across different specimens as well as specimen-specific variability. It is therefore important to represent, quantify, propagate and manage uncertainties adequately. However, before this is possible, the challenging step of identifying inherent uncertainties must be taken. Sankararaman and Goebel (2013) identify the following types of uncertainty:

- **Present uncertainty:** This involves uncertainty on the condition of the continuous fiber-reinforced composite at the time step at which the RUL is estimated. Specifically applied to PF, as considered in this thesis, this is directly related to state uncertainty at time step n. Reducing the present uncertainty is therefore possible by using more accurate sensors and improving filtering approaches. While it is impossible to get rid of this type of uncertainty, it is important to be quantified and visualized using prediction intervals (Kim et al., 2016).
- **Future uncertainty:** This type of uncertainty is inherent to prognostics, for which the future conditions are unknown at time step n. Therefore, this is dependent on future loading conditions, environmental conditions, operating conditions etc. Throughout this thesis, the focus is on constant amplitude loading. Additionally, future states are predicted using a prediction model, which directly introduces the third type of uncertainty discussed below.
- **Modeling uncertainty:** Future states are predicted using an underlying, in this case model-based, state transition model. However, as a perfect damage model does not exist for composites, the predicted states will differ from the actual states. More specifically, modeling uncertainties are introduced by uncertain model parameters, noise etc. It is therefore important to add a random walk to the PF algorithm to allow model parameters to remain dynamic throughout the lifetime (Chiachío et al., 2015a).
- **Prediction method uncertainty:** Even in case that a perfect model would be available and that future/present states can be predicted perfectly, uncertainty remains in the inability to quantify all sources of uncertainty. This is referred to as the prediction method uncertainty, which can be taken along in the PF prediction step for each damage state.

Apart from the aforementioned uncertainties, Eleftheroglou (2020) rightly identifies a fifth source: the **Past uncertainty**. This type of uncertainty is associated to the intrinsic scatter, elaborated upon in subsection 2.1.1. This type of uncertainty mostly depends on the quality of the material used, and on the manufacturing process.

Given the aforementioned sources of uncertainty, it is essential to interpret them appropriately. Apart from the uncertainties above, Talreja (2003) and Eleftheroglou (2020) describe composite damage evolution as a stochastic process. In order to represent, quantify, propagate and

manage the uncertainties adequately, it is irrelevant to provide deterministic solutions to RUP and RUL predictions. This means that it is more appropriate to use a subjective, Bayesian approach to obtain a pdf of the RUP and RUL prediction. PF belongs to Bayesian approaches in which the concept of likelihood and sampling is used as approximations to reduce the complexity (Sankararaman, 2012). In the PF algorithm itself, no assumptions are made with regards to the shape of the pdf of RUP and RUL predictions. This is favorable according to Sankararaman and Goebel (2013). Only for the purpose of visualizing the results, a mean and standard deviation will be used to represent the particle population (as a normal distribution) as elaborated upon in chapter 4. However, a true distribution of the particle population can still be represented with histograms. Finally, it is important to note that the selection of PF is favorable as this algorithm is not limited to a Gaussian distribution of parameters and because it is able to deal with non-linear prediction models. This makes the PF algorithm very flexible in terms of model type and noise distribution (Srini, 2019).

Chapter 3

Case study Tests and Data

This chapter introduces the case study dataset used to construct the NLS-PF machine learning model. This dataset was constructed by Li et al. (2020), a colleague from the Pythia team at Delft University of Technology. The most important characteristics are elaborated upon in this chapter including the specimens and test set-up section 3.1, loading conditions (section 3.2), DIC measurements (section 3.3) and the definition of stage I to stage II transition (section 3.4).

3.1 Specimens and Test Set-up

The specimens utilized for these tests were created with UD prepreg. The Hexply® F6376C-HTS(12 K)- 5-35%, with mechanical properties as shown in Table 3.1, has high stiffness carbon fibers (Tenax®-E-HTS45) combined with a tough epoxy (Hexply® 6376). The nominal thickness of a UD ply is 0.125 mm and the fiber volume of the prepreg is 58%.

Table 3.1: Mechanical Properties of Hexply® F6376C-HTS(12K)-5-35% (Kupski et al., 2019)

Longitudinal tensile strength	X_{T}	$2,274$MPa
Longitudinal compressive strength	X_{C}	$1,849$MPa
Transverse tensile strength	Y_{T}	102MPa
Transverse compressive strength	Y_{C}	255MPa
Longitudinal tensile modulus	$E_{11\mathrm{T}}$	$142,000$MPa
Transverse tensile modulus	$E_{22\mathrm{T}} = E_{33\mathrm{T}}$	$9,100$MPa
In-plane shear modulus	$G_{12} = G_{13}$	$5,200$MPa
Transverse shear modulus	$G_{23} = E_{33\mathrm{T}} / (2(1+\nu_{23}))$	$3,500$MPa
In-plane shear strength	$S_{12} = S_{13}$	63MPa
Transverse shear strength	S_{23}	35MPa
In-plane Poisson ratio	$\nu_{12} = \nu_{13}$	0.27
Transverse Poisson ratio	ν_{23}	0.30

The UD prepreg has been used to construct laminates with dimensions 300 mm x 300 mm and with stacking sequence $[0_2/90_4]_s$. The specimens were cured in the autoclave and cut to

dimensions 250 mm x 25 mm using a water-cooled diamond saw. In order to ensure sufficient clamping in the test set-up, paper grips were glued with cyanoacrylate glue on both ends with a length of 50 mm. A schematic representation of a single specimen with relevant dimensions is displayed in Figure 3.1.

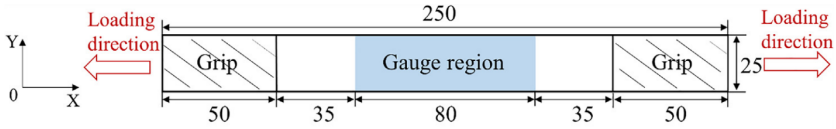

Figure 3.1: Schematic representation of case study specimen dimensions and loading direction (Li et al., 2020).

Seven specimens with the aforementioned specifications were tested in the laboratory of the Aerospace Engineering faculty at Delft University of Technology. Tests were conducted at room temperature using a 60 kN hydraulic fatigue machine. An overview of the test set-up is provided in Figure 3.2. One 9 megapixel camera was added on either side facing the specimen edge to collect information on transverse cracks. Additionally, two 5 megapixel cameras were mounted next to each other facing the specimen for DIC. All cameras were focused on the gauge region indicated in Figure 3.1. This is the area of interest with a length of 80 mm.

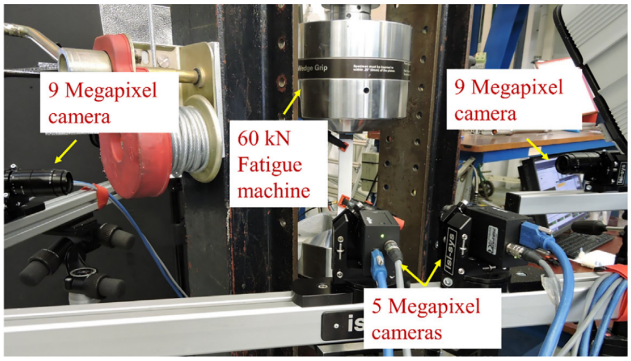

Figure 3.2: Overview of the case study test set-up for early fatigue life testing (Li et al., 2020).

3.2 Loading Conditions

During the experiments, seven symmetric cross-ply specimens were subjected to tension-tension fatigue loading with a stress ratio of 0.1 and a frequency of 5 Hz. The maximum stress level was set to 70% of the ultimate tensile strength (UTS), which corresponds to 507 MPa obtained from static tensile tests for the given prepreg, stacking sequence and geometry. In order to obtain camera recordings, loading and unloading ramps are applied every 500 cycles with a rate of 19 kN/s. The testing scheme is summarized in Figure 3.3. The DIC measurements and data are elaborated upon in section 3.3. Tests were stopped at 10^5 cycles, well beyond reaching stage I to stage II transition.

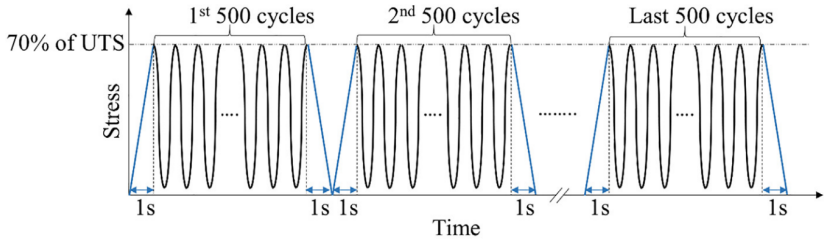

Figure 3.3: Testing scheme of case study specimens with loading-unloading every 500 cycles (Li et al., 2020).

3.3 Digital Image Correlation Measurements

During the experiments of the seven specimens, DIC information was captured using 4 cameras as touched upon before and shown in Figure 3.2. During each loading and unloading ramp, the cameras capture images simultaneously every 50 ms. The two 5 megapixel cameras mounted in front of the specimen measure the in-plane strain using DIC. For that purpose, the cameras are focused on the 80 mm length gauge region indicated in Figure 3.1 on which a speckle pattern was applied with dot size 0.18 mm. The other two 9 megapixel cameras face the edge of the specimen on either side and are also focused on the gauge region. At these positions, they are capable to monitor the damage on both edges that were painted white to guarantee contrast between regions with and without cracks.

In subsection 3.3.1, 3.3.2 and 3.3.3, it is explained which and how data was captured for the crack density, delamination ratio and stiffness respectively. Special attention is paid to the method of data extraction as will be required in chapter 4 to define the suitability of measurements in the online algorithm, and if included to quantify the measurement uncertainty.

3.3.1 Transverse Crack Density

Li et al. (2020) developed a MATLAB analysis tool to count the number of transverse cracks in the 90° plies using the cameras focused at both edges of the gauge region. In order to quantify the transverse crack density ρ, the average of the amount of transverse cracks on both edges was divided by the gauge length. The case study data for the transverse matrix crack evolution is provided in Figure 3.4. Based on the observed data of the seven specimens, a delay in matrix crack density evolution was noticed for a group of specimens. The terminology and specimen names in this thesis are kept identical to the original research. Group 1 is therefore the group of four specimens without a delay in crack density evolution, while group 2 is the group of three specimens showing delay.

3.3.2 Delamination Ratio

Li et al. (2020) managed to construct a model to obtain the delamination ratio. This model uses the observation that the in-situ Poisson ratio ν of the outer ply (which can be obtained through DIC measurements) shows a linear relationship with the normalized area of transverse

strain concentration. However, the latter, which is measured indirectly via the Poisson ratio ν, did not completely represent early delamination propagation close to the edges. For that purpose, the inter-laminar crack ratio I_r was introduced, which is the mean of max($L_{r,1}$, $L_{r,2}$) and max($L_{l,1}$,$L_{l,1}$) divided by the gauge length. The parameters $L_{r,1}$ and $L_{r,2}$ are the total length of inter-laminar cracks on the interface on the right-hand side of the specimen. The same principle holds on the left-hand side for $L_{l,1}$ and $L_{l,2}$. Therefore, these four could be collected using the two cameras facing both specimen edges. In order to combine the in-situ Poisson ratio ν and the inter-laminar crack ratio I_r measurements, it is established that $d_r = \nu \cdot I_r$. Doing so, measurements for the delamination ratio are provided in Figure 3.5.

While the measurements of the delamination ratio provide useful information on phenomenological relations for delamination damage progression, these will not be used in the PF algorithm to update model parameters of the testing specimen in real-time. This is because the in-situ measured Poisson ratio ν alone does not provide sufficient information to obtain the delamination ratio, making it difficult measure the actual delamination ratio in-situ. However, in the offline pre-training step of the PF, the measurements can be used to establish relations for damage evolution. More information on the use of delamination data is provided in chapter 4.

3.3.3 Stiffness

A dynamic axial stiffness measurement was collected every 500 cycles during hysteresis loops at the loading ramps. This was done by combining the axial stress σ_{xx} and the average axial strain $\bar{\epsilon}_{xx}$ obtained through VIC-3D DIC software and the cameras facing the specimen 0° ply. The axial stiffness E_{initial} and stiffness E_n are stiffnesses measured by the loading ramp at time step 0 and n respectively. Dividing E_n by E_{initial} yields the normalized longitudinal stiffness $\frac{E_N}{E_0}$ as provided in the dataset (Figure 3.6).

Additionally, Li et al. (2020) managed to decouple the stiffness degradation in stage I into transverse crack induced stiffness degradation and delamination induced stiffness degradation. These two are provided in the dataset as D_{tc} (as a function of crack density ρ in Figure 3.7) and D_{del} (as a function of delamination ratio d_r in Figure 3.8) respectively. It should be noted that D gives stiffness degradation in stage I, thus $D_{tc} + D_{del} = 1$ at stage transition. This in turn means that D is related to E_n as shown in Equation 3.1. Here, E_I is the dynamic stiffness at the end of stage I. Both D_{tc} and D_{del} are not used in-situ, which means they are not included in the PF algorithm for updating. However, in the pre-training step of the PF, the measurements can be used to map the crack density and delamination ratio to the normalized stiffness $\frac{E_n}{E_0}$.

$$D = \frac{(E_{\text{initial}} - E_N)}{(E_{\text{initial}} - E_I)} \tag{3.1}$$

3.4 Stage Transition Definition

For later use in the PF algorithm, it is important to define a failure criterion. While the stage I to stage II transition is not the same as macroscopic failure, it will be treated as the end-of-early-fatigue-life (EOEFL) condition to determine the RUL in this case study. The transition was defined during the testing campaign as less than 0.001 decrease in normalized stiffness $\frac{E_N}{E_0}$ over 2500 cycles. The same definition will be used in the PF method in chapter 4.

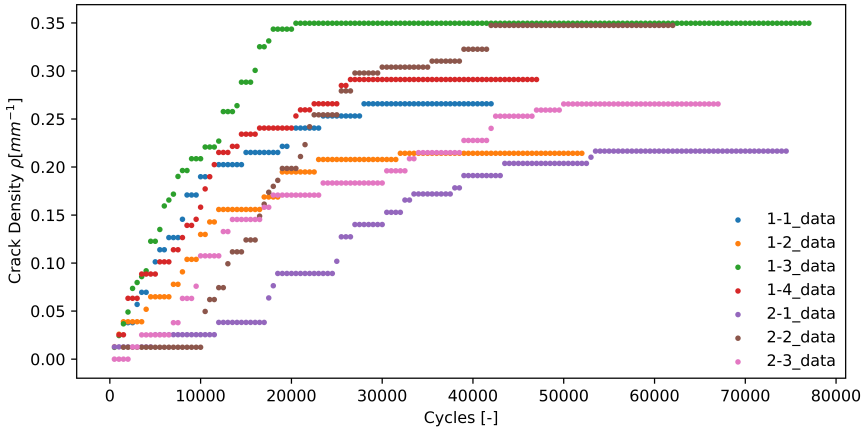

Figure 3.4: Case study data for transverse matrix crack density evolution in early fatigue life.

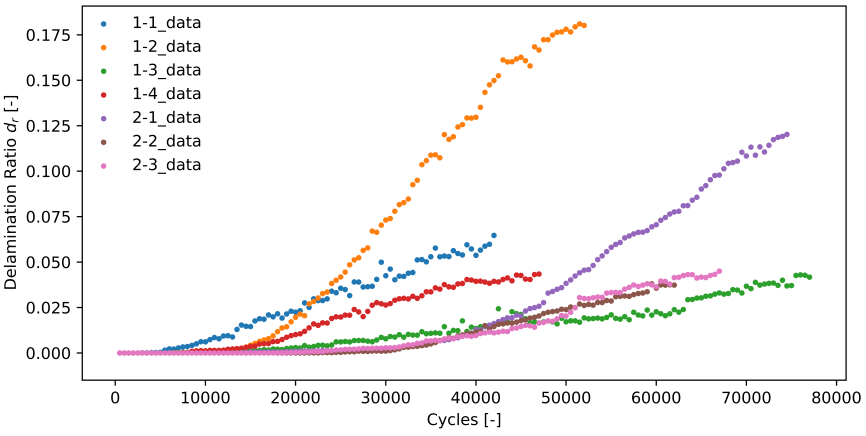

Figure 3.5: Case study data for delamination ratio evolution in early fatigue life.

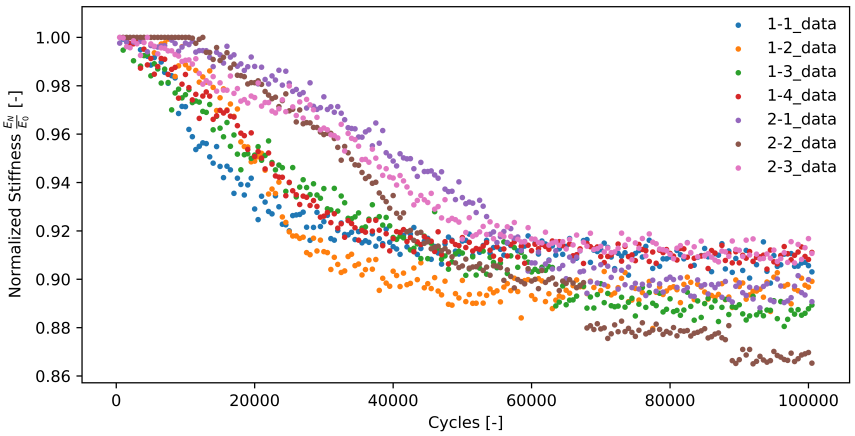

Figure 3.6: Case study data for normalized dynamic stiffness evolution in early fatigue life.

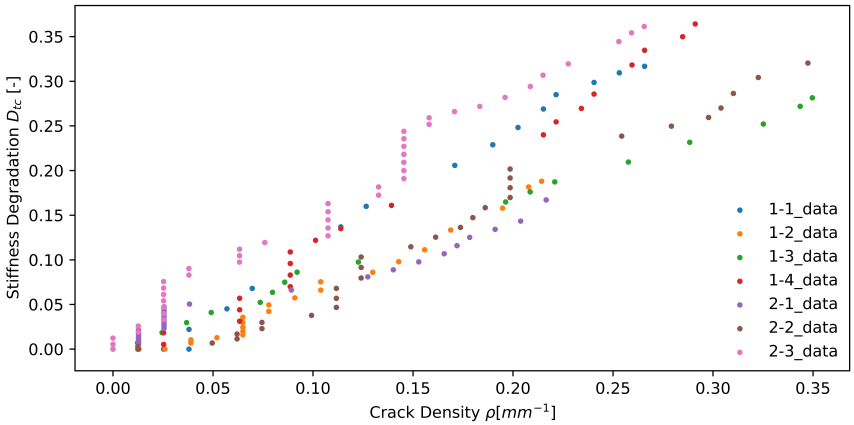

Figure 3.7: Case study data for transverse matrix crack induced stiffness degradation as a function of the transverse matrix crack density.

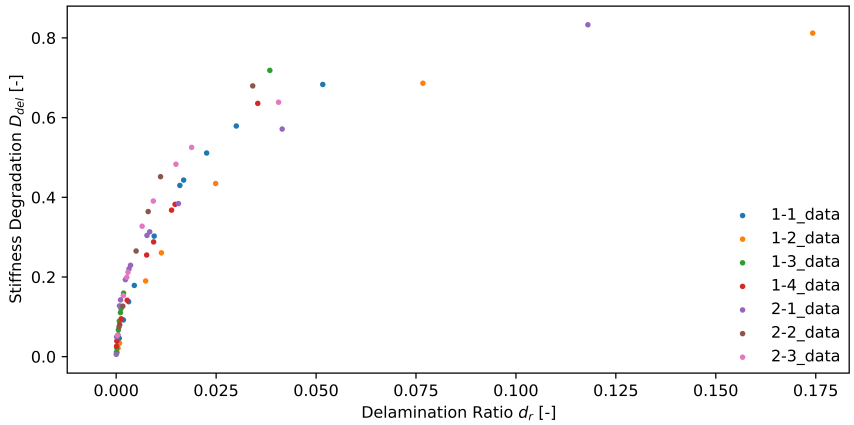

Figure 3.8: Case study data for delamination induced stiffness degradation as a function of the delamination ratio.

Chapter 4

Case Study Methodology

This chapter establishes the methodology used to construct the model-based machine learning model for this research on case study data. Throughout this chapter, the flowchart shown in Figure 4.1 serves as a guideline through all steps required to successfully implement the model. The case study is based on the data in chapter 3. In section 4.1, the phenomenological relations are established based on the case study data. These will serve as input to the pre-training process (section 4.2), in which the pdf of the model parameters is estimated based on training specimens. The pdf for each of the model parameters is subsequently used in the initialization step (section 4.3). After this, the online process is started. The filtering step (section 4.4) is built-up of four components: prediction of damage evolution (when combined referred to as state transition), updating particle weights based on incoming online measurements, resampling when required, and adding a random walk on the model parameters. Before moving to the failure criterion, the particles and weights of the current filtering step are used (only at time steps for which a measurement was available) to perform prognostics. As a result of the prognostics (section 4.5), the RUP for future states and the RUL to EOEFL are stored. Finally, section 4.6 focuses on the performance evaluation of the RUL prognostics to EOEFL.

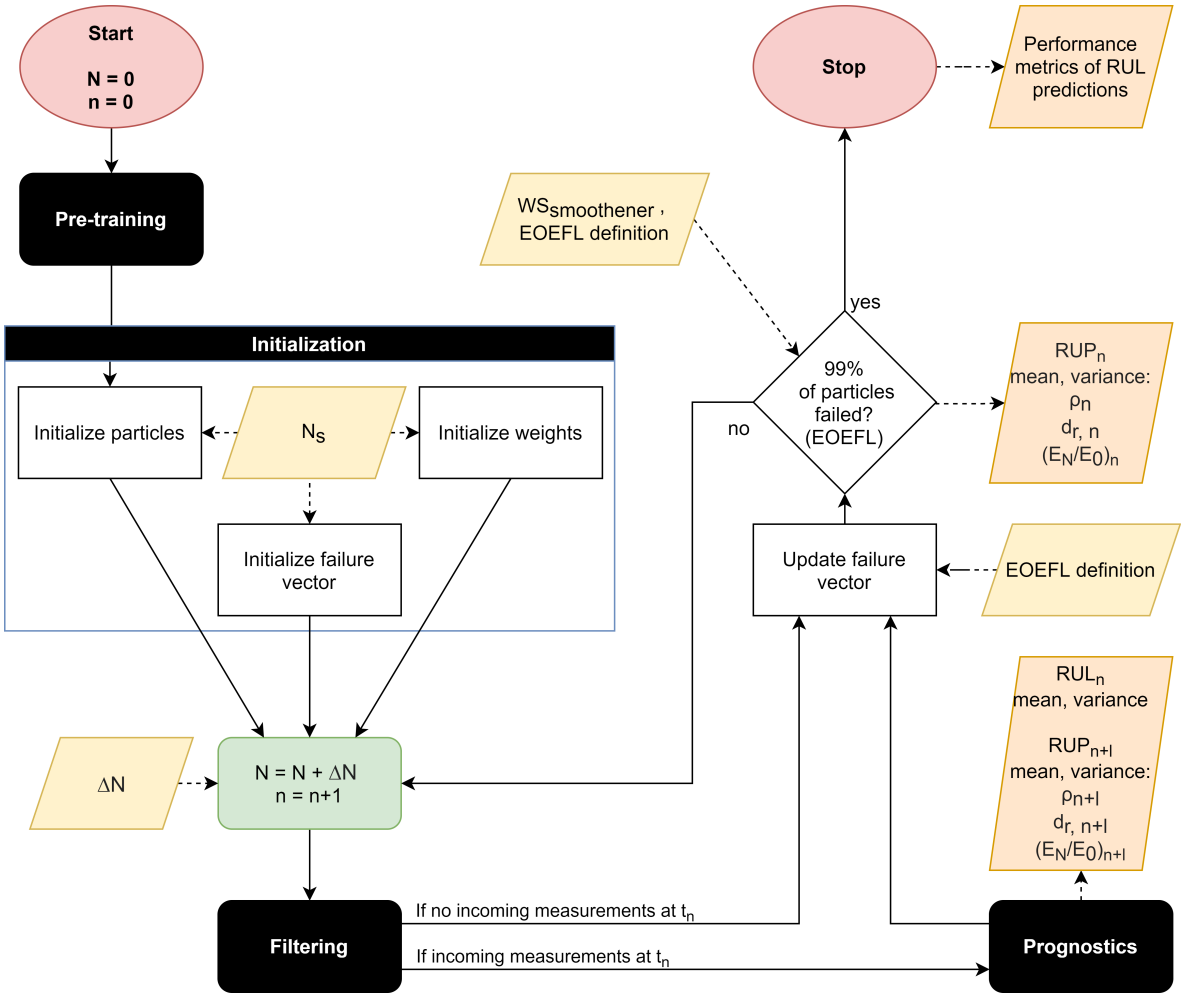

Figure 4.1: Flowchart of the entire algorithm with inputs (yellow), outputs (orange) and other sub-algorithms (black).

4.1 Phenomenological Models and Parameters

As previously mentioned, the first step is to construct phenomenological relations based on the observations as elaborated upon in chapter 3. Using the data provided, five phenomenological models are constructed in subsection 4.1.1 to 4.1.5. In this section, only the functions are given, more details on NLS fitting and the filtering of model parameters are given in section 4.2 and section 4.4 respectively. The first describes the evolution of transverse matrix crack density given a time step ΔN. Similarly, a second model describes the delamination ratio evolution given a time step ΔN. Finally, separate models for stiffness degradation induced by matrix cracks and delamination ratio are constructed. When combined, the normalized stiffness is obtained as a function of the induced stiffness degradation components. The phenomenological models each have their corresponding model parameters that will be either static or adaptive in the PF algorithm.

4.1.1 Crack Density vs. Cycles

Looking at the case study data (Figure 3.4), an exponential behavior in crack density with respect to cycles is observed. In order to perform NLS fitting in section 4.2, a pre-defined phenomenological relation is required. For this purpose, Equation 4.1 is a suitable function based on the observed trend. In this equation, the parameters a, b and c are model parameters that will be adaptive in the PF model parameter vector. A condition is present on the parameter c to ensure the crack density ρ cannot be negative. Additionally, $v_{\rho,total}$ accounts for uncertainties in the prediction method. It is assumed that $v_{\rho,total}$ is normally distributed as $\mathcal{N}(0, \sigma_{v,\rho,total})$.

$$\rho(N) = \begin{cases} 0 & \text{for } N \leq c \\ a \cdot [1 - exp\,(b \cdot (N - c))] + v_{\rho,total} & \text{for } N > c \end{cases} \tag{4.1}$$

As a PF requires an evolution model to perform state transition, an evolution model is established in Equation 4.2. The evolution model is obtained by differentiation of Equation 4.1 with respect to the cycles N. In order to ensure evolution of crack density over ΔN cycles, the right-hand side of the equation is multiplied by ΔN. It is observable that after differentiation, the same model parameters a, b and c remain.

$$\Delta\rho(N, \Delta N) = \begin{cases} 0 & \text{for } N \leq c \\ [-a \cdot b \cdot exp\,(b \cdot (N - c)) \cdot \Delta N] + v_\rho & \text{for } N > c \end{cases} \tag{4.2}$$

It should be noted that the normally distributed error in Equation 4.1 changes when differentiating. Therefore, the standard deviation after differentiation is transformed to obtain $\sigma_{v,\rho}$ using Equation 4.3. This equation uses the assumption that the uncertainties are independent random variables (Taylor and Thompson, 1998). This means the prediction method error term of the evolution function becomes v_ρ with normal distribution $\mathcal{N}(0, \sigma_{v,\rho})$. However, as no exact value is known for the prediction method uncertainty, the standard deviation $\sigma_{v,\rho}$ is adaptive in the model parameter vector of the PF.

$$\sigma_{v,\rho} = \frac{\sqrt{2} \cdot \sigma_{v,\rho,total}}{\Delta N} \tag{4.3}$$

4.1.2 Delamination Ratio vs. Cycles

A similar methodology as for the crack density vs. cycles is followed to obtain the phenomenological relation between delamination ratio and cycles based on the case study data (Figure 3.5). For this purpose, Equation 4.4 is a suitable function showing logistic characteristics. It is observed from the case study data that a maximum growth in delamination ratio is present at the time of crack saturation, after which the rate of delamination decreases again. In this phenomenological relation, the parameters d, e, f and g exist. Additionally, $v_{d_r,total}$ accounts for uncertainties in the prediction method. It is assumed that $v_{d_r,total}$ is normally distributed around zero as $\mathcal{N}(0, \sigma_{v,d_r,total})$.

$$d_r(N) = \left[\frac{d}{1 + exp\left(-e \cdot (N - f)\right)} + g\right] + v_{d_r,total} \tag{4.4}$$

In order to account for the multicausality of stiffness degradation, a second evolution model is established Equation 4.5, now for the delamination ratio. This evolution model is obtained by differentiation of Equation 4.4 with respect to the cycles N. To ensure evolution of delamination over ΔN cycles, the right-hand side of the equation is multiplied by ΔN. It is observable that after differentiation, only the model parameters d, e and f remain and will be included in the adaptive model parameter vector of the PF algorithm.

$$\Delta d_r(N, \Delta N) = \left[\frac{d \cdot e \cdot exp\left(-e \cdot (N - f)\right)}{\left[1 + exp\left(-e \cdot (N - f)\right)\right]^2} \cdot \Delta N\right] + v_{d_r} \tag{4.5}$$

Equivalent to the methodology for the crack density, the normally distributed error in Equation 4.4 changes when differentiating. Therefore, the standard deviation after differentiation is transformed to obtain σ_{v,d_r} using Equation 4.6. Doing so, the prediction method error term of the evolution function becomes v_{d_r} having a zero-mean normal distribution $\mathcal{N}(0, \sigma_{v,d_r})$. However, as again no exact value is known for the prediction method uncertainty, the standard deviation σ_{v,d_r} is adaptive in the model parameter vector of the PF.

$$\sigma_{v,d_r} = \frac{\sqrt{2} \cdot \sigma_{v,d_r,total}}{\Delta N} \tag{4.6}$$

4.1.3 Crack Induced Stiffness Degradation vs. Crack Density

As discussed in the case study data in chapter 3, the stiffness degradation was decoupled into crack induced stiffness degradation and delamination induced stiffness degradation. While these measurements are not used in-situ, they allow to map the effect of transverse cracks on the stiffness degradation in stage I. The data in Figure 3.7 shows a linear behavior between crack density ρ and crack induced stiffness degradation D_{tc}. Therefore, h and i are introduced as model parameters in Equation 4.7. The condition on -i/h is present to prevent crack induced stiffness degradation to be smaller than 0. Additionally, the prediction method uncertainty is added by assuming 0-mean normally distributed noise $\mathcal{N}(0, \sigma_{v,D_{tc}})$.

$$D_{tc}(\rho) = \begin{cases} 0 & \text{for } \rho \leq -i/h \\ [h \cdot \rho + i] + v_{D_{tc}} & \text{for } \rho > -i/h \end{cases} \tag{4.7}$$

As differences in behavior per specimen are less expressive, the h and i parameters can be generalized for all specimens. Therefore, the parameters h, i and $v_{D_{tc}}$ are static in the PF algorithm, and thus the same for all particles. How the fitting parameters are determined, is elaborated upon in more detail in section 4.2.

4.1.4 Delamination Induced Stiffness Degradation vs. Delamination Ratio

Apart from the crack induced stiffness degradation, delamination induced stiffness degradation is required to describe total stiffness degradation. For this purpose, the phenomenological fitting function is defined in Equation 4.8. A Linear relation is observed in Figure 3.8 between the crack density ρ and the crack induced stiffness degradation D_{tc}. Therefore, j and k are introduced as model parameters. To this prediction model, a prediction method uncertainty is added by assuming 0-mean normally distributed noise $\mathcal{N}(0, \sigma_{v,D_{del}})$.

$$D_{del}(d_r) = j\left[exp\left(k \cdot d_r\right) - 1\right] + v_{D_{del}} \tag{4.8}$$

Due to the lack of data for some specimens for higher delamination ratios, it is decided to generalize the model parameters j and k for all specimens. This means that j, k and $v_{D_{del}}$ are static in the PF algorithm, and thus the same for all particles. How the fitting parameters are determined, is elaborated upon in more detail in section 4.2.

4.1.5 Normalized Stiffness vs. Cycles

As mentioned in section 3.4, the stage I to stage II transition, of EOEFL of a specimen is reached when the stiffness degrades less than 0.001 over 2500 cycles. Therefore, as now only the induced stiffness degradation terms D_{tc} and D_{del} are described by phenomenological relations, an additional relation is required to obtain the normalized stiffness $\frac{E_N}{E_0}$. This relation is derived from Equation 3.1. However, in an online process, the stiffness at the end of stage I E_I is still unknown and a fixed EOEFL condition on the stiffness property is not desirable due to the large variation between specimens (ranges between 0.89 and 0.92 for the specimens in the case study). Therefore, an additional adaptive model parameter m is added in the PF which is equivalent to $\frac{E_I}{E_{\text{initial}}}$. Using this property, and given that $D = D_{tc} + D_{del}$, Equation 4.9 is obtained.

$$\frac{E_N}{E_0}(D_{tc}, D_{del}) = (m-1) \cdot (D_{tc} + D_{del}) + 1 \tag{4.9}$$

4.1.6 Overview of Damage Properties and Model Parameters

In the previous subsections, multiple phenomenological relations are defined. In order to summarize the damage properties contained as variables in the relations, Table 4.1 is presented. $\Delta\rho$ and Δd_r have ΔN as independent variable, and thus predict damage evolution between states. D_{tc} and D_{del} are only used as relations to obtain $\frac{E_N}{E_0}$, as it is required for the EOEFL condition. For later reference in section 4.4, it is summarized from chapter 3 that only ρ and $\frac{E_N}{E_0}$ can be measured in-situ with reasonable accuracy and are thus only suitable for updating

in the PF algorithm. However, the phenomenological relations in this section are pre-trained (section 4.2) with in-situ and ex-situ measurements.

Table 4.1: Overview of PF Damage Properties

		Growth Function		In-Situ Measurement	
Damage Property	Independent Variables	yes	no	yes	no
ρ	N, ΔN	x		x	
d_r	N, ΔN	x			x
D_{tc}	ρ		x		x
D_{del}	d_r		x		x
$\frac{E_N}{E_0}$	D_{tc}, D_{del}		x	x	

The model parameters describing the phenomenological relations between damage properties are summarized in Table 4.2. More information on pre-training of the model parameters using NLS is given in section 4.2. For future purposes, it is important to note the difference between static parameters in the PF and adaptive parameters. Where static parameters will be initialized to the same value for all particles and cannot change throughout the process, adaptive parameters are initialized to a range of values in section 4.3 and can change in the PF algorithm filtering step (section 4.4). The latter is desirable for relations that involve large variability per specimen such as $\Delta\rho(N, \Delta N)$, $\Delta d_r(N, \Delta N)$ and $\frac{E_N}{E_0}(D_{tc}, D_{del})$.

Table 4.2: Overview of PF Model Parameters

	Usage in PF		Phenomenological Relation	
Model Parameter	Static	Adaptive	Dependent Variable	Independent Variables
a		x	ρ	N, ΔN
b		x	ρ	N, ΔN
c		x	ρ	N, ΔN
d		x	d_r	N, ΔN
e		x	d_r	N, ΔN
f		x	d_r	N, ΔN
h	x		D_{tc}	ρ
i	x		D_{tc}	ρ
j	x		D_{del}	d_r
k	x		D_{del}	d_r
m		x	$\frac{E_N}{E_0}$	D_{tc}, D_{del}
$\sigma_{v,\rho}$		x	ρ	N, ΔN
σ_{v,d_r}		x	d_r	N, ΔN
$\sigma_{v,D_{tc}}$	x		D_{tc}	ρ
$\sigma_{v,D_{del}}$	x		D_{del}	d_r

4.2 Pre-Training

In this section, the first black block in the flowchart (Figure 4.1), being pre-training, is focused on. A more detailed separate flowchart of the pre-training step is shown in Figure 4.2. The outputs of the pre-training process are required in the initialization process (section 4.3) of the particles.

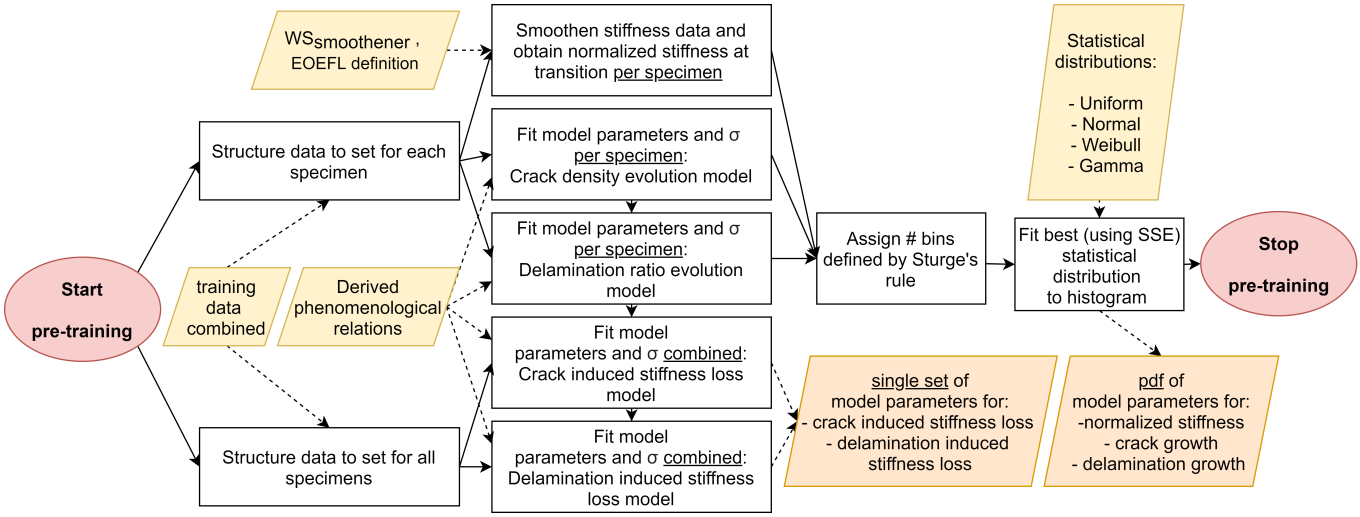

Figure 4.2: Flowchart of the pre-training algorithm with inputs (yellow) and outputs (orange).

4.2.1 Train-Test Split

Before starting the pre-training process, train-test split is performed to eliminate bias. This means that pre-training is done on the six training specimens. The seventh specimen, the test specimen, is only used in the online process. Additionally, the training data are split into two sets for pre-training purposes. One set contains the training data combined for all specimens for crack induced stiffness loss D_{tc} as a function of the crack density ρ, and for delamination induced stiffness loss D_{del} as a function of the delamination ratio d_r (static model parameters). The second set contains training data split per specimen for crack density ρ, delamination ratio d_r and normalized stiffness $\frac{E_N}{E_0}$ as a function of cycles (adaptive model parameters).

4.2.2 Fitting of Model Parameters

Using the splits in the training data, model parameters for the phenomenological relations presented in section 4.1 can be obtained. This is done by fitting each function to the data using the NLS method curve_fit in SciPy (SciPy). As minimization algorithm, Levenberg-Marquardt is used. This is proven to be a reliable method for an unconstrained search as discussed in subsection 2.3.1 (Gavin, 2019). The main difference between the determination of static and adaptive model parameters is explained below.

Static Model Parameters

As mentioned before, static model parameters in the PF algorithm will be the same value for all particles. Therefore, the first set of training data (combined for all specimens) is used to fit the phenomenological relations of $D_{tc}(\rho)$ (Equation 4.7) and $D_{del}(d_r)$ (Equation 4.8). Once the best set of model parameters h, i, j and k is obtained using NLS fitting, the standard deviations of the prediction method uncertainty $\sigma_{v,D_{tc}}$ and $\sigma_{v,D_{del}}$ shall be estimated. As touched upon in section 4.1, the error term in both is assumed to follow a 0-mean normal distribution.

To obtain the error at each measurement point, the dependent variable estimated using the fit is subtracted from the real (measured) value. Assuming the sample is representative for the population, Equation 4.10 is used to obtain the standard deviation of the errors σ. In this equation, x is the error at a measurement point and $\bar{x}$ is assumed to be 0 with 0-mean normally distributed errors. The variable S is the total number of observations in the sample. As a result, a single value for $\sigma_{v,D_{tc}}$ and $\sigma_{v,D_{del}}$ is obtained.

$$\sigma \approx sd = \sqrt{\frac{\sum(x-\bar{x})^2}{S-1}} \tag{4.10}$$

Adaptive Model Parameters

As opposed to the static model parameters, adaptive model parameters in the PF algorithm will have different values for different particles. For that reason, the required output of the pre-training step in the pre-training flowchart (Figure 4.2) encompasses a pdf for the adaptive model parameters of the phenomenological relations to initialize particles with later in section 4.3. Therefore, the second set of training data (separated per specimen) is used to fit the relations for $\rho(N)$ (Equation 4.1) and $d_r(N)$ (Equation 4.4). It should be noted that model parameters in the aforementioned relations directly correspond to the evolution phenomenological relations used in the PF algorithm: $\Delta\rho(N, \Delta N)$ and $\Delta d_r(N, \Delta N)$. Once the best sets of model parameters a, b, c, d, e, f are obtained using NLS fitting for each specimen separately, it is desirable to learn the pdf of model parameters.

To learn the pdf of the distribution of a single adaptive model parameter, a histogram is made first with the number of bins determined by Sturges' rule (Equation 4.11). The derivation of Sturges' rule, which is widely used in statistics nowadays, is explained in more detail in Scott (2009). As a major disadvantage, Sturges' rule tends to make the histogram too smooth for larger sample sizes. However, it is in this case less relevant due to the generally limited number of specimens tested. Once this is done, a pdf is fit to the histogram. The best of four distributions is chosen (uniform, normal, Weibull, gamma) by minimizing the sum of squared errors (SSE).

$$\text{number of bins} = 1 + \log_2(\text{sample size}) \tag{4.11}$$

The standard deviations of the prediction method uncertainty $\sigma_{v,\rho,total}$ and $\sigma_{v,d_r,total}$ are estimated in a similar way as the static parameters by assuming 0-mean normally distributed

noise. However, this time, the standard deviations are considered on the training dataset and NLS phenomenological fits for each specimen separately. Both uncertainties for the $\rho(N)$ and $d_r(N)$ are transformed to the prediction method uncertainty of the crack density evolution $\sigma_{v,\rho}$ and delamination evolution σ_{v,d_r} using Equation 4.3 and Equation 4.6 respectively. As a last step, the pdf of the distribution of prediction uncertainties is once more chosen (uniform, normal, Weibull, gamma) by minimizing the SSE after fitting the statistical distributions to the histograms (bin size using Sturges' rule).

Finally, the last adaptive model parameter m needs pre-training. As mentioned previously in section 4.1, the parameter m is not depending on an observed phenomenological relation. It is rather an additional adaptive model parameter that is added in the PF algorithm to relate the percentage of total stiffness degradation in stage I to the normalized stiffness. For that purpose, the model parameter m is equivalent to $\frac{E_I}{E_0}$. This means it cannot be fit using NLS as done previously for the other model parameters. However, for each of the training specimens separately, one can observe a specific normalized stiffness at which the transition from stage I to stage II occurs using the $\frac{E_N}{E_0}$ data vs. cycles. Stage transition is previously defined in section 3.4 as a normalized stiffness degradation $\frac{E_N}{E_0}$ of less than 0.001 over 2500 cycles. However, as the measurement data are rather noisy to evaluate the failure definition, a running mean is applied with a pre-defined window size $WS_{smoothener}$ as user input. After this, the transition definition can be applied on the smooth data to obtain $m = \frac{E_I}{E_0}$ for each specimen. The final pdf for the model parameter m is then obtained following the same analogy as for the other adaptive model parameters by using the results of model parameter m for each specimen.

4.3 Initialization

The PF algorithm is a state-space dynamic model that consists of a state transition function and a measurement function. For this purpose, several vectors shall be defined and initialized for time step $t_n = 0$ before starting the online process. In this section, the definition of vectors and each their corresponding initialization is elaborated upon.

Damage State Vector

The damage state vector contains information on the damage state at time step t_n. As previously discussed in chapter 3, the damage properties of interest that reliably describe the damage process are: crack density ρ, delamination ratio d_r and the normalized stiffness $\frac{E_N}{E_0}$. Therefore, these are included in the damage state vector $\boldsymbol{x}$ with dimension $\mathbb{R}^3$ shown below.

$$\boldsymbol{x} = \left[\rho, d_r, \frac{E_N}{E_0}\right] \quad \in \mathbb{R}^3$$

It can be assumed that initially, the structure is free of defects, which initializes the state vector to $\boldsymbol{x_0} = [0, 0, 1]$ for all N_s particles. While it is mentioned in Axiom 1 in section 2.2 that all structures have inherent flaws or defects, the initialization is only a starting point after which the adaptivity of the PF algorithm can deal with these uncertainties.

Model Parameter Vector

Apart from the damage states, all N_s particles that are initialized must contain information on the underlying phenomenological models. An overview of all model parameters of the phenomenological relations is given in Table 4.2. Using those (for now excluding the prediction method uncertainties), the model parameter vector $\boldsymbol{\theta}$ is defined below with dimension $\mathbb{R}^{11}$. In this PF framework, it is preferred to store both static and adaptive model parameters in the model parameter vector for flexibility purposes if one would desire that specific static parameters are transformed to adaptive parameters.

$$\boldsymbol{\theta} = [a, b, c, d, e, f, h, i, j, k, m] \quad \in \mathbb{R}^{11}$$

In order to initialize the model parameter vector $\boldsymbol{\theta_0}$ for each of the N_s particles, the output of the pre-training process (section 4.2) is required. The static model parameters h, i, j and k are initialized to the same constant for each particle. On the other hand, N_s samples of each adaptive model parameter are drawn from distribution defined by the pdf output of the pre-training process. The samples for all model parameters are combined randomly to obtain N_s model parameter vectors.

In subsection 4.4.4, a random walk is added to the model parameters to allow $\boldsymbol{\theta}$ to continuously adapt. While this section does not deal with the details of the artificial dynamics, it is important to note that a matrix shall be initialized for the artificial noise Σ_{ξ_0} with dimensions $\mathbb{R}^{n_\theta \mathrm{X} n_\theta}$ (Chiachío et al., 2015a).

Model Error Vector

Along with the model parameters, the phenomenological relations involve static prediction method errors $\sigma_{v,D_{tc}}$ and $\sigma_{v,D_{del}}$, and adaptive prediction method errors $\sigma_{v,\rho}$ and σ_{v,d_r}. All prediction errors combined are referred to as the model error vector $\boldsymbol{v}$ with dimension $\mathbb{R}^4$ as shown below. In this PF framework, it is preferred to store both static and adaptive model errors in the model error vector for flexibility purposes.

$$\boldsymbol{v} = [\sigma_{v,\rho}, \sigma_{v,d_r}, \sigma_{v,D_{tc}}, \sigma_{v,D_{del}}] \quad \in \mathbb{R}^4$$

Initialization of the model error vector $\boldsymbol{v_0}$ for N_s particles is done by using the output of the pre-training process (section 4.2). The static model errors $\sigma_{v,D_{tc}}$ and $\sigma_{v,D_{del}}$ are initialized to the same value for each particle. On the other hand, N_s samples of are drawn from the pdf for the adaptive model errors $\sigma_{v,D_{tc}}$ and $\sigma_{v,D_{del}}$. By randomly combining each of the obtained model errors, N_s model error vectors are obtained.

Particles

The particles used in the PF algorithm each contain the state vector $\boldsymbol{z}$. As shown below, the state vector is the combination of the damage state vector $\boldsymbol{x}$, the model parameter vector $\boldsymbol{\theta}$ and the model error vector $\boldsymbol{v}$. It should be noted that at initialization, only the adaptive

model parameters and model errors differ. However, once transitioning and updating states in the PF algorithm, also the damage states of particles will differ. For the purpose of filtering (section 4.4), the weight vector is introduced next.

$$\boldsymbol{z} = [\boldsymbol{x}, \boldsymbol{\theta}, \boldsymbol{v}] \qquad \in \mathbb{R}^{18}$$

Weights and Failure Vector

To facilitate the PF algorithm filtering step, each particle is assigned a weight. This results in a weight vector $\boldsymbol{w}$ that contains N_s weights. Initially, no information is present at time step t_0, which means that it cannot be deduced whether a particle is more or less likely. Therefore, the weight vector is initialized as equally weighted particles as $\boldsymbol{w_0} = \left[\frac{1}{N_s}, \frac{1}{N_s}, ..., \frac{1}{N_s}, \frac{1}{N_s}\right]$. Similarly, at time step t_0, no degradation is present on the damage properties, which means that the failure vector $\boldsymbol{F_0} = [False, False, ..., False, False]$ with length N_s.

4.4 Filtering

Using the initialized vectors, the online process in the PF algorithm can be started. This is indicated by the black 'filtering' box in the flowchart in Figure 4.1. The complete sub-algorithm is displayed in Figure 4.3. A few building blocks are distinguished in PF. First, state transition of all particles is done in the prediction step (subsection 4.4.1) for each of the damage properties. Subsequently, the predictions are compared to the likelihood function based on incoming DIC measurements to update particle weights in subsection 4.4.2. In subsection 4.4.3, the condition for resampling of the regularized PF is elaborated upon along with the resampling algorithm. Finally, the artificial dynamics of model parameters is treated in subsection 4.4.4 to ensure the model parameters remain dynamic throughout the component's life.

4.4.1 Prediction

The posterior distribution at step t_{n-1} stored in the particles is propagated to the prior distribution at step t_n using the state transition function $t(\cdot)$ given in Equation 4.12. During the prediction process, only the damage state vector $\boldsymbol{x}$ is propagated, meaning that no transition is present in the model parameters and model errors. Therefore, $\boldsymbol{\theta} = \boldsymbol{\theta_{n-1}}$ and $\boldsymbol{v_n} = \boldsymbol{v_{n-1}}$. Using the properties of independence in Markov models, the prediction of $\boldsymbol{x_n}$ is conditionally independent of states prior to $\boldsymbol{x_{n-1}}$ given its Markov blanket (Barber, 2012).

$$\begin{aligned} \boldsymbol{\theta} &= \boldsymbol{\theta_{n-1}} \\ \boldsymbol{v_n} &= \boldsymbol{v_{n-1}} \\ \boldsymbol{x_n} &= \boldsymbol{t}(\boldsymbol{x_{n-1}}, \boldsymbol{\theta}, \boldsymbol{v_n}) \end{aligned} \tag{4.12}$$

The transition function $t(\cdot)$ is broken down into the three damage states: crack density ρ, delamination ratio d_r and normalized stiffness $\frac{E_N}{E_0}$. The state transition for each damage state is shown in Equation 4.13. The damage evolution for ρ and d_r, given in Equation 4.2 and Equation 4.5 respectively, is added to the damage state at t_{n-1}. The model parameters a, b, c,

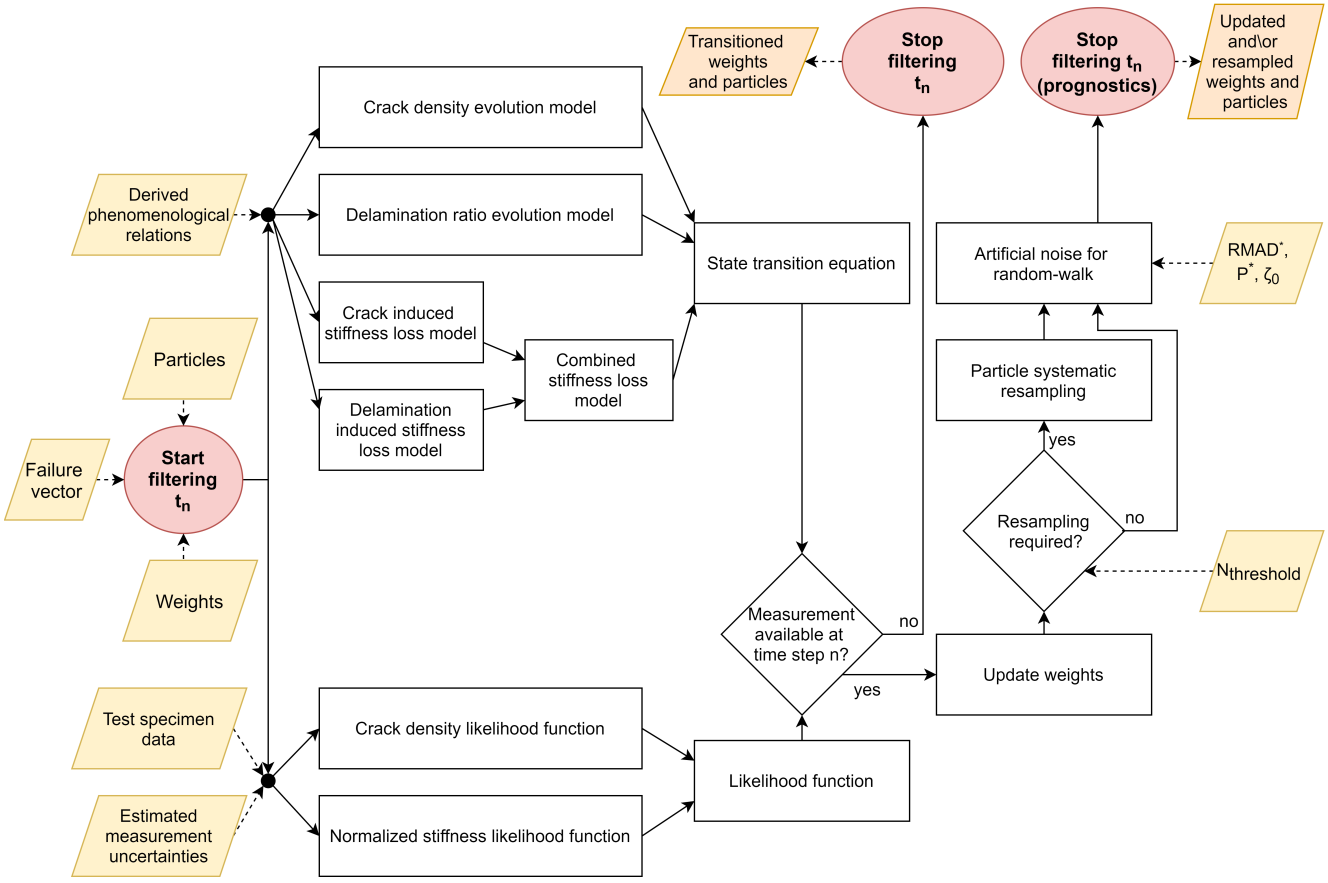

Figure 4.3: Flowchart of the filtering algorithm with inputs (yellow) and outputs (orange).

d, e and f depend on each particle separately and are therefore variables in the state transition equation. On the other hand, the state transition equation for the normalized stiffness of a particle obtained by combining Equation 4.7, Equation 4.8 and Equation 4.9. Here, the model parameters h, i, j, k and m are involved. One should note that all prediction method errors have previously been defined as 0-mean normally distributed variables. By making the assumption that each measurement noise is independent of one another, the damage state variables are decoupled (Chiachío et al., 2015a). This results in the factorization shown in Equation 4.14.

$$\begin{aligned}
\rho_n &= \rho_{n-1} + \Delta\rho\left(N, \Delta N, a, b, c\right) + v_{\rho,n} \\
d_{r,n} &= d_{r,n-1} + \Delta d_r\left(N, \Delta N, d, e, f\right) + v_{d_r,n} \\
\left(\frac{E_N}{E_0}\right)_n &= (m-1)\cdot\left[D_{tc}\left(\rho_n, h, i\right) + v_{D_{tc,n}} + D_{del}\left(d_{r,n}, j, k\right) + v_{D_{del},n}\right] + 1
\end{aligned} \tag{4.13}$$

$$\begin{aligned}
P\left(\boldsymbol{x}_n \,|\, \boldsymbol{x}_{n-1}, \boldsymbol{\theta}, \boldsymbol{v_n}\right) = & P\left(\left(\frac{E_N}{E_0}\right)_n \,\middle|\, \rho_n, d_{r,n}, \boldsymbol{\theta}, \boldsymbol{v_n}\right) \cdot \\
& P\left(d_{r,n} \,|\, d_{r,n-1}, \boldsymbol{\theta}, \boldsymbol{v_n}\right) \cdot \\
& P\left(\rho_n \,|\, \rho_{n-1}, \boldsymbol{\theta}, \boldsymbol{v_n}\right)
\end{aligned} \tag{4.14}$$

4.4.2 Updating

While the model parameters remain unchanged in the prediction step, they are now updated using a likelihood function and the incoming DIC measurement at the current time step t_n. In the online process of this thesis, it is decided to only use the crack density ρ and normalized stiffness $\frac{E_N}{E_0}$ for updating in the PF algorithm. This can be observed in Table 4.1. Equation 4.15 describes the state-space response to incoming measurements. Therefore, they are both contained in the measurement vector $\boldsymbol{y} = \left[\bar{\rho}, \frac{\bar{E_N}}{E_0}\right]$ with dimension $\mathbb{R}^2$. For clarity purposes, the bar indicates a measurement of a damage property. First, the measurement uncertainties contained in the measurement error vector $\boldsymbol{q}$ for this specific case study are quantified. Using this, the likelihood function can be defined and used to update the importance weights afterwards.

$$\mathbf{y_n} = \mathbf{x}_n + \mathbf{q_n} \tag{4.15}$$

Measurement Uncertainties

Both measurements contained in the measurement vector $\boldsymbol{y}$ have inherent uncertainties. In this case, it is assumed that measurement errors are 0-mean normally distributed, which makes it possible to quantify them as standard deviations $\sigma_{q,\rho}$ and $\sigma_{q,\frac{E_N}{E_0}}$. In chapter 3, the measurement techniques were explained on which this analysis is based.

Cameras capture the number of cracks on both edges of the cross-ply composite laminate during testing. The number of cracks, which is required to calculate the crack density, was determined as the average of crack number at both edges in the dataset. Only a single crack density is the result, which means that the deviation in the number of cracks between both

edges can be considered to estimate the measurement error. Additionally, the gauge length (which slightly differs for each specimen) influences the crack density measurement as only cracks within the viewing window are counted. However, compared to the deviation in cracks between the two edges, the DIC measurement error along the y-axis obtained from Vic-3D is negligibly small. Therefore, it is assumed that the only contributor to the measurement uncertainty in the crack density ρ is comes from the deviation between two edges.

In Table 4.3, the required information is shown to estimate the measurement uncertainty of the crack density. This includes the number of cracks at both edges at CDS (n_1 and n_2), the gauge length measured by DIC, and the crack density as a result of both. The standard deviation of the crack density σ is calculated using Equation 4.16, in which the assumption is made that the gauge length measurement does not contribute to the uncertainty to cancel out the part depending on the gauge length. Additionally, $n_c = mean(n_1, n_2)$ and $\sigma n_c = std(n_1 - n_2) = 2.035$ cracks. As a result, the average σ is concluded to be the measurement uncertainty of the crack density $\sigma_{q,\rho} = 0.0257$.

$$\frac{\sigma}{\rho} = \sqrt{\left(\frac{\sigma_{n_c}}{n_c}\right)^2 + \cancel{\left(\frac{\sigma_{GL}}{GL}\right)^2}} \iff \sigma = \rho \cdot \frac{\sigma_{n_c}}{n_c} \tag{4.16}$$

Table 4.3: Crack Density Measurement Uncertainty Determination

Spec.	Transverse Cracks CDS [−]				DIC CDS [mm]	Crack Density CDS [$\frac{1}{mm}$]	
	n_1	n_2	$mean(n_1, n_2)$	$n_1 - n_2$	Gauge Length (GL)	$\frac{mean(n_1,n_2)}{GL}$	σ
1-1	22	20	21	2	79	0.266	0.0258
1-2	17	16	16.5	1	77	0.214	0.0264
1-3	28	29	28.5	-1	81.5	0.350	0.0250
1-4	22	24	23	-2	79	0.291	0.0258
2-1	16	18	17	-2	78.5	0.217	0.0259
2-2	28	28	28	0	80.59	0.347	0.0253
2-3	19	23	21	-4	79.07	0.266	0.0257

The stiffness measurement is independent of the crack density measurement. While one could estimate the uncertainty of the DIC displacement measurement in the y-direction σ_y from Vic-3D ($\sigma_y \approx 0.00112$ mm), this only encompasses a small amount of the total uncertainty in the stiffness measurement. It is therefore assumed to estimate $\sigma_{q,\frac{E_N}{E_0}} = 0.02$. It is reasoned that the stiffness measurement shall have a certain degree of uncertainty to ensure effective sampling. This phenomenon has been observed during small-scale test runs with a very small measurement uncertainty (steep bell-curve around the measurement), resulting in random behavior as essentially all particles have the same inconsiderable likelihood. A visualization of this behavior is shown in Figure 4.4.

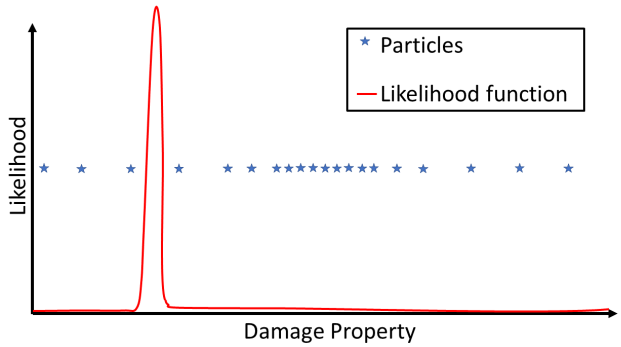

Figure 4.4: Visualization of a very small measurement uncertainty (steep bell-curve) around the measured property, resulting in equally small likelihoods for all particles and thus random behavior.

Likelihood Function and Weight Updating

On each sample with the propagated degradation property in $\boldsymbol{x_n}$ after the prediction step, the probability of obtaining measurement y_n is calculated. The likelihood is expressed by Equation 4.17 in which both measurements are combined. It shall be noted that this is only possible as the measurements, as previously discussed, are assumed to be independent.

$$P\left(\mathbf{y}_n \mid \mathbf{x}_n, \boldsymbol{\theta}, \boldsymbol{v_n}\right) = P\left(\bar{\rho}_n \mid \rho_n\right) P\left(\left(\frac{\bar{E_N}}{E_0}\right)_n \middle| \left(\frac{E_N}{E_0}\right)_n\right) \tag{4.17}$$

Revisiting the assumption of 0-mean normally distributed noise functions for both measurements, one can express both terms in the factorization as displayed in Equation 4.18. However, it is important to note that a PF can deal with any other type of noise as well as a non-linear model, as long as the likelihood function of the measurement is known beforehand. Therefore, the technique also provides a feasible solution for problems where linearization and the Gaussian noise distribution assumption would result in a lack of performance (Gordon et al., 1993; Srini, 2019).

$$\begin{aligned} P\left(\bar{\rho}_n \mid \rho_n\right) &= \frac{1}{\sqrt{2\pi}\sigma_{q_\rho}} \exp\left(-\frac{\left(\bar{\rho}_n - \rho_n\right)^2}{2\sigma_{q_\rho}^2}\right) \\ P\left(\left(\frac{\bar{E_N}}{E_0}\right)_n \middle| \left(\frac{E_N}{E_0}\right)_n\right) &= \frac{1}{\sqrt{2\pi}\sigma_{q_{\frac{E_N}{E_0}}}} \exp\left(-\frac{\left(\left(\frac{\bar{E_N}}{E_0}\right)_n - \left(\frac{E_N}{E_0}\right)_n\right)^2}{2\sigma_{q_{\frac{E_N}{E_0}}}^2}\right) \end{aligned} \tag{4.18}$$

The un-normalized weight of a particle $\hat{w}_n^i$ is determined in the updating step based on the likelihood of the particle by using Equation 4.19. Here, w_{n-1}^i is the weight of the previous particle, which incorporates information of prior states into the current state.

$$\hat{w}_n^i \propto w_{n-1}^i \cdot P\left(\boldsymbol{y}_n \mid \boldsymbol{x_n^i}, \boldsymbol{\theta}^i, \boldsymbol{v_n^i}\right) \text{ where } i = 1, \ldots, N_s \tag{4.19}$$

Subsequently, the weights are normalized to w_n^i such that the sum of all N_s weights equals 1 (Equation 4.20).

$$w_n^i = \frac{\hat{w}_n^i}{\sum_{i=1}^{N_s} \hat{w}_n^i} \text{ where } i = 1, \ldots, N_s \tag{4.20}$$

The process so far in the filtering step reflects a SIS PF strategy as discussed in subsection 2.3.2. However, the risk of weight degeneracy exists, which is dealt with in the resampling step.

4.4.3 Resampling

After assigning normalized weights to particles, the weight degeneracy can occur when no resampling (SIS) is done. This phenomenon means that low-weighted particles remain present. Therefore, the predictions are dependent on only a few particles with higher weights, which decreases the accuracy of the predictions and increases the variance of the posterior distribution (Li et al., 2015). Ideally, all particles have equal weights so that the model parameters and degradation properties can be derived from the posterior distribution only (Kim et al., 2016). While a PF algorithm with resampling (SIR) reduces the problem of weight degeneracy, it introduces sample impoverishment. Sample impoverishment indicates the problem that high weight samples are likely to be extracted multiple times during resampling, while low weight samples are unlikely to be drawn. This means that the variety of samples decreases and eventually collapses into a set of unique samples. Therefore, in this thesis, a regularization is added to combine SIS and SIR by only resampling if the effective sample size drops below a pre-determined threshold. When resampling has occurred, all importance weights are reset to the initial weight vector $\boldsymbol{w} = \left[\frac{1}{N_s}, \frac{1}{N_s}, ..., \frac{1}{N_s}, \frac{1}{N_s}\right]$.

Resampling is required once degeneracy is encountered, which means that this does not need to happen at every time step in the regularized PF algorithm. Therefore, the effective sample size N_{eff} is introduced as a trigger for the resampling algorithm. This estimated effective sample size is calculated using Equation 4.21 (Li et al., 2015). Following this analogy, when $N_{eff}(t) \leq N_{threshold}$, resampling is required. Additionally, resampling occurs at every time step (SIR) when $N_{threshold} = 1$, and resampling never occurs (SIS) when $N_{threshold} = 0$.

$$N_{eff}(t) = \frac{1}{\sum_{i=1}^{N_s} w_i^2(t)} \tag{4.21}$$

As clarified in the literature review on resampling techniques (subsection 2.3.2), systematic resampling proves most suitable due to the constant sample size and its computational efficiency. The principle of this algorithm is visualized in Figure 2.8. In systematic resampling, constant steps are defined between two particles to be resampled. Therefore, a random number is selected in the first sub-interval u_n^1 as shown in Equation 4.22, after which a constant step is added to obtain the selection from subsequent sub-intervals u_n^i. The m^{th} particle is then selected to resample based on the condition in Equation 4.23 (Li et al., 2015).

$$\begin{aligned} u_n^1 &\sim \mathcal{U}\left(0, \tfrac{1}{N_s}\right] \\ u_n^i &= u_n^1 + \tfrac{i-1}{N_s} \text{ where } i = 2, \ldots, N_s \end{aligned} \tag{4.22}$$

$$Q_n^{m-1} < u_n^i \leq Q_n^m \quad \text{where } Q_n^m = \sum_{i=1}^{m} w_n^i \tag{4.23}$$

4.4.4 Random Walk

A commonly occurring problem after updating the states up to time step t_n is related to the inability of the model parameter vector $\boldsymbol{\theta}$ to adapt. Therefore, Chiachío et al. (2015a) presents a technique to explore the parameter space of $\boldsymbol{\theta}$ by adding an independent random perturbation ξ to transition the model parameter vector as $P(\boldsymbol{\theta_n} \mid \boldsymbol{\theta_{n-1}})$. This is described in Equation 4.24.

$$\boldsymbol{\theta}_n = \boldsymbol{\theta}_{n-1} + \boldsymbol{\xi}_n \tag{4.24}$$

By assuming a 0-mean normal distribution to transition model parameters to a next state, the model parameters after adding the random walk are obtained by Equation 4.25. The random walk vector $\boldsymbol{\xi_n}$ has dimension $\mathbb{R}^{11}$.

$$P\left(\boldsymbol{\theta_n} \mid \boldsymbol{\theta_{n-1}}\right) = \mathcal{N}\left(\boldsymbol{\theta_{n-1}}, \boldsymbol{\sigma_{\xi_n}}\right) \tag{4.25}$$

Daigle and Goebel (2013) stress the importance of tuning the random walk parameter, which in this case encompasses the random walk for each model parameter j: $\sigma_{\xi_{n,j}}$. A large random walk variance causes rapid convergence, while a too small random walk variance causes very slow convergence, if any. To use the random walk in the best possible way, methods in literature focus on a shrinkage of $\sigma_{\xi_{n,j}}$ over time. Such method has been proposed by Daigle and Goebel (2013) and is shown in Equation 4.26. Here, the random walk of the previous time step is multiplied with a shrinkage term under the square root. In the shrinkage term, P_j^* determines the rate of convergence (larger means faster convergence) to the target relative median absolute deviation (RMAD) RMAD_j^* (Chiachío et al., 2015a). Both are user inputs and their sensitivity on the PF algorithm results are discussed in more detail in chapter 5.

$$\sigma_{\xi_{n,j}} = \sigma_{\xi_{n-1,j}} \sqrt{1 - P_j^* \frac{\text{RMAD}\left(\theta_{n,j}\right) - \text{RMAD}_j^*}{\text{RMAD}\left(\theta_{n,j}\right)}} \tag{4.26}$$

The RMAD is used as a relative measure of spread (or variance) as shown in Equation 4.27. Therefore, it can be calculated for each model parameter $\theta_{n,j}$ taking into account the model parameter value in each of the N_s samples. One should note that for static model parameters, the RMAD will always be equal to zero, which means that no artificial noise is added.

$$\begin{aligned} \text{RMAD}\left(\theta_{n,j}\right) &= \frac{\text{median}\left(\left\{\left|\theta_{n,j}^i - \text{median}\left(\tilde{\theta}_{n,j}\right)\right|\right\}_{i=1}^{N_s}\right)}{\text{median}\left(\tilde{\theta}_{n,j}\right)} \\ \text{where } \tilde{\theta}_{n,j} &= \left\{\theta_{n,j}^1, \ldots, \theta_{n,j}^i, \ldots, \theta_{n,j}^{N_s}\right\} \end{aligned} \tag{4.27}$$

Initially, the random walk of the particles at time step t_0 is defined as a percentage of the inter-percentile range (IPR) for a model parameter between 0.05 and 0.95 $IPR_{j,0}(0.05, 0.95)$. From this point on, the previously mentioned equations and the pre-set value P_j^* are used to decrease the variance of the random walk. However, it is not desirable to have no random walk at all towards the end. Therefore, the target RMAD_j^* is required as user input as a percentage of the initial RMAD at time step t_0.

4.5 Prognostics

As a last step in the flowchart before moving to a next iteration, prognostics of future RUP (ρ, d_r and $\frac{E_N}{E_0}$) and prognostics of the RUL up to EOEFL is performed. The flowchart for this purpose is shown in Figure 4.5. As a starting point, the updated and resampled particles with additional random walk in the state vector z_n at time step t_n are copied. Along with this, a copy of the weight vector and the failure vector is made. Doing so, the original vectors will directly move to the next filtering iteration, while the copies of the vectors serve for the prognostics performed at time step t_n. In order to progress damage to t_{n+l}, state transition is elaborated upon first. Once future damage states are known, the pdf of the RUP can be determined using all N_s particles. Finally, the EOEFL failure criterion and associated RUL estimation are treated. One should note that progression of particles and assessment of failure is done for each particle separately in the PF algorithm.

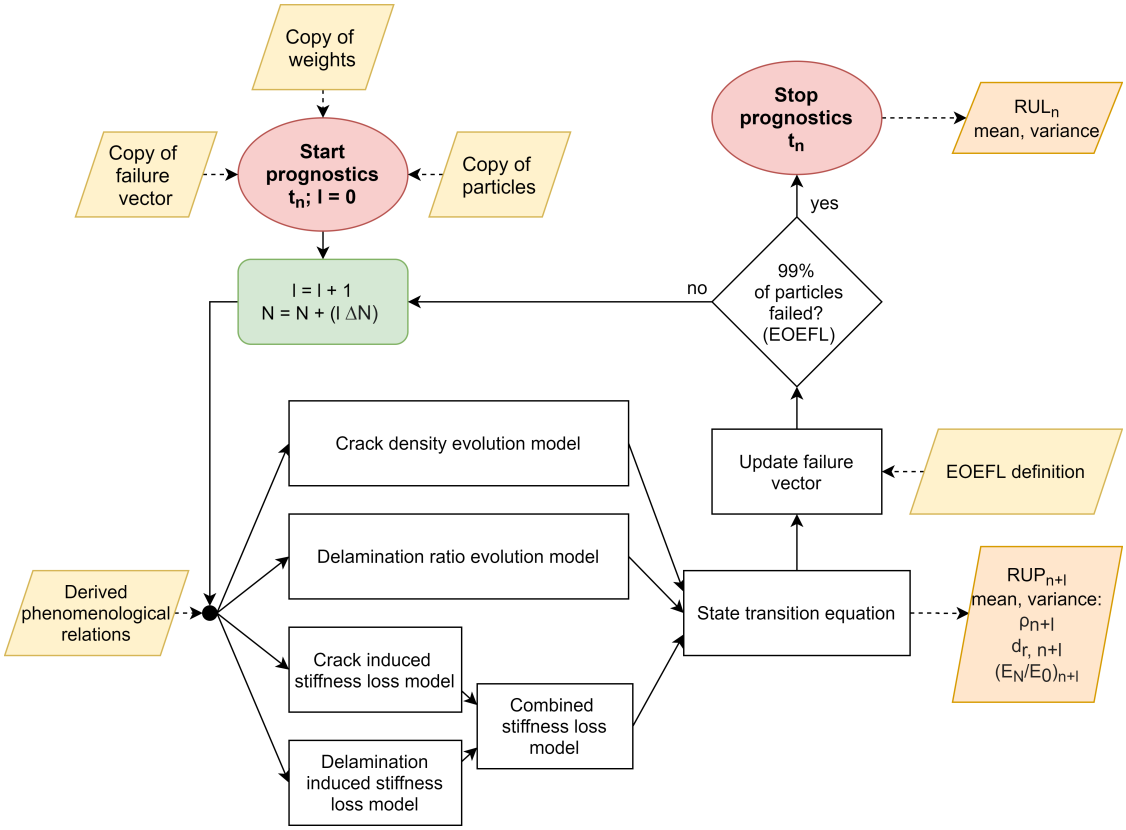

Figure 4.5: Flowchart of the prognostics algorithm with inputs (yellow) and outputs (orange).

4.5.1 State Transition

The state transition equations for prognostics are identical to those used in the filtering step of the online PF algorithm. Therefore, in prognostics, one starts at time step t_n, and calculate future states to time step t_{n+l}. This is illustrated by Equation 4.28, in which the damage state of each particle is propagated to future states using the state transition function $\boldsymbol{t}(\cdot)$.

More details on the governing phenomenological relations supporting the state transition can be obtained in subsection 4.4.1.

$$\mathbf{x}^{\mathbf{i}}_{\mathbf{n+l}} = \boldsymbol{t}\left(\mathbf{x}^{\mathbf{i}}_{\mathbf{n+l-1}}, \boldsymbol{\theta}^{\boldsymbol{i}}_{\boldsymbol{n}}, \boldsymbol{v}^{\boldsymbol{i}}_{\boldsymbol{n}}\right) \text{ where } i = 1, \ldots, N_s \tag{4.28}$$

4.5.2 Remaining Useful Properties Estimation

The RUP estimation refers to combining the damage states of all particles at time step t_{n+l} to a single estimate. However, it is assumed for the RUP estimation here that the damage states follow a normal distribution, which means a weighted mean and standard deviation (or variance) can be obtained. For that purpose, the weight vector at t_n, w_n is still considered to weight the importance of each particle. The mean of each RUP prediction can be obtained using Equation 4.29.

$$\begin{aligned}
\rho_{n+l} &= \sum_{i=1}^{N_s} \rho^i_{n+l} \cdot w^i_n \\
d_{r_{n+l}} &= \sum_{i=1}^{N_s} d^i_{r_{n+l}} \cdot w^i_n \\
\left(\frac{E_N}{E_0}\right)_{n+l} &= \sum_{i=1}^{N_s} \left(\frac{E_N}{E_0}\right)^i_{n+l} \cdot w^i_n
\end{aligned} \tag{4.29}$$

Similarly, the weighted variance of each RUP prediction is obtained using Equation 4.30. The variances are used later in the results (chapter 5) to generate prediction intervals.

$$\begin{aligned}
\sigma^2_{\rho_{n+l}} &= \sum_{i=1}^{N_s} \left(\rho^i_{n+l} - \rho_{n+l}\right)^2 \cdot w^i_n \\
\sigma^2_{d_{r_{n+l}}} &= \sum_{i=1}^{N_s} \left(d^i_{r_{n+l}} - d_{r_{n+l}}\right)^2 \cdot w^i_n \\
\sigma^2_{\left(\frac{E_N}{E_0}\right)_{n+l}} &= \sum_{i=1}^{N_s} \left(\left(\frac{E_N}{E_0}\right)^i_{n+l} - \left(\frac{E_N}{E_0}\right)_{n+l}\right)^2 \cdot w^i_n
\end{aligned} \tag{4.30}$$

4.5.3 End-Of-Early-Fatigue-Life Criterion and Remaining Useful Life Estimation

The failure vector $\boldsymbol{F}$ from the filtering process has been passed at t_n for prognostics purposes. The failure criterion in the filtering process and prognostics process is identical, and will therefore be explained only once here for both. Initially, at t_0, all N_s entries in the failure vector are $False$, which means no particle has reached EOEFL. As mentioned previously, the definition for EOEFL is less than 0.001 normalized stiffness degradation over 2500 cycles. Therefore, in the filtering process as well as prognostics process, the datapoints of the last 2500 cycles are stored in a temporary dataframe to track the stiffness degradation. In case a particle reaches EOEFL, the entry for that particle is set to $True$ in the failure vector.

In Equation 4.31, the RUL of the i^{th} particle at time step n in the filtering process is shown as a function of the number of cycles at which the particle reaches EOEFL. If a particle from the filtering process is copied to the prognostics process with $True$ (already failed), this automatically means the RUL is 0 for the prognostics. In any other case, state transition is done for that particle up to EOEFL.

$$\mathrm{RUL}_n^i = max\left(0, \mathrm{EOEFL}_n^i - t_n\right) \quad \text{where } i = 1, \ldots, N_s \tag{4.31}$$

In a similar way as the RUP estimation, the RUL can be estimated at t_n using the weighted mean and standard deviation of the RUL of all particles RUL_n^i. For that purpose, the weight vector at t_n, w_n is considered to weight the importance of each particle. The mean of each RUL prediction is obtained with Equation 4.32, while Equation 4.33 yields the variance.

$$\mathrm{RUL}_n = \sum_{i=1}^{N_s} \mathrm{RUL}_n^i \cdot w_n^i \tag{4.32}$$

$$\sigma_{RUL_n}^2 = \sum_{i=1}^{N_s} \left(RUL_n^i - \tilde{RUL_n}^i\right)^2 \cdot w_n^i \tag{4.33}$$

4.6 Performance Evaluation

Once the EOEFL threshold is reached in the PF algorithm, the performance of a specific algorithm for the test specimen is evaluated with evaluation metrics and the complete set of test data. For this purpose, at each discrete time step $t_\mathrm{i}\ \varepsilon\ [1, k]$ an DIC measurement is recorded. For the current case study data, this means every 500 cycles. As this thesis deals with prognostics and RUL estimation, it is decided to evaluate performance based on the RUL to EOEFL.

At each time step t_i, the error E_m between the actual value and the observed value can be calculated using Equation 4.34. This involves $\mathrm{RUL}_{\mathrm{actual}}$, which is the absolute value of the difference between the number of cycles at stage transition (the EOEFL) and the number of cycles at time step t_i. Additionally, as a result of the prognostics step, the mean of the RUL for all particles at time step t_i is known and can be used to obtain the error E_m. As performance metrics, the precision, root mean squared error (RMSE), mean absolute percentage error (MAPE), cumulative relative accuracy (CRA) and convergence are adopted from Eleftheroglou et al. (2018).

$$E_m\left(\mathrm{t_i}\right) = \mathrm{RUL}_{\mathrm{actual}}\ \left(\mathrm{t_i}\right) - \mathrm{mean}\left[\mathrm{RUL}\left(\mathrm{t_i}\right)\right] \tag{4.34}$$

In forecasting applications, the precision is used to give a measure of spread. In this work, the precision of the PF algorithm is calculated with Equation 4.35. It is desirable to minimize precision, indicating that predictions are close to each other (Eleftheroglou et al., 2018).

$$\text{Precision} = \sqrt{\frac{\sum_{i=1}^{k}\left(E_m\left(\mathrm{t}_i\right) - \overline{E_m}\left(\mathrm{t}_i\right)\right)^2}{k-1}} \quad \text{where } \overline{E_m} = \frac{\sum_{i=1}^{k} E_m}{k} \tag{4.35}$$

While precision gives a measure of spread, the RMSE evaluates the accuracy (or correctness)of the model. More specifically, one can interpret the RMSE as the average error of the predictions which is independent of the direction of the error. It is desirable to minimize the RMSE (Persson and Ståhl, 2020).

$$\text{RMSE} = \sqrt{\frac{\sum_{\mathrm{i}=1}^{k}\left(E_m\left(t_i\right)\right)^2}{k}} \tag{4.36}$$

The MAPE is a commonly used evaluation metric for forecasting purposes that gives an intuitive interpretation of the relative error. It should be noted that the MAPE can only be calculated when $\text{RUL}_{\text{actual}} > 0$ to avoid division by zero. This means the MAPE can be computed for all measurement points up to the time step before EOEFL. To obtain a model with high accuracy, it is desirable to minimize the MAPE (de Myttenaere et al., 2016).

$$\text{MAPE} = \frac{1}{k}\sum_{\mathrm{i}=1}^{k}\left|\frac{100 \cdot E_m\left(t_i\right)}{\text{RUL}_{\text{actual}}\left(t_i\right)}\right| \tag{4.37}$$

The CRA metric evaluates the Relative Accuracy (RA) multiple times to obtain and aggregate accuracy level. This reflects the algorithm's behavior more generally than the RA, which only discloses information about a single time instance. The CRA is calculated using Equation 4.38, in which the condition $\text{RUL}_{\text{actual}} > 0$ should again be satisfied to avoid division by 0. This means the CRA can be computed for all measurements points up to the time step before reaching EOEFL. It is desirable to maximize the CRA (Goebel et al., 2012).

$$\text{CRA} = \frac{\sum_{\mathrm{i}=1}^{k}\text{RA}\left(t_i\right)}{k} \quad \text{where } \text{RA}\left(t_i\right) = 1 - \left|\frac{E_m\left(t_i\right)}{\text{RUL}_{\text{actual}}\left(t_i\right)}\right| \tag{4.38}$$

Finally, the convergence expresses at which rate the error E_m improves over time. In order to do so, the variables x_c and y_c are introduced as the center of mass of the area under the curve describing the absolute value of the error $|E_m(i)|$ over time. The convergence metric is then defined as the distance between the origin and the centroid (x_c, y_c). When this distance is smaller, and thus the convergence metric is smaller, convergence happens faster in time. Therefore, it is desirable to minimize the convergence metric (Goebel et al., 2012).

$$\begin{aligned}
&\text{Convergence} = \sqrt{\left(x_c - t_i\right)^2 + y_c^2} \\
&\text{where } x_c = \frac{\sum_{\mathrm{i}=1}^{k-1}\left(t_{i+1}^2 - t_i^2\right) \cdot |E_m(\mathrm{i})|}{2 \cdot \sum_{\mathrm{i}=1}^{k-1}\left(t_{i+1} - t_i\right) \cdot |E_m(\mathrm{i})|} \\
&\text{and } y_{\mathrm{c}} = \frac{\sum_{\mathrm{i}=1}^{k-1}\left(t_{i+1} - t_i\right) \cdot E_m(\mathrm{i})^2}{2 \cdot \sum_{\mathrm{i}=1}^{k-1}\left(t_{i+1} - t_i\right) \cdot |E_m(\mathrm{i})|}
\end{aligned} \tag{4.39}$$

Chapter 5

Case Study Results and Discussion

This chapter details the results of the PF methodology established in chapter 4 on the case study data (chapter 3). First, the virtual test set-up (soft- and hardware) is set out in section 5.1. After this, the results of the RUL prognostics of all specimens are discussed in section 5.2. In order to identify strengths and weaknesses of the PF algorithm, a strong performer (specimen 1-4 in section 5.3) and a weak performer (specimen 2-2 in section 5.4) are focused on in a more detailed discussion. For these specimens, additional information on RUP and evolution of model parameters is added. This chapter concludes with a sensitivity analysis (section 5.5) of the PF hyperparameters.

5.1 Available Hardware and Software

As the prognostics step of the PF requires significant computational effort, it was important to know which software and hardware was available. As hardware, a personal HP ZBook Studio G5 laptop was continuously present to generate the results presented in this chapter. The laptop has the following specifications:

- **Operating System:** Microsoft Windows 10 Home
- **Processor:** Intel Core i7-8750H CPU @ 2.2GHz, 6 cores
- **Disk Space:** 256GB
- **RAM:** 16GB

These system specifications have proven to meet the requirements for this thesis project. As software tool, Python 3.8 is used with several libraries that are designed for machine learning (Python). These libraries include Numpy 1.18.1, SciPy 1.4.1, Matplotlib 3.1.3 and Pandas 1.0.3 (Numpy; SciPy; Matplotlib; Pandas). Other more general Python libraries are available, and additional libraries can be downloaded if required. Throughout the thesis, for transparency and analysis purposes, RUP, RUL and model parameter data are saved for each iteration by pickling all stored variables after the PF algorithm has stopped.

5.2 Remaining Useful Life Prognostics Results

In this section, the results of the RUL prognostics of all specimens in the case study dataset, as given in chapter 3, are presented. The observed phenomena will be discussed here, after which a more in-depth analysis later in the report will help to understand this behavior. The methodology established in chapter 4 is used for that purpose. All user inputs for the PF algorithm are shown in Table 5.1. Among these input parameters, RMAD_j^* and $\xi_{j,0}$ are design choices that depend on the allowed spread in EOEFL predictions and on the allowed initial spread. Furthermore, ΔN influences the accuracy of the evolution model as it is approximated as a linear growth from t_{n-1} to t_n with the derivative of the observed relations in Equation 4.1 and Equation 4.4 as slope. The other inputs N_s, $\text{N}_{threshold}$ and P^* are hyperparameters of the PF algorithm that can be tuned to improve predictions.

Additionally, it is worth mentioning that a maximum number of iterations is introduced on both the filtering and prognostics algorithms to prevent infinite looping. This is supported by observations made in the PF behavior for specimen 2-2 (section 5.4). In this case study, it is decided to limit iterations to 100,000 cycles. This means that, if a particle has not failed at this point, the RUL is set to 100,000 cycles and future states are no longer explored. Another adjustment made to prevent early stopping of the PF algorithm in this specific case is that the failure criterion is only activated when the normalized stiffness $\frac{E_N}{E_0} \leq 0.96$. Otherwise, a very small slope could be detected on the upper plateau as clearly observable for specimen 2-1 (Figure 5.4c).

Table 5.1: PF User Inputs for RUL Prognostics to EOEFL

User Input Parameter	Value
Training Spec.	{Spec. : Spec. $\neq$ Testing Spec.}
$\text{WS}_{smoothener}$	20
N_s	1,500
ΔN	250
$\text{N}_{threshold}$	0.95
P^*	1E-3
RMAD_j^*	0.2 $\cdot\text{RMAD}_{j,0}$
$\xi_{j,0}$	0.00025 $\cdot\text{IPR}_{j,0}(0.05, 0.95)$

In the PF algorithm, the weighted mean and standard deviation of the RUL predictions and damage properties are stored at every filtering and prognostics time step (Equation 4.29 - 4.33). This means that it is always assumed that particles are normally distributed. As a result, the 95 % prediction interval (PI) can be constructed in this chapter around the weighted mean using Equation 5.1, in which $\bar{X}$ and σ_X denote the weighted mean and standard deviation of property X respectively. It is important to mention that the PI lower bound in some cases has a small negative value for damage properties and/or RUL predictions, which is highly unlikely. This does not necessarily mean that some particles have an actual negative value for that property, but it rather shows the shortcomings of estimating properties by assuming a normal distribution. In some cases, a normal-like distribution is observed, while in other cases it is not. However, this assumption is made to compactly capture and report information on the spread of particles for a particular property.

$$95\%\ \text{PI} = \bar{X} \pm \sqrt{\left(1 + \frac{1}{N_s}\right) \cdot \sigma_X^2} \tag{5.1}$$

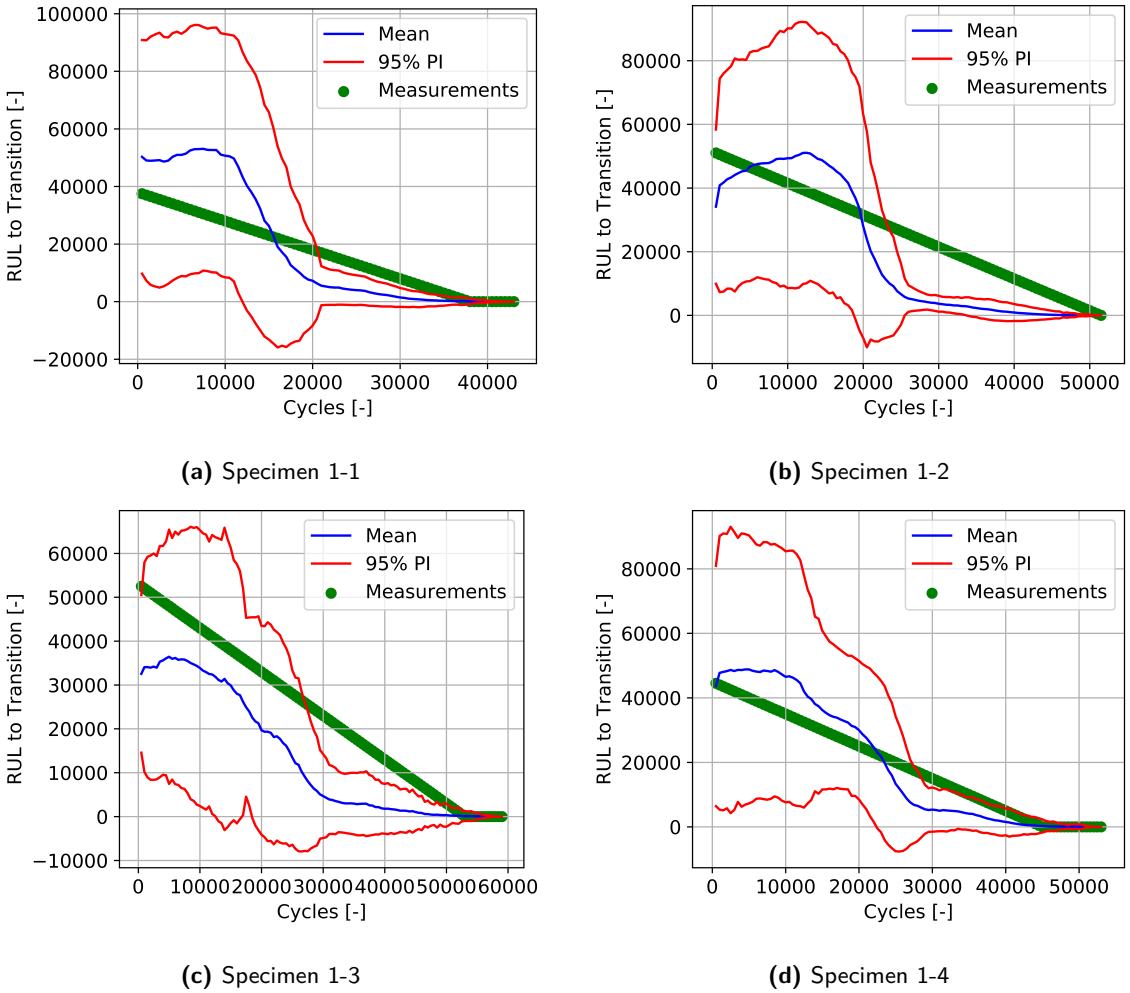

(a) Specimen 1-1

(b) Specimen 1-2

(c) Specimen 1-3

(d) Specimen 1-4

Figure 5.1: Results of remaining useful life (RUL) prognostics (specimen group 1) for stage I to II transition with indicative weighted mean and 95% prediction interval (PI) of the N_s particles.

The results of the RUL predictions to EOEFL (or stage I to stage II transition) with the aforementioned PF user inputs are shown in Figure 5.1 and Figure 5.2 for specimen group 1 and 2 respectively. The aforementioned weighted mean of the RUL_n prediction at t_n cycles is indicated in blue, while the 95% PI is plotted in red including a lower and upper bound. The actual RUL to EOEFL of each specimen, obtained using measurements, is shown in green at each time step at which a measurement is present. This actual RUL is obtained by subtracting the number of cycles at which transition occurs by the number of cycles at the time step of interest. The number of cycles at transition is obtained using a similar methodology as was used for the model parameter m (section 4.2). This means that a running mean is first applied to the normalized stiffness of the testing specimen with window size $\text{WS}_{smoothener}$,

after which EOEFL is identified as the first time step at which less than 0.001 normalized stiffness degradation occurs over 2500 cycles. However, while the normalized stiffness was previously of interest for model parameter m, now the number of cycles at transition is used in the calculation to obtain the actual RUL.

First, the RUL predictions to EOEFL for specimen group 1 are presented (Figure 5.1). One can observe that for all group 1 specimens, the RUL is constant or increasing in approximately the first 12,000 cycles. After this point, a distinct sudden drop in RUL is observed for specimen 1-1 (Figure 5.1a) and 1-2 (Figure 5.1b). In specimen 1-3 (Figure 5.1c) and 1-4 (Figure 5.1d), this behavior is less explicit. Additionally, it is apparent that for all specimens, the prediction intervals shrink over the lifetime. This indicates less spread appears in the RUL predictions when moving towards EOEFL.

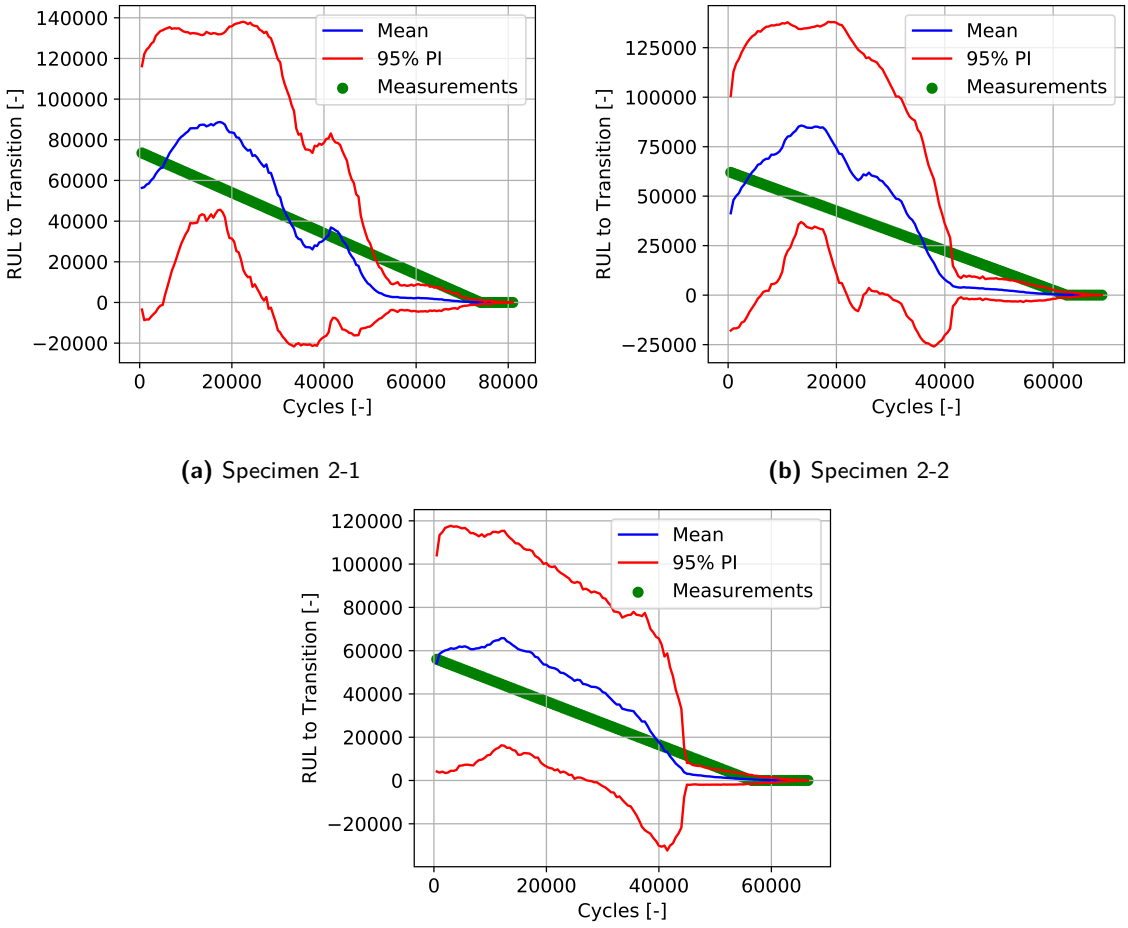

(a) Specimen 2-1

(b) Specimen 2-2

(c) Specimen 2-3

Figure 5.2: Results of remaining useful life (RUL) prognostics (specimen group 2) for stage I to II transition with indicative weighted mean and 95% prediction interval (PI) of the N_s particles.

Secondly, the RUL predictions to EOEFL for specimen group 2 are presented (Figure 5.2). One can observe that for all group 2 specimens, the RUL is constant or increasing in approximately the first 20,000 cycles. After this point, a distinct drop in RUL can be seen for specimen 2-2 (Figure 5.2b) in which the RUL decreases with approximately 55,000 cycles between $t_n \approx 25,000$ cycles and $t_n \approx 40,000$ cycles. In specimen 2-1 (Figure 5.2a) and 2-3 (Figure 5.2c), this behavior is less expressive. Additionally, it is apparent that the PI for all specimens reduce in the last 20,000 cycles of a specimen's lifetime. This is consistent with a plateau region in the phenomenological relation $\rho(N)$ (meaning no crack growth) and with a plateau region in $D_{del}(d_r)$ (meaning no additional delamination induced stiffness degradation) towards EOEFL.

Apart from the previously shown plots of the RUL to transition (EOEFL), the performance metrics are applied based on the error E_m as calculated in Equation 4.34. Therefore, only the weighted mean is required, meaning it is not dependent on the normality assumption in contrast to the prediction interval visualizations. The precision, RMSE, MAPE, CRA and convergence are obtained using the RUL prognostics of each specimen following the methodology in section 4.6. The results are shown in Table 5.2.

Table 5.2: Performance Metrics Results per Specimen of RUL prognostics to EOEFL

Specimen	Precision	RMSE	MAPE	CRA	Convergence
1-1	11,507.17	11,739.77	63.632	0.364	15,621.336
1-2	10,098.93	11,571.23	58.327	0.417	26,785.481
1-3	5,555.73	11,509.04	57.447	0.426	24,673.576
1-4	**6,646.292**	**6,685.92**	**39.185**	**0.608**	**19,941.175**
2-1	14,934.92	15,090.6	47.006	0.53	31,556.781
2-2	**17,107.87**	**18,426.19**	**59.924**	**0.401**	**27,338.085**
2-3	8,978.045	11,385.06	44.584	0.554	23,740.206

Among the results presented in Table 5.2, it is apparent that specimen 1-4 scores particularly good in terms of the accuracy metrics RMSE, MAPE and CRA. On the other hand, specimen 2-2 scores particularly weak in terms of all metrics. Therefore, those are indicated in bold and will be treated extensively in section 5.3 and section 5.4 respectively. This will provide more insight in the applied methodology, and it will uncover apparent strengths and weaknesses of the methodology. For the other specimens, visualizations of the RUP prognostics are added in Appendix A.

5.3 Extensive Results of Specimen 1-4

In this section, the results of specimen 1-4 are presented in extensive detail. This specimen is a particularly good performer of the PF as mentioned in section 5.2. The results of RUL prognostics for stage I to II transition with indicative weighted mean and 95% PI of the N_s particles has been presented in Figure 5.1d. The RUL results are dependent on all preceding steps, being pre-training, filtering and RUP prognostics. Therefore, the results for each of these steps is discussed in the following subsections.

5.3.1 Pre-Training

In the pre-training step, the training specimens, being the set of all specimens except for the testing specimen, are used to serve as input for the initialization of particles in the PF algorithm. A flowchart of this step has been shown in Figure 4.2. A distinction is once more made between static and adaptive model parameters.

Static Model Parameters

First, the focus is on the static model parameters h, i, j and k. These are pre-trained using NLS on the combined dataset of the training specimens all together to obtain a single value for each. Those will serve in the PF algorithm to describe the crack induced stiffness degradation relation $D_{tc}(\rho)$ (Equation 4.7) and the delamination induced stiffness degradation relation $D_{del}(d_r)$ (Equation 4.8). The results of the NLS fits using scipy.curve_fit are shown in Figure 5.3.

The crack induced stiffness degradation model parameters (Figure 5.3a) are $h = 1.016$ and $i = -0.004$. Following the methodology, a single uncertainty is obtained as standard deviation of the 0-mean normal distribution $\sigma_{v,D_{tc}} = 0.0416$. Similarly, the delamination induced stiffness degradation model parameters (Figure 5.3b) are $j = -0.711$ and $k = -69.086$ and the uncertainty is again obtained as the standard deviation $\sigma_{v,D_{del}} = 0.0578$.

Adaptive Model Parameters

After the static model parameters, the focus moves to the adaptive model parameters a, b, c, d, e, f and m. It is noted once more that these will serve to initialize the PF with different values for the same model parameter for each particle. The first six model parameters are pre-trained using NLS (scipy.curve_fit) on each training specimen separately to describe the crack growth $\Delta\rho(N, \Delta N)$ (Equation 4.2) and delamination growth $\Delta d_r(N, \Delta N)$ (Equation 4.5). Additionally, the model parameter m required for the phenomenological relation $\frac{E_N}{E_0}(D_{tc}, D_{del})$ (Equation 4.9) is obtained by smoothing the normalized stiffness and applying the EOEFL criterion. As a result, the NLS fits and state transition model parameter m are shown in Figure 5.4. The corresponding values for each specimen are listed in Table 5.3.

Table 5.3: NLS Fits of Adaptive Model Parameters per Training Specimen (Pre-Training 1-4)

	Crack Growth			Delamination Growth			Stiffness
Spec.	a	b	c	d	e	f	m
1-1	0.272	-0.106E-3	610	0.084	0.932E-4	23,929	0.916
1-2	0.222	-0.924E-4	1,011	0.198	0.144E-3	33,323	0.894
1-3	0.354	-0.125E-3	1,213	0.092	0.377E-4	77,001	0.907
2-1	0.235	-0.509E-4	10,689	0.140	0.114E-3	58,826	0.899
2-2	0.357	-0.834E-4	9,364	0.041	0.144E-3	46,549	0.899
2-3	0.285	-0.463E-4	2,067	0.049	0.137E-3	50,754	0.919

The standard deviations $\sigma_{v,\rho,total}$ and $\sigma_{v,d_r,total}$ are obtained as the NLS error distribution for $\rho(N)$ and $d_r(N)$ of each specimen separately. However, in the PF algorithm, the prediction method error standard deviations of the growth relations $\sigma_{v,\rho}$ and σ_{v,d_r} are required. To do so, Equation 4.3 and Equation 4.6 are used with all parameters presented in Table 5.4.

Table 5.4: NLS Adaptive Model Parameter Errors per Training Specimen (Pre-Training 1-4)

	Crack Growth		Delamination Growth	
Spec.	$\sigma_{v,\rho,total}$	$\sigma_{v,\rho}$	$\sigma_{v,d_r,total}$	σ_{v,d_r}
1-1	7.01E-3	3.97E-5	2.15E-3	1.22E-5
1-2	8.79E-3	4.98E-5	2.87E-3	1.63E-5
1-3	1.16E-2	6.59E-5	2.32E-3	1.31E-5
2-1	1.12E-2	6.32E-5	1.89E-3	1.07E-5
2-2	9.37E-3	5.30E-5	9.55E-4	5.40E-6
2-3	1.13E-2	6.41E-5	1.19E-3	6.76E-6

While multiple statistical distributions are defined in the methodology and in the algorithm, all model parameters and prediction method errors are initialized as a uniform distribution as this gives the lowest SSE on the histograms with the bin size defined by Sturges' rule. This is due to the small size of the training set (six specimens). However, the framework to support multiple distribution is present for future applications to maximize information retrieval (specific statistical distribution) once the training dataset is larger.

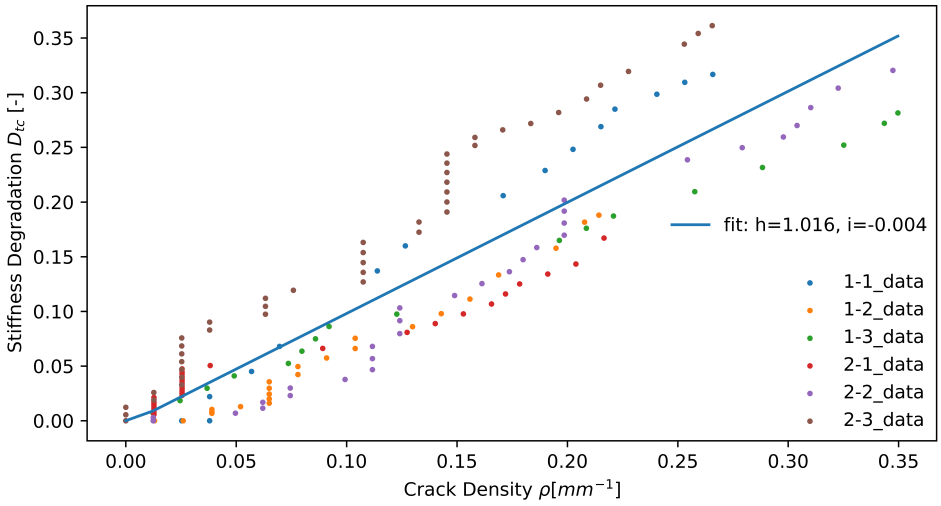

(a) Crack induced stiffness degradation model parameters: h and i

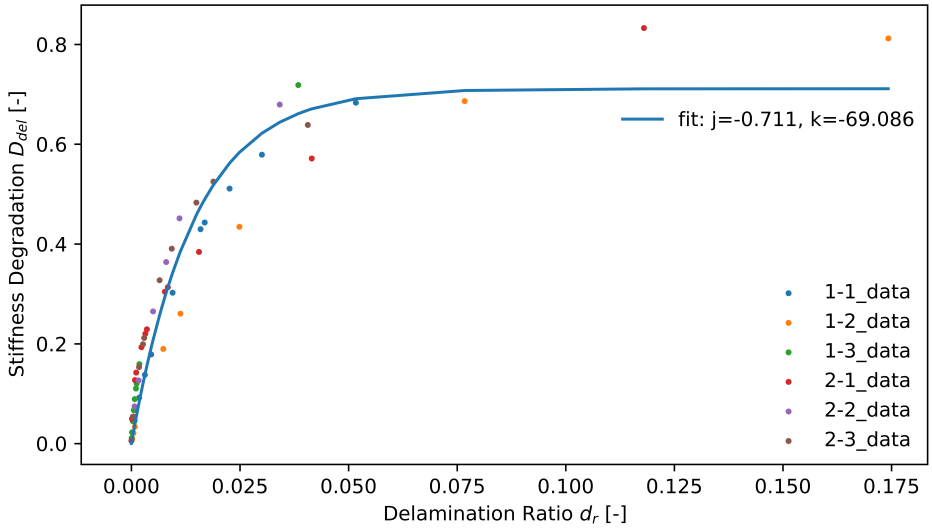

(b) Delamination induced stiffness degradation model parameters: j and k

Figure 5.3: Non-linear least squares fits of static stiffness degradation model parameters on full set of training specimens to serve as input for the machine learning model of specimen 1-4.

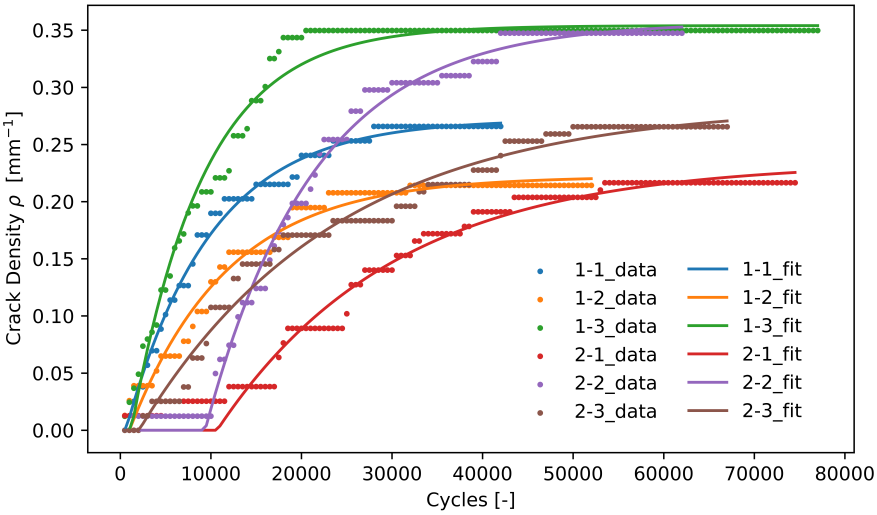

(a) Transverse matrix crack density growth model parameters: a, b and c

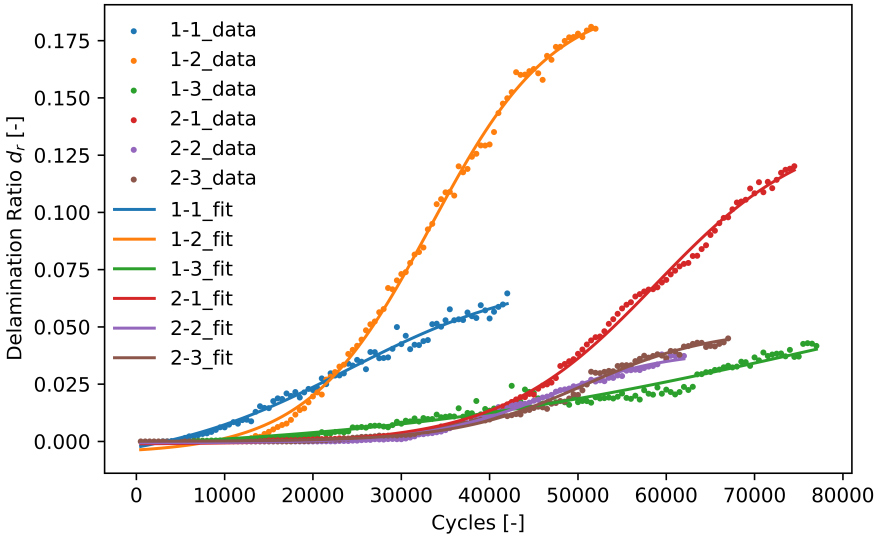

(b) Delamination ratio growth model parameters: d, e and f

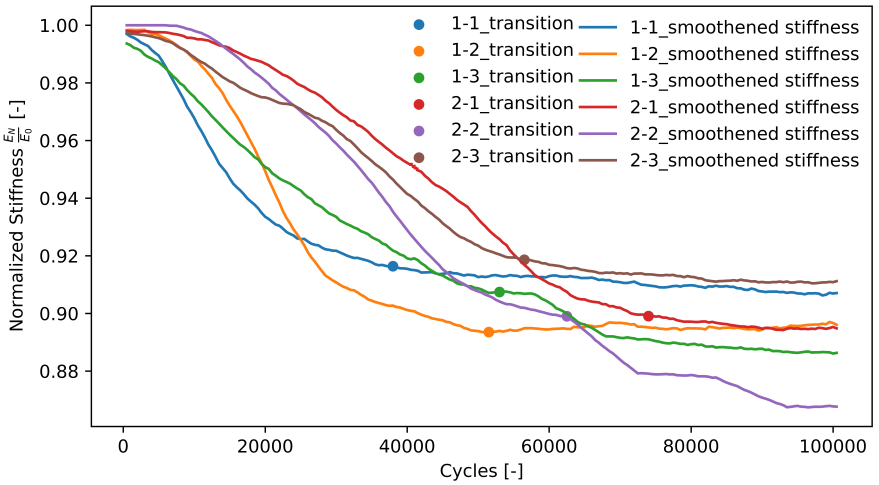

(c) Normalized stiffness model parameter: m

Figure 5.4: Non-linear least squares fits of adaptive model parameters for each training specimen serving as initialization for the machine learning model of specimen 1-4.

5.3.2 Filtering

Keeping in mind the pre-training and initialization results, the results for the subsequent filtering loop of the PF are presented here. In Figure 5.5, the results are displayed for the filtering process damage properties of specimen 1-4 with indicative weighted mean and 95% PI. One should note that no prognostics is involved yet, only damage properties contained in the particles at time step t_n are shown.

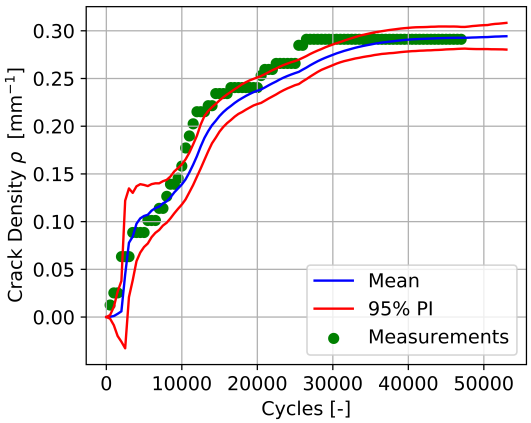

(a) Transverse matrix crack density ρ

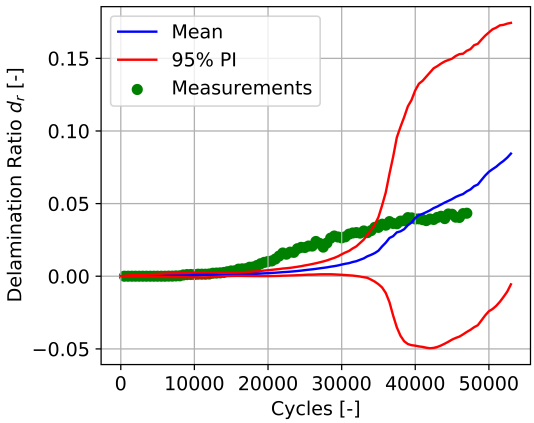

(b) Delamination ratio d_r

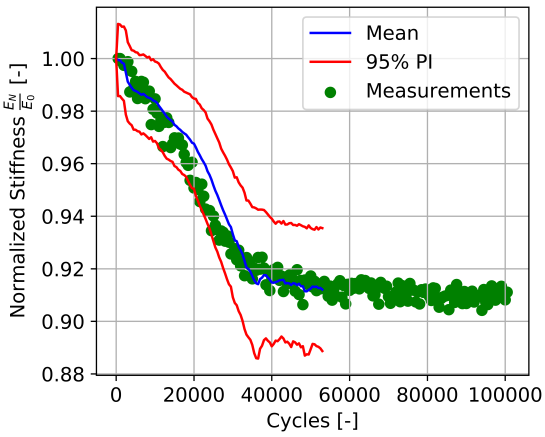

(c) Normalized stiffness $\frac{E_N}{E_0}$

Figure 5.5: Results of the filtering process for damage properties of specimen 1-4 with indicative weighted mean and 95% prediction interval (PI) of the N_s particles.

It is apparent in Figure 5.5a that the particles are a good representation of the crack density ρ at each filtering time step compared to the measurements (green). The delamination ratio d_r proves to be more difficult to be represented reliably in the filtering process as visible in Figure 5.5b. This is expected as the delamination ratio measurement is not used to update the particle filter model parameters. A likelihood estimate of these model parameters is only made via the normalized stiffness $\frac{E_N}{E_0}$ likelihood (which also depends on crack growth model parameters and model parameter m). While the run-out of delamination ratio higher than

0.05 does not cause problems as $D_{del}(d_r)$ reaches a plateau region for $d_r \geq 0.05$ (Figure 5.3b), the delay in delamination growth is a more difficult problem to deal with. This is elaborated upon later. For the normalized stiffness $\frac{E_N}{E_0}$ (Figure 5.5c), the delay in delamination growth is observed in a higher normalized stiffness between 20,000 and 35,000 cycles compared to the measurements. Apart from the delamination growth, this is also dependent on adaptive model parameter m, on which is elaborated later, used to map D_{tc} and D_{del} to $\frac{E_N}{E_0}$.

The model parameters are evolving from one time step to another in the PF by updating based on the likelihood function. First, the model parameters describing $\Delta\rho(N, \Delta N)$ are elaborated upon. Figure 5.6 displays the results of the updating process of the crack growth model parameters (a, b, c and $\sigma_{v,\rho}$) for specimen 1-4 with weighted mean and 95% PI. The green line indicates the 'actual' model parameter when performing NLS fitting on the testing specimen only for the relation $\rho(N)$.

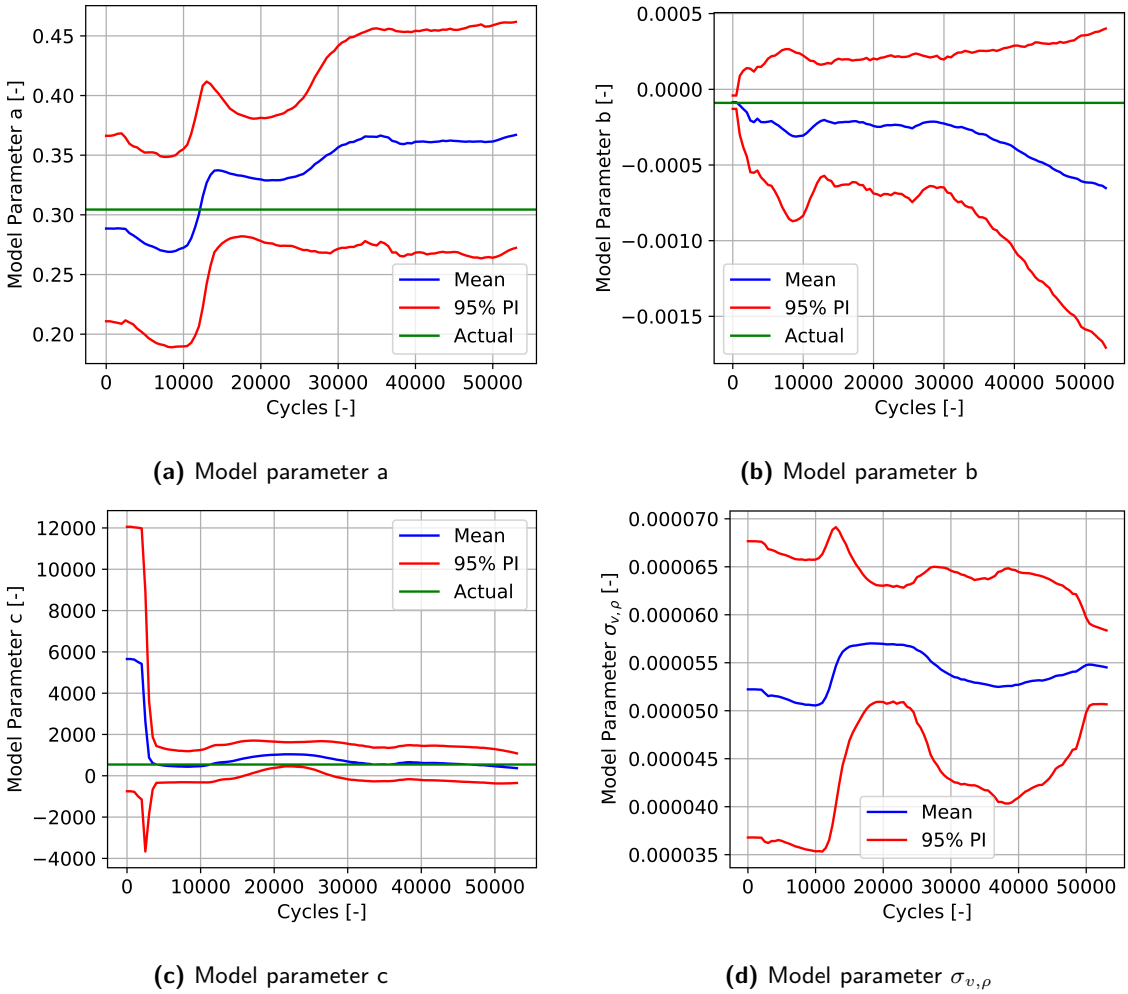

(a) Model parameter a

(b) Model parameter b

(c) Model parameter c

(d) Model parameter $\sigma_{v,\rho}$

Figure 5.6: Results of the updating process of transverse matrix crack growth model parameters for specimen 1-4 with indicative weighted mean and 95% prediction interval (PI) of the N_s particles.

The crack growth relation is the first showing characteristic behavior (steep increase of exponential function) compared to the delamination ratio. Therefore, very early in the lifetime

($\approx$ 20,000 cycles and less), both the likelihood of the crack density and normalized stiffness do not contain much information on delamination (nearly no growth for all particles), which means that particles are mostly judged on crack growth model parameters a, b and c to assign the importance weights. This is reflected in model parameter c (Figure 5.6c), which quickly converges to its actual value. This parameter indicates when exponential behavior starts in $\rho(N)$, which is usually below 10,000 cycles. This means characteristic behavior happens early in the lifetime. The model parameter b (Figure 5.6b) becomes remarkably smaller in early life. This parameter describes the steepness of the exponential curve. The other model parameters a (Figure 5.6a) and $\sigma_{v,\rho}$ (Figure 5.6d) show nearly constant behavior, which is expected as specimen 1-4 shows standard crack growth compared to the training set.

Secondly, the model parameters describing $\Delta d_r(N, \Delta N)$ are elaborated upon. Figure 5.7 displays the results of the updating process of the delamination model parameters (d, e, f and σ_{v,d_r}) for specimen 1-4 with weighted mean and 95% PI. The green line indicates the 'actual' model parameter from NLS fitting on the testing specimen only for the relation $d_r(N)$.

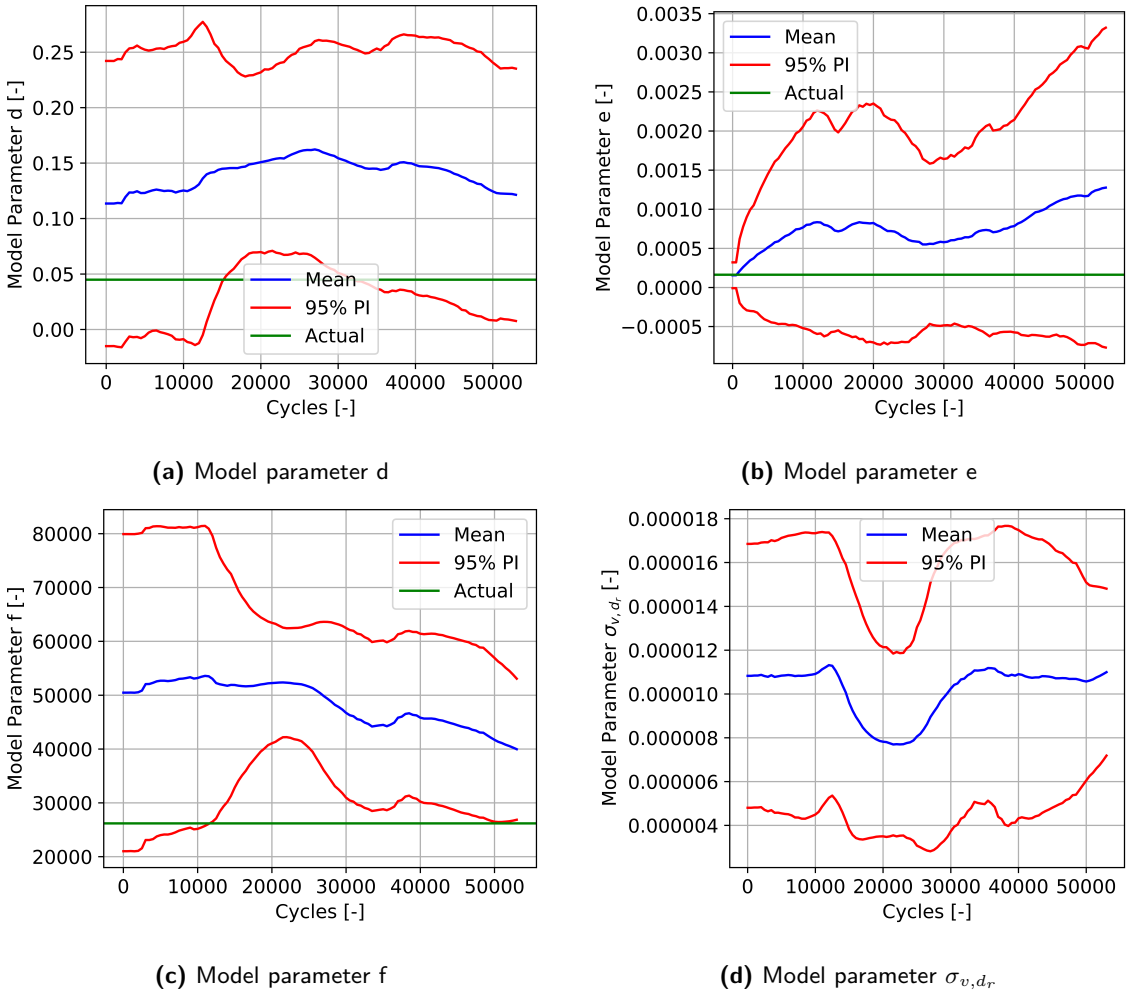

(a) Model parameter d

(b) Model parameter e

(c) Model parameter f

(d) Model parameter σ_{v,d_r}

Figure 5.7: Results of the PF updating process of delamination ratio growth model parameters for specimen 1-4 with indicative weighted mean and 95% prediction interval (PI) of the N_s particles.

The delamination growth relation shows only very late characteristic behavior (upward kink in the logistic function) compared to the crack density. As explained previously, this means that during early lifetime ($\approx$ 20,000 cycles and less), little information can be obtained on the delamination model parameters because the delamination growth for nearly each set of model parameters is close to zero at that time. Therefore, the available model parameters for the delamination growth are those associated to particles that have been assigned high importance weights based on the crack growth. However, after early lifetime, the characteristic curvature starts (Figure 5.10c). The number of cycles at which this occurs is reflected in model parameter f (Figure 5.7c). This parameter indicates where the kink is present in $d_r(n)$, or equivalently were $\Delta d_r(N, \Delta N)$ is maximal. The model parameter e (Figure 5.7b) becomes remarkably larger in early life. Given the lack of decrease in model parameter f over the lifetime, it is consistent that model parameter e compensates for this by increasing the steepness in $d_r(n)$ to quickly obtain higher d_r for a given model parameter f. The other model parameters d (Figure 5.7a) and σ_{v,d_r} (Figure 5.7d) show nearly constant behavior, which is expected as specimen 1-4 shows standard delamination growth compared to the training set. While the model parameter d remains too high, it is found in this thesis that the upper logistic curve matters less to determine the RUL due to the asymptotic behavior in $D_{del}(d_r)$ (Figure 5.3b). Keeping in mind that the delamination ratio measurement is not used to update the model parameters (only the stiffness measurement is indirectly used), this indicates why model parameter f converges in neither of the specimens (even for strong performing specimens as specimen 1-4) because an excessive value for d_r does not necessarily relate to an excessively low $\frac{E_N}{E_0}$ given the aforementioned asymptote in D_{del}.

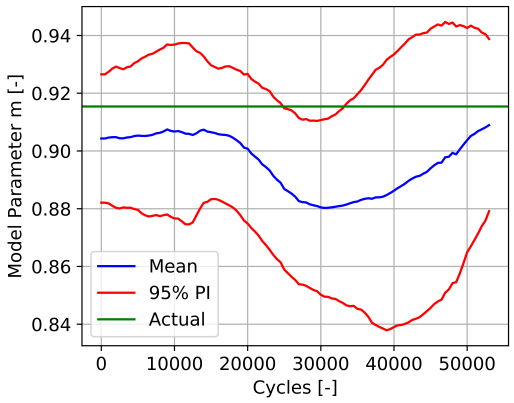

Figure 5.8: Results of the updating of the normalized stiffness adaptive model parameter m for specimen 1-4 with indicative weighted mean and 95% prediction interval (PI) of the N_s particles.

Lastly, the model parameter m, describing $\frac{E_N}{E_0}(D_{tc}, D_{del})$, is elaborated upon. For that purpose, Figure 5.8 displays the results of the updating process of the normalized stiffness model parameter m for specimen 1-4 with weighted mean and 95% PI. The green line indicates the 'actual' model parameter by applying the 0.001 stiffness degradation over 2500 cycles threshold to the smooth normalized stiffness curve of specimen 1-4 only. It is important to note that the model parameter m has a significant influence on the stiffness predictions. In this case variation in m is limited, but for specimen 2-2, the negative influence of model parameter m on the predictions is more expressive and explained in more detail.

5.3.3 Prognostics

As the flowchart Figure 4.1 indicates, the aforementioned filtering step is followed by the prognostics sub-algorithm, for which the results are elaborated upon here with the RUP of specimen 1-4. One should keep in mind that the results for the model parameters (Figure 5.6 to 5.8) at time step t_n serve as direct input to explore future damage states of the damage property at time step t_n (Figure 5.5). While the figures with results for the filtering step contain a mean, it is important to keep in mind that the prognostics are performed for each of the N_s particles separately. Once the normalized stiffness degrades less than 0.001 over 2,500 cycles for a single particle, its failure boolean at time step t_{n+l} in the vector $\boldsymbol{F}$ becomes True. This means the RUL of that particle is $t_{n+l} - t_n$. The RUL to EOEFL results of specimen 1-4 have been presented previously in Figure 5.1d.

At filtering time step t_n (a) 500, (b) 10,000, (c) 20,000, (d) 30,000, (e) 40,000 and (f) 45,000 cycles, the results for the prognostics of the transverse matrix crack density ρ (Figure 5.9), delamination ratio d_r (Figure 5.10) and normalized stiffness $\frac{E_N}{E_0}$ (Figure 5.11) are shown. For this purpose, the weighted mean and 95% PI of the N_s particles are displayed at each prognostics time step t_{n+l}. The green data points up to t_n are the measurements that have been used previously in the PF algorithm to update model parameters.

It is observed that the prognostics for the crack density perform particularly well. From 20,000 cycles on (Figure 5.9c), the PF quickly identifies the plateau region just below $\rho = 0.3$ mm^{-1}. Additionally, the confidence intervals decrease when t_n increases. This is partially caused by the decreasing spread of the model parameters, which was dealt with in the filtering step, but also because the zero-mean normally distributed prediction method error is added at every time step. Compared to the crack density, the PF algorithm manages to reliably predict the delamination ratio from 30,000 cycles on (Figure 5.10d), which is slightly later. As explained in the filtering step, this is partially caused by later characteristic damage behavior for the delamination ratio, with in this case d_r different from zero only after $t_n = 15,000$ cycles. Additionally, as this measurement is not used, a likelihood cannot be assigned to a particle based on d_r. This is a second reason for the delay in the increase of d_r. However, it is identified that this discrepancy between the measured and predicted d_r is smaller than for specimen 2-2, for which the most important reason is a smaller variation in model parameter m. The influence of this model parameter on the prognostics is treated in more detail in section 5.4. Finally, one should note that with the asymptote in the current $D_{del}(d_r)$ relation, the upper plateau of $d_r(N)$ cannot be reliably predicted. This is also visible in Figure 5.10f.

Using the two aforementioned damage properties at t_{n+l} (ρ and d_r), the static model parameters (h, i, j and k), and the model parameter m, the prognostics of the normalized stiffness is obtained. The stiffness degradation serves as direct input to the EOEFL failure criterion. In Figure 5.12, histograms at the same time steps t_n present the distribution of the RUL predictions of all particles. These histograms with the distribution of particles directly relate to the indicated mean and PI in Figure 5.1d. At $t_n = 45,000$ cycles (Figure 5.12f), one can see that many particles have failed already (large peak at $RUL \approx 0$). This indicates the difficulty of using this degradation rate failure criterion, for which the failed vector $\boldsymbol{F}$ is passed from filtering to prognostics loop at each t_n. This can cause ambiguity as a failed particle's model parameters could evolve, but the RUL is immediately zero with the failed condition.

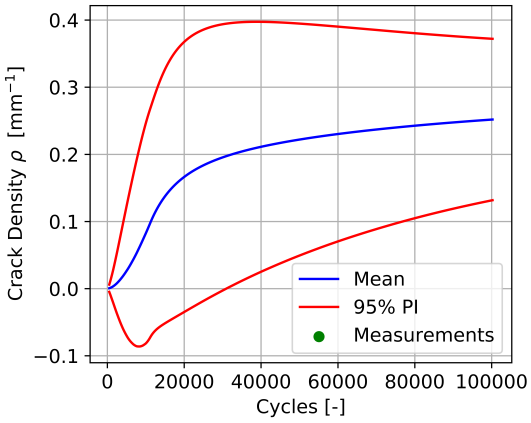

(a) 500 cycles

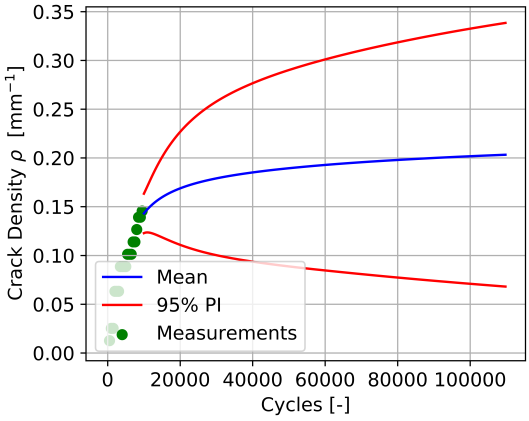

(b) 10,000 cycles

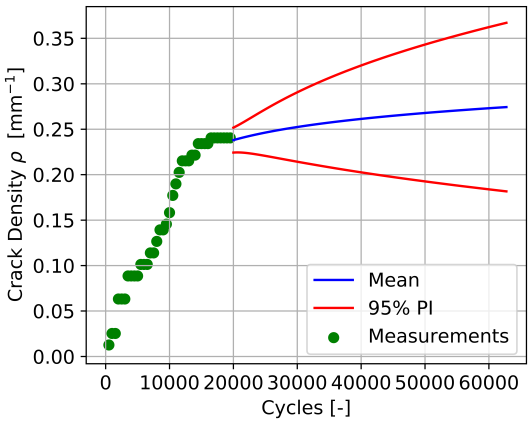

(c) 20,000 cycles

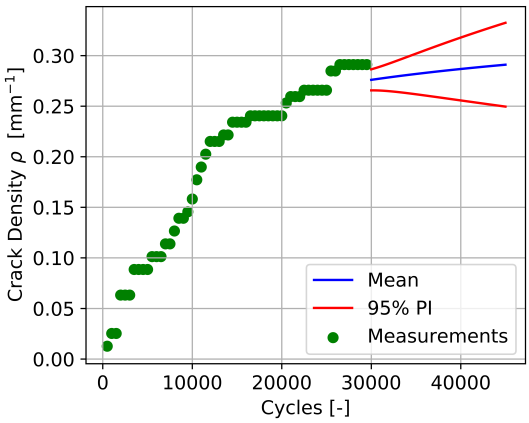

(d) 30,000 cycles

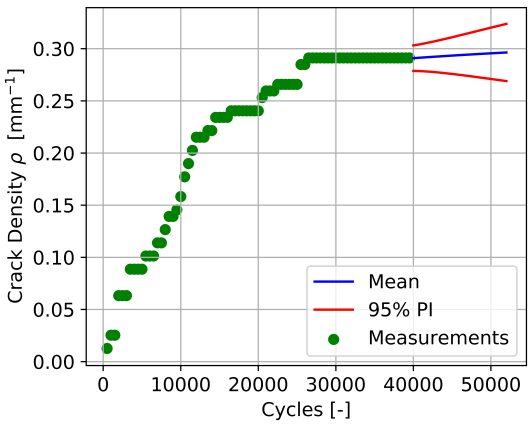

(e) 40,000 cycles

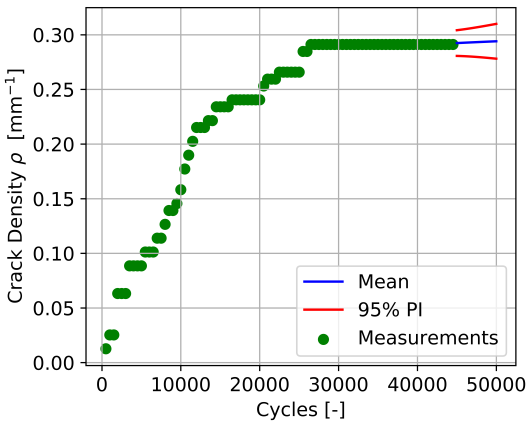

(f) 45,000 cycles

Figure 5.9: Results of the prognostics at distinct cycles of the transverse matrix crack density ρ for specimen 1-4 with indicative weighted mean and 95% prediction interval (PI) of the N_s particles.

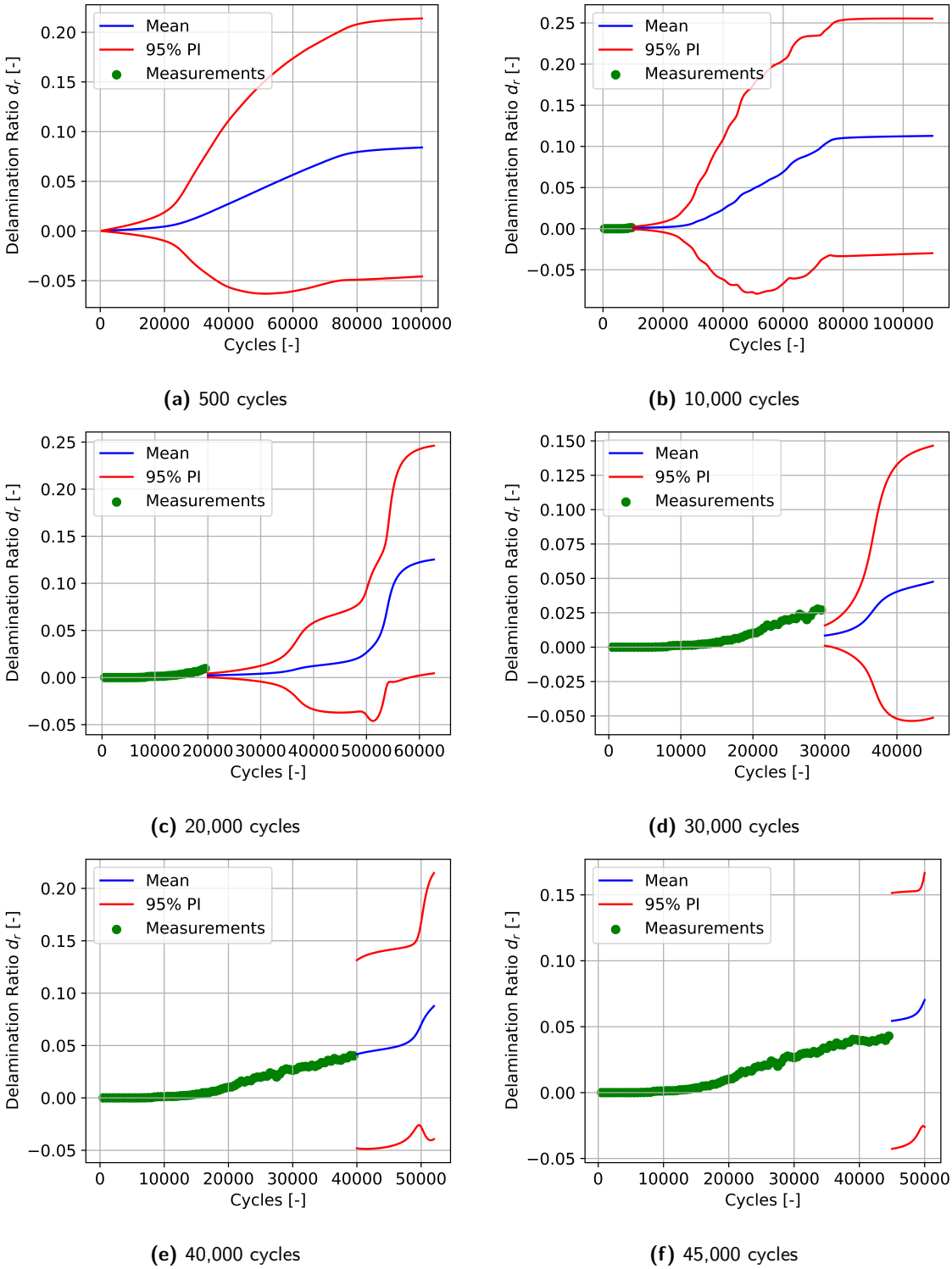

(a) 500 cycles

(b) 10,000 cycles

(c) 20,000 cycles

(d) 30,000 cycles

(e) 40,000 cycles

(f) 45,000 cycles

Figure 5.10: Results of the prognostics at distinct cycles of the delamination ratio d_r for specimen 1-4 with indicative weighted mean and 95% prediction interval (PI) of the N_s particles.

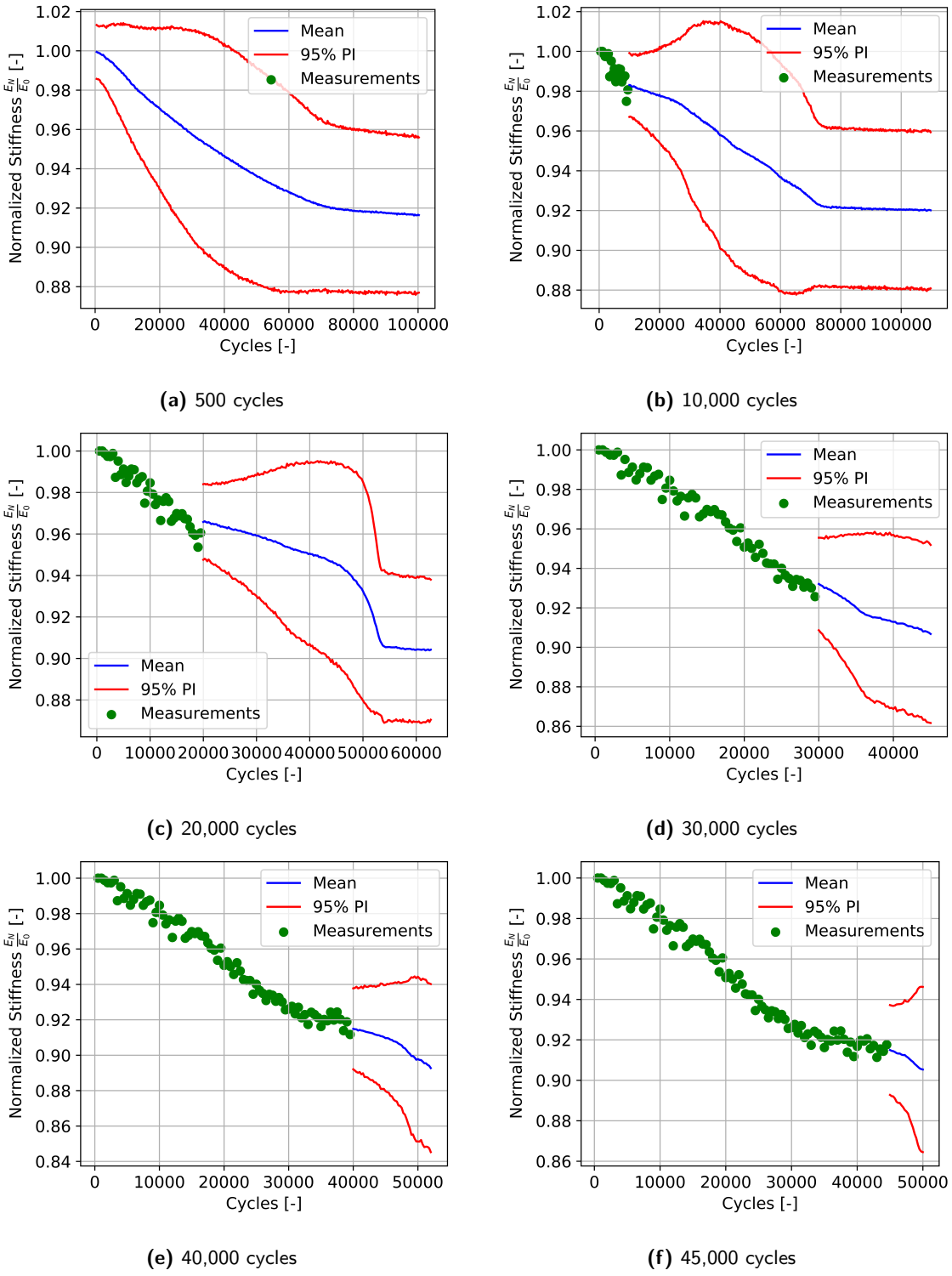

(a) 500 cycles

(b) 10,000 cycles

(c) 20,000 cycles

(d) 30,000 cycles

(e) 40,000 cycles

(f) 45,000 cycles

Figure 5.11: Results of the prognostics at distinct cycles of the normalized stiffness $\frac{E_N}{E_0}$ for specimen 1-4 with indicative weighted mean and 95% prediction interval (PI) of the N_s particles.

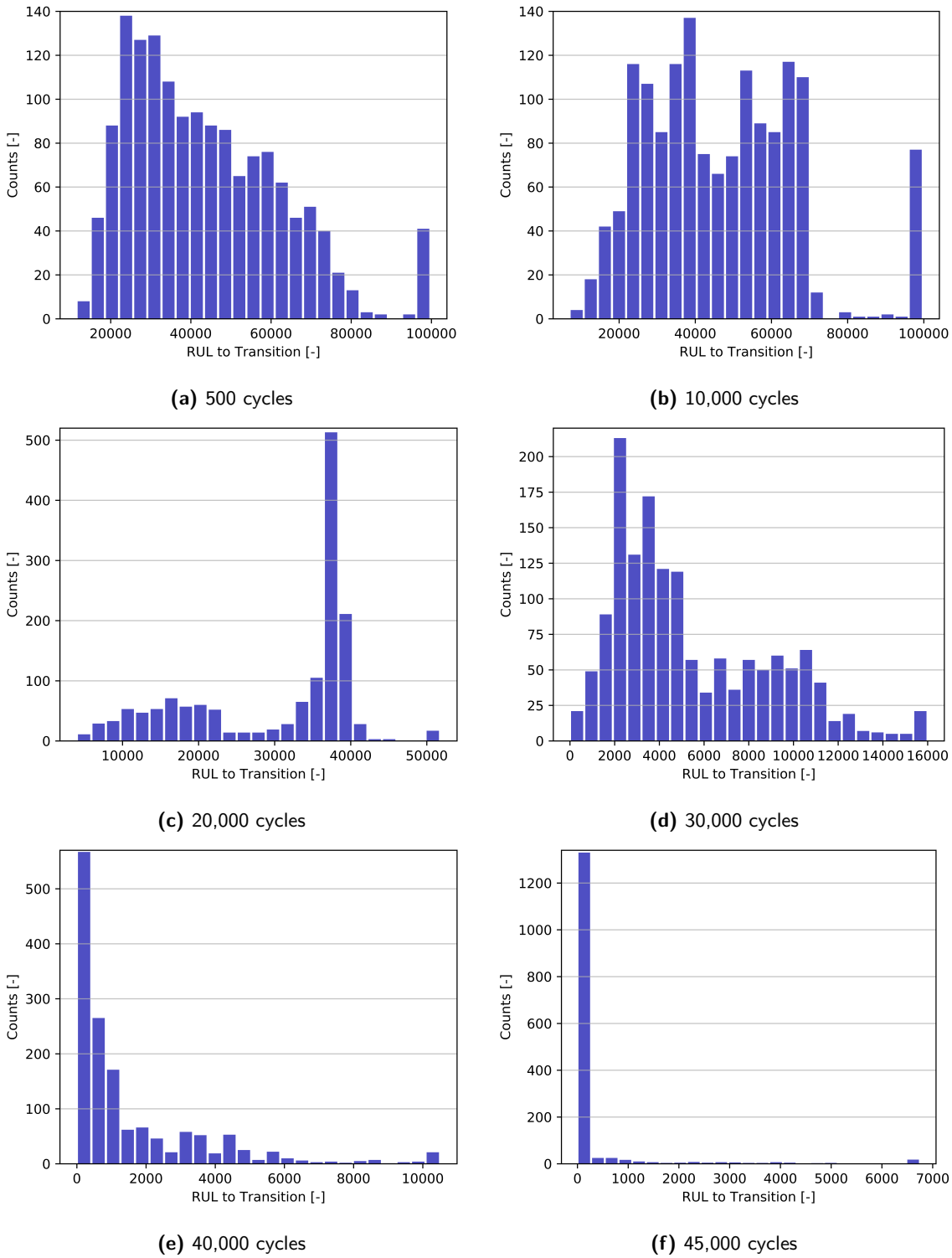

(a) 500 cycles

(b) 10,000 cycles

(c) 20,000 cycles

(d) 30,000 cycles

(e) 40,000 cycles

(f) 45,000 cycles

Figure 5.12: Results of the prognostics at distinct cycles of the remaining useful life (RUL) for stage I to II transition for specimen 1-4 with a histogram presenting the distribution of the N_s particles.

5.4 Extensive Results of Specimen 2-2

In this section, the results of specimen 2-2 are presented in extensive detail. This specimen is a particularly weak performer of the PF as mentioned in section 5.2. The results of RUL prognostics for stage I to II transition with indicative weighted mean and 95% PI of the N_s particles has been presented in Figure 5.2b. The results for each of the PF steps is discussed in the following subsections in a similar way as was done for specimen 1-4 previously. Additionally, remarkable differences with the good performing specimen 1-4 are highlighted.

5.4.1 Pre-Training

In the pre-training step, the training specimens, being the set of all specimens except for the testing specimen, are used to serve as input for the initialization of particles in the PF algorithm. A flowchart of this step has been shown in Figure 4.2. A distinction is once more made between static and adaptive model parameters.

Static Model Parameters

First, the focus is on the static model parameters h, i, j and k. These are pre-trained using NLS on the combined dataset of the training specimens all together to obtain a single value for each. The results of the NLS fits are shown in Figure 5.13. Because the entire set of training specimens is used in the NLS fits, and because the training set consists of all specimens except for the testing specimen, the result of this process is different for specimen 2-2 compared to specimen 1-4. This is mostly observable when comparing Figure 5.3b (pre-training $D_{del}(d_r)$ for specimen 1-4) with Figure 5.13b (pre-training $D_{del}(d_r)$ for specimen 2-2). The higher value for the model parameter j in specimen 1-4, which is associated with a higher D_{del} plateau region, is present because specimen 2-2 is used in the pre-training process of specimen 1-4. The data points for specimen 2-2 are associated with a higher plateau region when compared to those for specimen 1-4.

The crack induced stiffness degradation model parameters (Figure 5.13a) are $h = 1.095$ and $i = -0.002$. Following the methodology, a single uncertainty is obtained as standard deviation of the 0-mean normal distribution $\sigma_{v,D_{tc}} = 0.0426$. Similarly, the delamination induced stiffness degradation model parameters (Figure 5.13b) are $j = -0.725$ and $k = -60.873$ and the uncertainty is again obtained as the standard deviation $\sigma_{v,D_{del}} = 0.0537$.

Adaptive Model Parameters

After the static model parameters, the focus moves to the adaptive model parameters a, b, c, d, e, f and m. As the adaptive model parameters are pre-trained using NLS on each training specimen separately, little differences are present compared to specimen 1-4. The only remarkable difference is that specimen 1-4 is now in the training set, while specimen 2-2 is the testing specimen and thus not in the training set. As a result, the NLS fits and state transition model parameter m for pre-training of specimen 2-2 are shown in Figure 5.14. The corresponding model parameters and prediction method errors (standard deviation of 0-mean

normally distributed error) for each specimen that will be used for initialization are listed in Table 5.5 and 5.6 respectively.

Table 5.5: NLS Fits of Adaptive Model Parameters per Training Specimen (Pre-Training 2-2)

	Crack Growth			Delamination Growth			Stiffness
Spec.	a	b	c	d	e	f	m
1-1	0.272	-0.106E-3	610	0.084	0.932E-4	23,929	0.916
1-2	0.222	-0.924E-4	1,011	0.198	0.144E-3	33,323	0.894
1-3	0.354	-0.125E-3	1,213	0.092	0.377E-4	77,001	0.907
1-4	0.304	-0.900E-4	545	0.045	0.163E-3	26,185	0.915
2-1	0.235	-0.509E-4	10,689	0.140	0.114E-3	58,826	0.899
2-3	0.285	-0.463E-4	2,067	0.049	0.137E-3	50,754	0.919

Table 5.6: NLS Adaptive Model Parameter Errors per Training Specimen (Pre-Training 2-2)

	Crack Growth		Delamination Growth	
Spec.	$\sigma_{v,\rho,total}$	$\sigma_{v,\rho}$	$\sigma_{v,d_r,total}$	σ_{v,d_r}
1-1	7.01E-3	3.97E-5	2.15E-3	1.22E-5
1-2	8.79E-3	4.98E-5	2.87E-3	1.63E-5
1-3	1.16E-2	6.59E-5	2.32E-3	1.31E-5
1-4	1.05E-2	5.95E-5	1.11E-3	6.28E-6
2-1	1.12E-2	6.32E-5	1.89E-3	1.07E-5
2-3	1.13E-2	6.41E-5	1.19E-3	6.76E-6

The same reasoning as for specimen 1-4 is valid in the initialization step, which means that all parameters and prediction method errors are initialized to a uniform distribution. This is because the size of the training set is small with six specimens. Therefore, only the minima and maxima of the initialization can differ, but the underlying distribution cannot change.

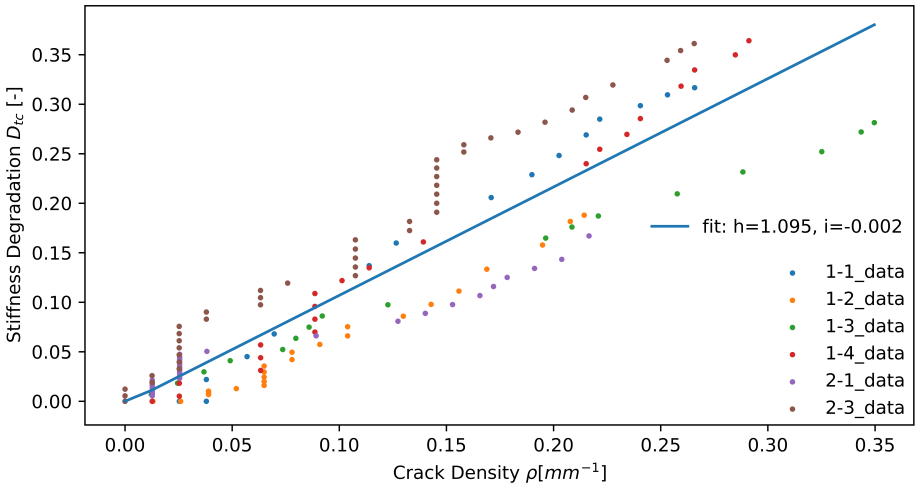

(a) Crack induced stiffness degradation model parameters: h and i

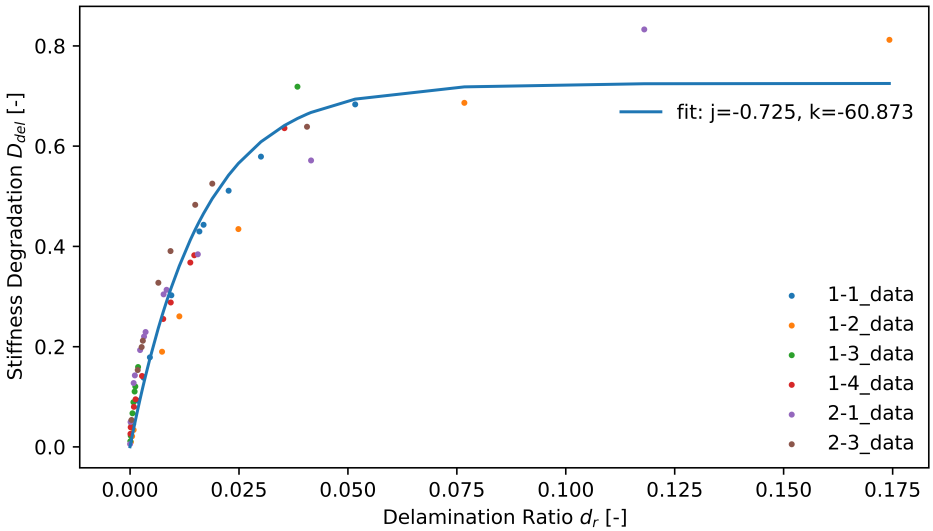

(b) Delamination induced stiffness degradation model parameters: j and k

Figure 5.13: Non-linear least squares fits of static stiffness degradation model parameters on full set of training specimens to serve as input for the machine learning model of specimen 2-2.

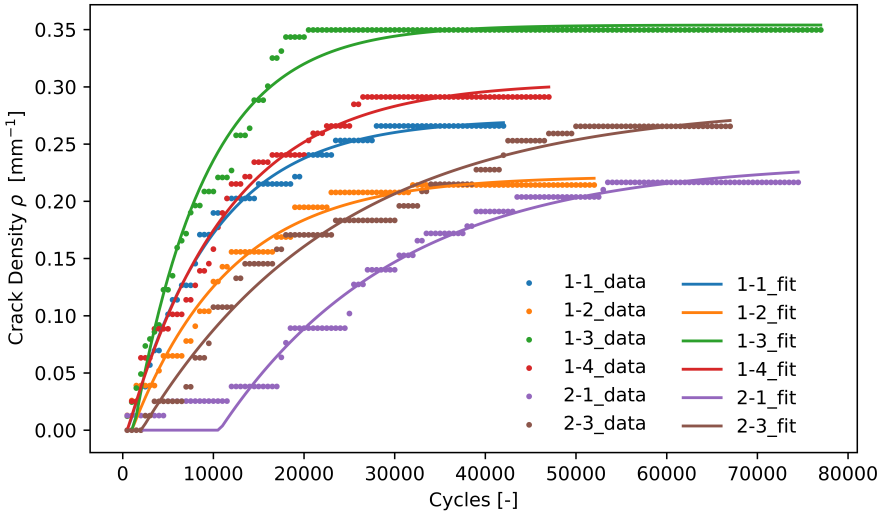

(a) Transverse matrix crack density growth model parameters: a, b and c

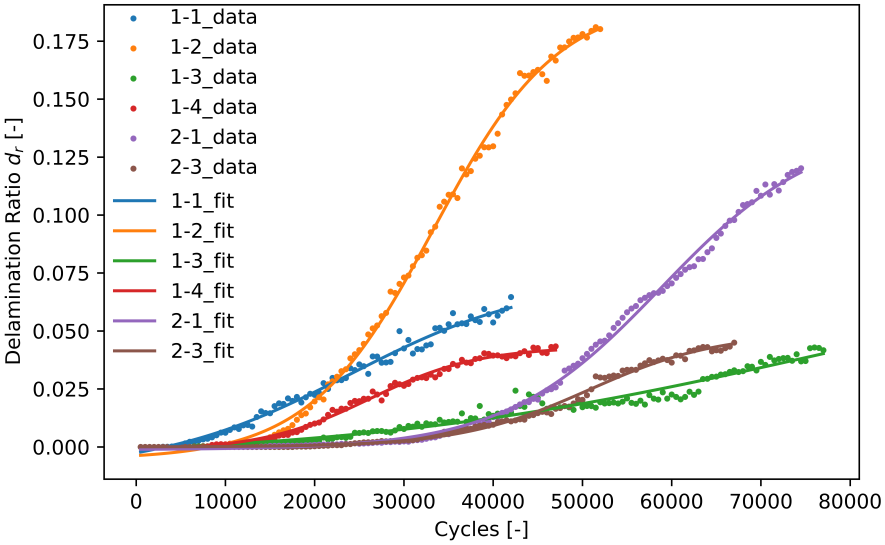

(b) Delamination ratio growth model parameters: d, e and f

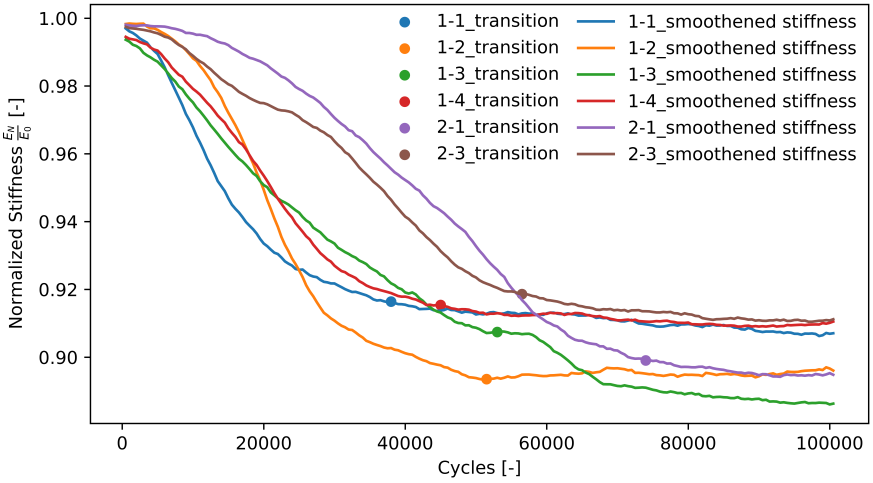

(c) Normalized stiffness model parameter: m

Figure 5.14: Non-linear least squares fits of adaptive model parameters for each training specimen serving as initialization for the machine learning model of specimen 2-2.

5.4.2 Filtering

The filtering results of the PF algorithm for specimen 2-2 are presented here. In Figure 5.15, the results are displayed for the filtering process damage properties of specimen 2-2 with indicative weighted mean and 95% PI. One should note that no prognostics is involved yet, only damage properties contained in the particles at time step t_n are shown.

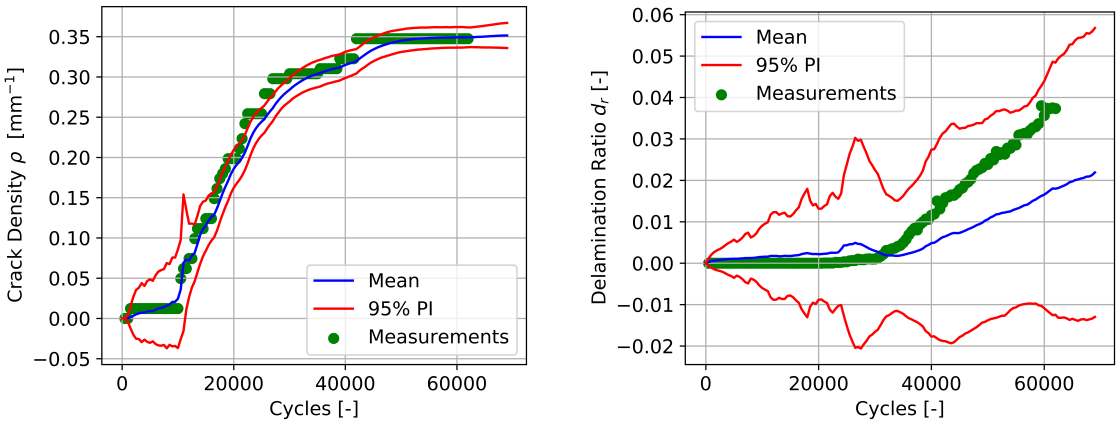

(a) Transverse matrix crack density ρ **(b)** Delamination ratio d_r

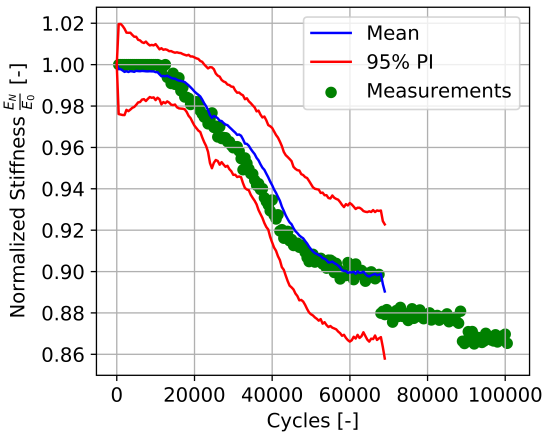

(c) Normalized stiffness $\frac{E_N}{E_0}$

Figure 5.15: Results of the filtering process for damage properties of specimen 2-2 with indicative weighted mean and 95% prediction interval (PI) of the N_s particles.

One can observe in Figure 5.15a that the particles are a good representation of the crack density ρ at each filtering time step compared to the measurements (green). This includes the offset of the exponential relation that makes the crack density up to 10,000 cycles equal to zero. The delamination ratio d_r proves again more difficult to reliably represent in the filtering process of specimen 2-2 as displayed in Figure 5.15b. It is important to mention that no in-situ (online) delamination measurements are used in the methodology, making it harder to update those model parameters in the filter. The only evidence used to weigh the importance of particles for d_r is the normalized stiffness measurement $\frac{E_N}{E_0}$. However, this

measurement depends also on the crack growth and model parameter m. The delamination ratio contained in the particles of the PF are persistently lower than (offline) measurements added for comparative purposes here. The normalized stiffness $\frac{E_N}{E_0}$ (Figure 5.15c) is highly dependent on adaptive model parameter m, on which is elaborated later, used to map D_{tc} and D_{del} to $\frac{E_N}{E_0}$.

The model parameters are evolving from one time step to another in the PF by updating based on the likelihood function. First, the model parameters describing $\Delta\rho(N, \Delta N)$ are elaborated upon. Figure 5.16 displays the results of the updating process of the crack growth model parameters (a, b, c and $\sigma_{v,\rho}$) for specimen 2-2 with weighted mean and 95% PI. The green line indicates the 'actual' model parameter when performing NLS fitting on the testing specimen only for the relation $\rho(N)$.

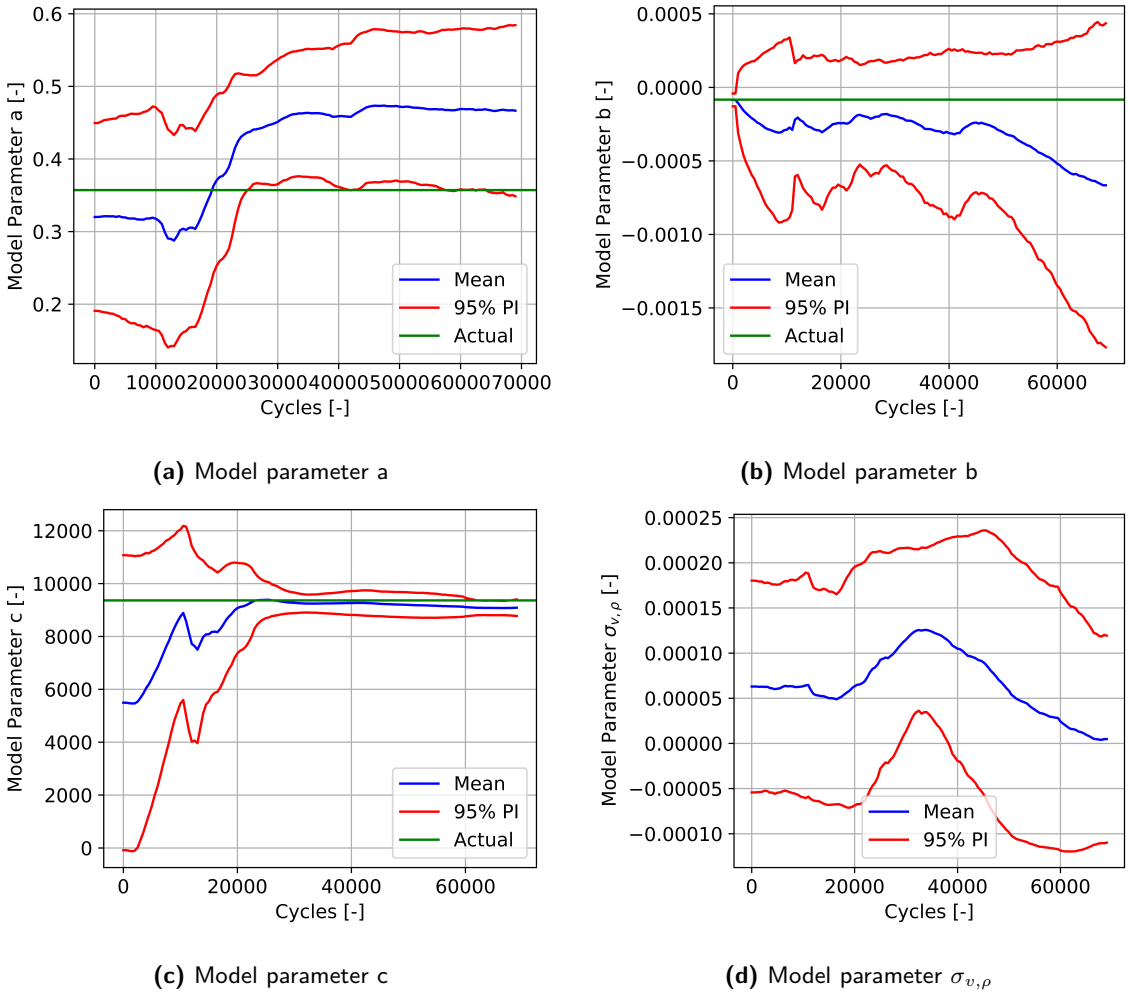

(a) Model parameter a

(b) Model parameter b

(c) Model parameter c

(d) Model parameter $\sigma_{v,\rho}$

Figure 5.16: Results of the updating process of transverse matrix crack growth model parameters for specimen 2-2 with indicative weighted mean and 95% prediction interval (PI) of the N_s particles.

Although the crack density shows a characteristic exponential behavior later in specimen 2-2 than in specimen 1-4 due to the offset, it is still the first damage property to show characteristic behavior (steep increase of exponential function) compared to the delamination

ratio. Therefore, very early in the lifetime ($\approx$ 25,000 cycles and less), both the likelihood of the crack density and normalized stiffness do not contain much information on delamination (nearly no growth for all particles). This means that particles are mostly judged on crack growth model parameters a, b and c to assign the importance weights. This is reflected in model parameter c (Figure 5.16c), which quickly converges to its actual value as was the case for specimen 1-4 as well. This parameter indicates the offset for when exponential behavior starts in $\rho(N)$. The model parameter b (Figure 5.16b) gradually decreases in early life. It is used to describe the steepness of the exponential curve. The other model parameters $\sigma_{v,\rho}$ (Figure 5.16d) shows nearly constant behavior. The value of model parameter a (Figure 5.16a) indicates the asymptote in the $\rho(N)$ relation. The fact that model parameter a does not converge to the actual value can be explained by keeping in mind the difference between the actual relation and the growth function. When the filter increases model parameter a, it does not necessarily mean the plateau should be higher, but it rather looks at the growth in crack density that is required to obtain a likely crack density matching the upcoming measurement.

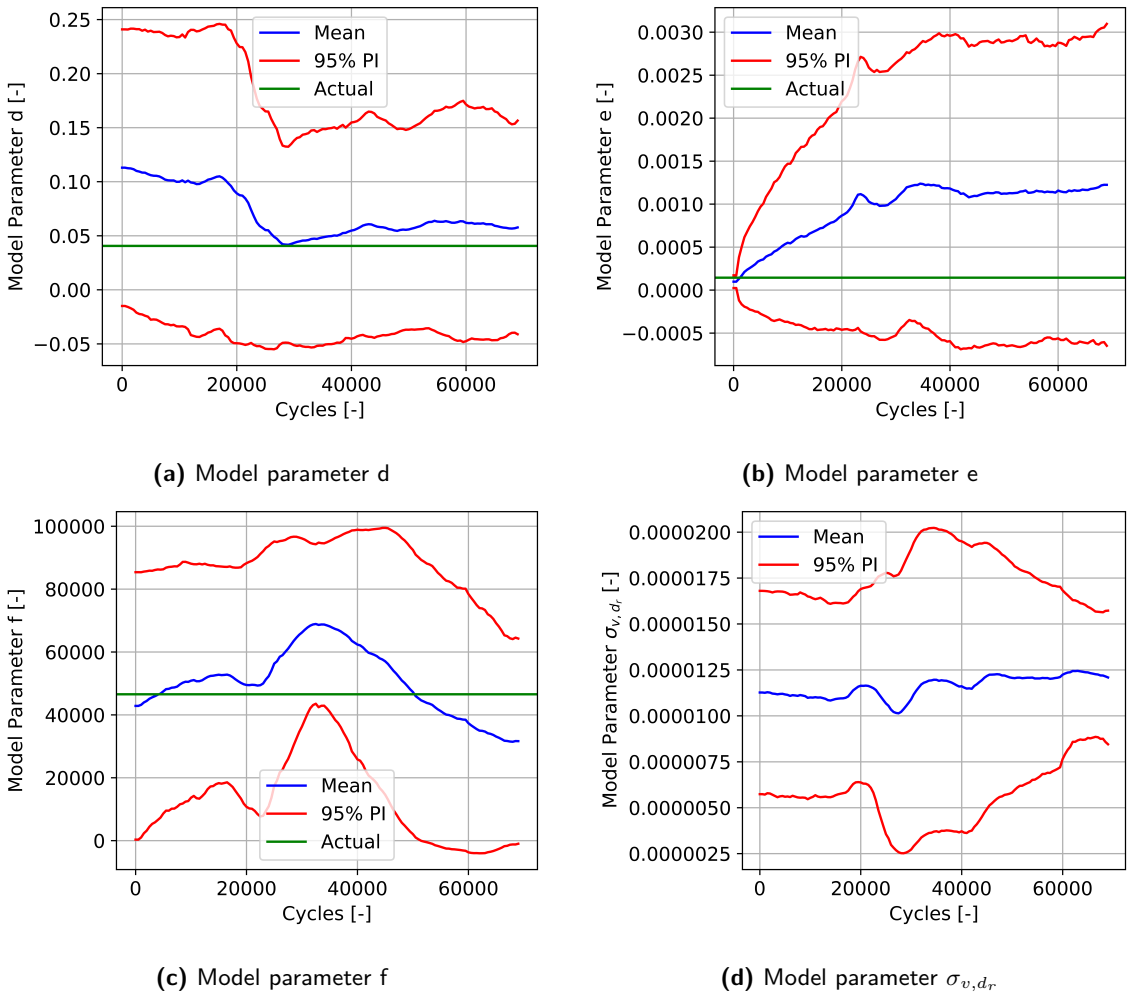

(a) Model parameter d

(b) Model parameter e

(c) Model parameter f

(d) Model parameter σ_{v,d_r}

Figure 5.17: Results of the updating process of delamination ratio growth model parameters for specimen 2-2 with indicative weighted mean and 95% prediction interval (PI) of the N_s particles.

Secondly, the model parameters describing $\Delta d_r(N, \Delta N)$ are elaborated upon. Figure 5.17 displays the results of the updating process of the delamination model parameters (d, e, f and σ_{v,d_r}) for specimen 2-2 with weighted mean and 95% PI. The green line indicates the 'actual' model parameter from NLS fitting on the testing specimen only for the relation $d_r(N)$.

The delamination growth relation once more shows very late characteristic behavior (upward curve of the logistic function) compared to the crack density. As explained previously, this means that during early lifetime ($\approx$ 30,000 cycles and less), little information is obtained on the delamination model parameters because the delamination growth for nearly each set of model parameters is close to zero at that time. Therefore, the available model parameters for the delamination growth are those associated to particles that have been assigned high importance weights based on the crack growth. However, after early lifetime, the characteristic curvature starts. The number of cycles at which this occurs is reflected in model parameter f (Figure 5.17c). Before characteristic behavior up to 30,000 cycles, it is visible that model parameter f has increased. However, once delamination information is reflected in the stiffness measurement, the delamination growth should increase with decreasing crack growth (thus crack induced stiffness loss). This explains the decrease in model parameter f after 30,000 cycles. More specifically, model parameter f indicates where the kink is present in $d_r(n)$, or equivalently were $\Delta d_r(N, \Delta N)$ is maximal. The model parameter e (Figure 5.7b) becomes remarkably larger in early life. However, most of the increase happens at the time little information exists on $d_r(n)$ from measurements, thus it is most probable that such model parameter e belonged to a particle with likely crack density in early life. The other model parameters d (Figure 5.7a) and σ_{v,d_r} (Figure 5.7d) show converging behavior to the actual value and nearly constant behavior respectively.

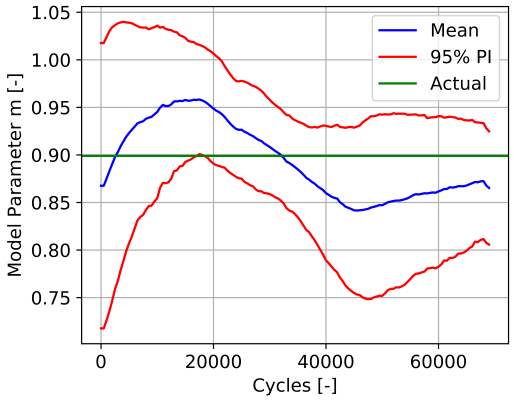

Figure 5.18: Results of the updating process of the normalized stiffness adaptive model parameter m for specimen 2-2 with indicative weighted mean and 95% prediction interval (PI) of the N_s particles.

Lastly, the model parameter m, describing $\frac{E_N}{E_0}(D_{tc}, D_{del})$, is elaborated upon in extensive detail. As previously mentioned in the results of specimen 1-4 because its influence is clearly visible here. For that purpose, Figure 5.18 displays the results of the updating process of the normalized stiffness model parameter m for specimen 2-2 with weighted mean and 95% PI. The green line indicates the 'actual' model parameter by applying the 0.001 stiffness degradation over 2500 cycles threshold to the smooth normalized stiffness curve of specimen 2-2 only.

It is apparent that model parameter m has a significant influences as it controls the combined normalized stiffness based on both crack density and delamination ratio. A lower value of m quickly decreases the normalized stiffness. For specimen 1-4, the range over which parameter m changes is smaller (≈ 0.03) compared to specimen 2-2 (≈ 0.1). It is observed that when the delamination ratio is larger than expected, it is compensated by the parameter m to 'match' the incoming stiffness measurement in the filtering process. This is clearly visible when comparing Figure 5.15b with Figure 5.18. Below 30,000 cycles, the delamination ratio is higher than the actual offline measured delamination ratio (not used in the updating step). This causes the model parameter m to be larger below these 30,000 cycles in order to increase the normalized stiffness to match the online in-situ stiffness measurement. After this point, model parameter m decreases even below the actual value because d_r is underestimated. In that case, model parameter m compensates the lower d_r by decreasing model parameter m to artificially increase the normalized stiffness. This indicates the difficulty of using the normalized stiffness combination model with the crack density and delamination ratio in the PF without using a measured in-situ delamination in the online process.

5.4.3 Prognostics

In a similar way as for the strong performer, specimen 1-4, the results for the RUP prognostics of specimen 2-2 are treated here in extensive detail. This goes hand in hand with identifying the most prominent differences between the two in performance. As the flowchart Figure 4.1 indicates, the aforementioned filtering step if followed by the prognostics sub-algorithm. The results for the model parameters of specimen 2-2 that have been shown in (Figure 5.16 to 5.18) serve as direct input to explore future damage states of the damage property at time step t_n (Figure 5.15). It is important to note that prognostics are performed separately for each particle. The RUL to EOEFL results of specimen 2-2 have been presented previously in Figure 5.2b.

At filtering time step t_n (a) 500, (b) 10,000, (c) 20,000, (d) 30,000, (e) 42,500 and (f) 55,000 cycles, the results for the prognostics of the transverse matrix crack density ρ (Figure 5.19), delamination ratio d_r (Figure 5.20) and normalized stiffness $\frac{E_N}{E_0}$ (Figure 5.21) are shown. For this purpose, the weighted mean and 95% PI of the N_s particles are displayed at each prognostics time step t_{n+l}. The green data points up to t_n are the measurements that have been used previously in the PF algorithm to update model parameters.

The results for the crack density prognostics show reliable results, even with the offset, for which the crack density remains zero first. At $t_n = 10{,}000$ cycles (Figure 5.19b), the exonential behavior of the for the crack density is modeled well in the prognostics. From 30,000 cycles on (Figure 5.9c), the PF successfully identifies the plateau region just below $\rho = 0.35$ mm^{-1}, which is visible when taking $t_{n+l} = 60{,}000$ cycles as a reference to compare Figure 5.19d, 5.19e and 5.19f. Additionally, as was the case for specimen 1-4, the confidence intervals decrease when t_n increases. Aside from the crack density, the PF algorithm has more difficulty with performing reliable prognostics of the delamination ratio d_r. As previously mentioned in the filtering step, d_r of specimen 2-2 is continuously underestimated. This is also reflected in Figure 5.20d, in which the delamination onset is not yet reflected in the particles. At $t_n =$ 42,500 cycles (Figure 5.20e) and $t_n = 55{,}000$ cycles (Figure 5.20f), the delamination ratio is

still underestimated at very low values (≈ 0.01 and 0.02 respectively). Two reasons for this discrepancy are identified: the absence of in-situ d_r measurements and a volatile behavior of model parameter m. The first has also been observed for specimen 1-4, which resulted in a delay in the increase of d_r. However, the second reason is more dominant for specimen 2-2 and it explains the difficulty in the RUL prediction. Looking at Figure 5.18, it can be observed that model parameter m fluctuates between ≈ 0.95 at $t_n = 15{,}000$ cycles and ≈ 0.85 at $t_n = 45{,}000$ cycles. Such an unreliable model parameter m causes the model parameters of the d_r phenomenological model to not be updated. This means that the particles with 'extremes' of m can show likely stiffness behavior for updating in the PF. This behavior is also visible in the normalized stiffness prognostics.

Using the two aforementioned damage properties at t_{n+l} (ρ and d_r), the static model parameters (h, i, j and k), and the model parameter m, the prognostics of the normalized stiffness is obtained. The stiffness degradation serves as direct input to the EOEFL failure criterion. It is clear in Figure 5.21b Figure 5.21c and Figure 5.21d that the prognostics of the stiffness degradation go slower than actually is the case for specimen 2-2. Additionally, a higher plateau region is predicted in the same figures. This is consistent with an excessively high value of model parameter m at those cycles. Later, in Figure 5.21e and Figure 5.21f, model parameter m is close to its minimum and is stabilizing towards the actual model parameter m for specimen 2-2 (Figure 5.18). This causes the plateau region to be present, and causes the delamination ratio prognostics in Figure 5.20e and Figure 5.20f to become more reliable. It is therefore identified that the phenomenological relation with model parameter introduces difficulties, for which a recommendation is stated in chapter 6.

Finally, in Figure 5.22, histograms at the same time steps t_n present the distribution of the RUL predictions of all particles. These histograms with the distribution of particles directly relate to the indicated mean and PI in Figure 5.2b. The high peak for RUL estimations at 100,000 cycles in Figure 5.22b and Figure 5.22c is present because the maximum number of iterations is set to 100,000 cycles. This means that, if a particle did not fail yet at that point, its RUL is set to zero and the algorithm moves on to the next filtering iteration t_{n+1}. The reason for high RUL predictions at $t_n = 10{,}000$ cycles, $t_n = 20{,}000$ cycles and $t_n = 30{,}000$ cycles is directly related to the aforementioned slow stiffness degradation prognostics due to model parameter m at the same filtering steps. After this point, at $t_n = 42{,}000$ cycles (Figure 5.22e), predictions quickly decrease to very low RUL estimations, while the specimen actually still has $\approx 20,000$ cycles left to EOEFL. This is difficult to explain in extensive detail due to the lack of transparency in the EOEFL failure criterion. In this criterion, the failed vector $\boldsymbol{F}$ is passed from filtering to prognostics loop at each t_n. This causes ambiguity as a failed particle's model parameters could evolve, but the RUL is immediately zero with the failed condition. Additionally, this failure criterion decreases computational efficiency because stiffness results should be stored for multiple filtering and prognostics steps to track degradation. Therefore, from these findings, a recommendation is formulated in chapter 6 to avoid such RUL failure criterion. This problem is not present if one would only be interested in the RUP up to t_{n+l}, or if degradation to EOL (macroscopic) failure would be modeled. However, this is not possible with the phenomenological relations and case study data in this thesis.

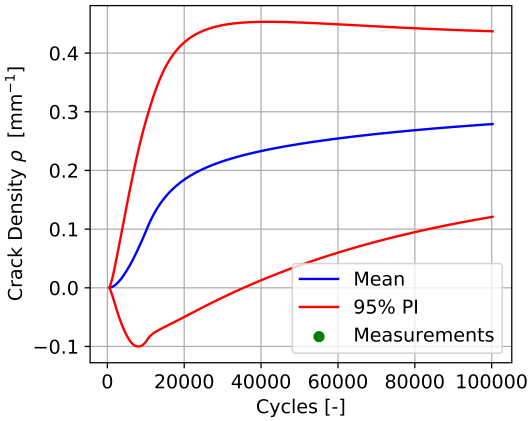

(a) 500 cycles

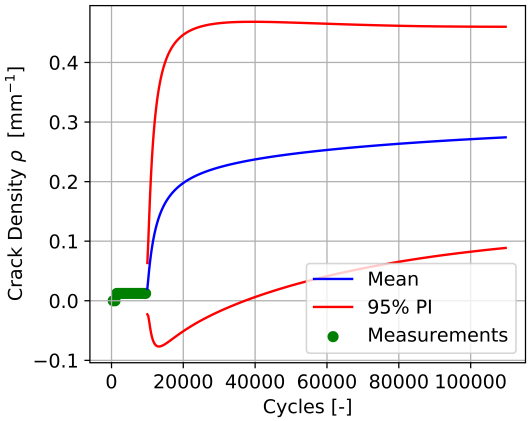

(b) 10,000 cycles

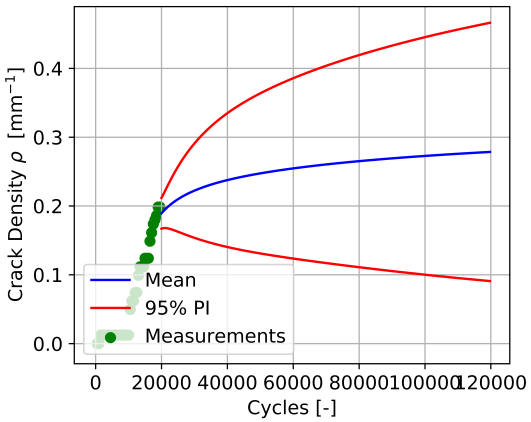

(c) 20,000 cycles

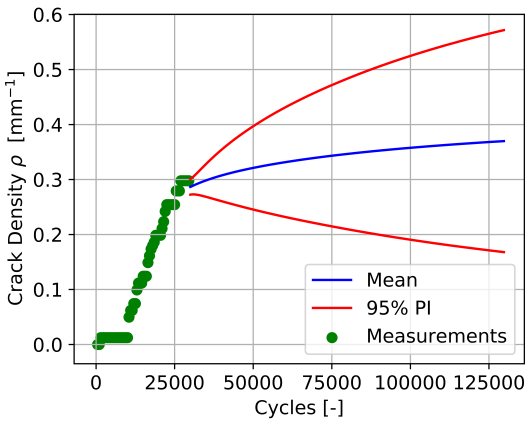

(d) 30,000 cycles

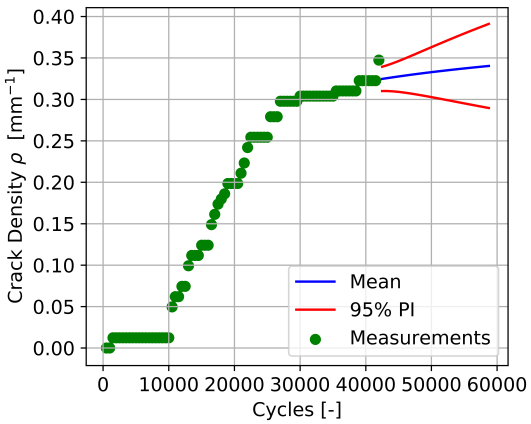

(e) 42,500 cycles

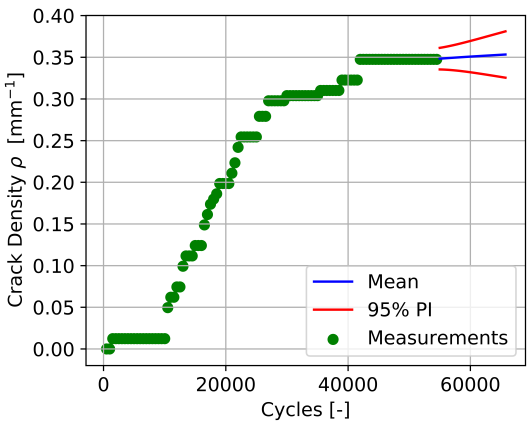

(f) 55,000 cycles

Figure 5.19: Results of the prognostics at distinct cycles of the transverse matrix crack density ρ for specimen 2-2 with indicative weighted mean and 95% prediction interval (PI) of the N_s particles.

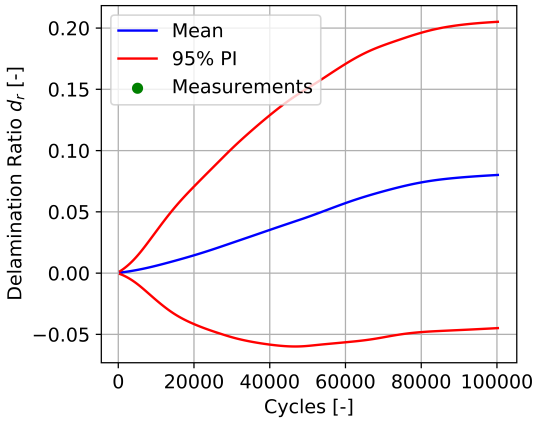

(a) 500 cycles

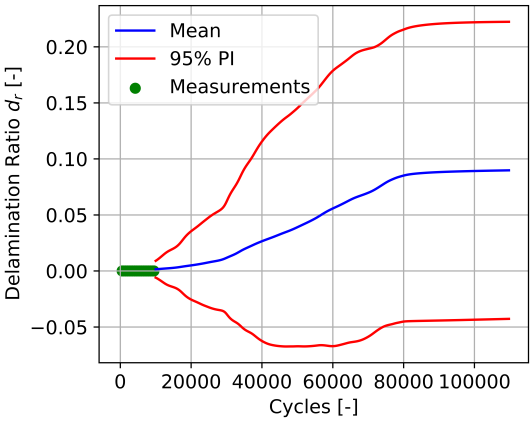

(b) 10,000 cycles

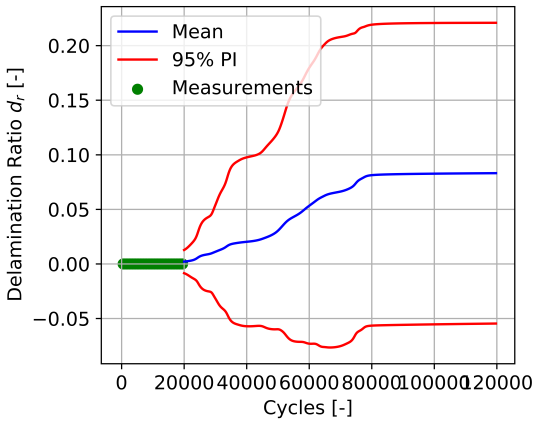

(c) 20,000 cycles

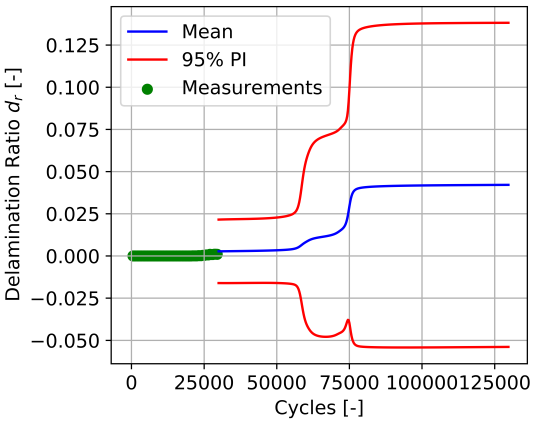

(d) 30,000 cycles

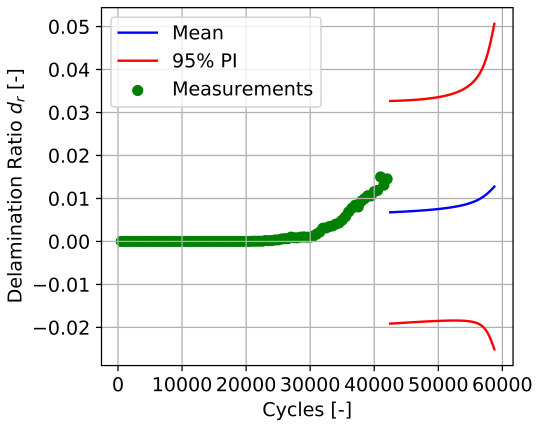

(e) 42,500 cycles

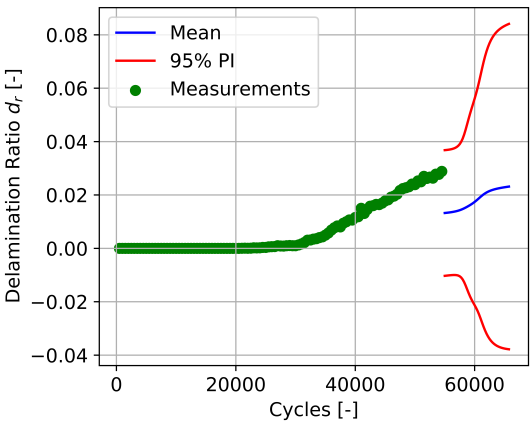

(f) 55,000 cycles

Figure 5.20: Results of the prognostics at distinct cycles of the delamination ratio d_r for specimen 2-2 with indicative weighted mean and 95% prediction interval (PI) of the N_s particles.

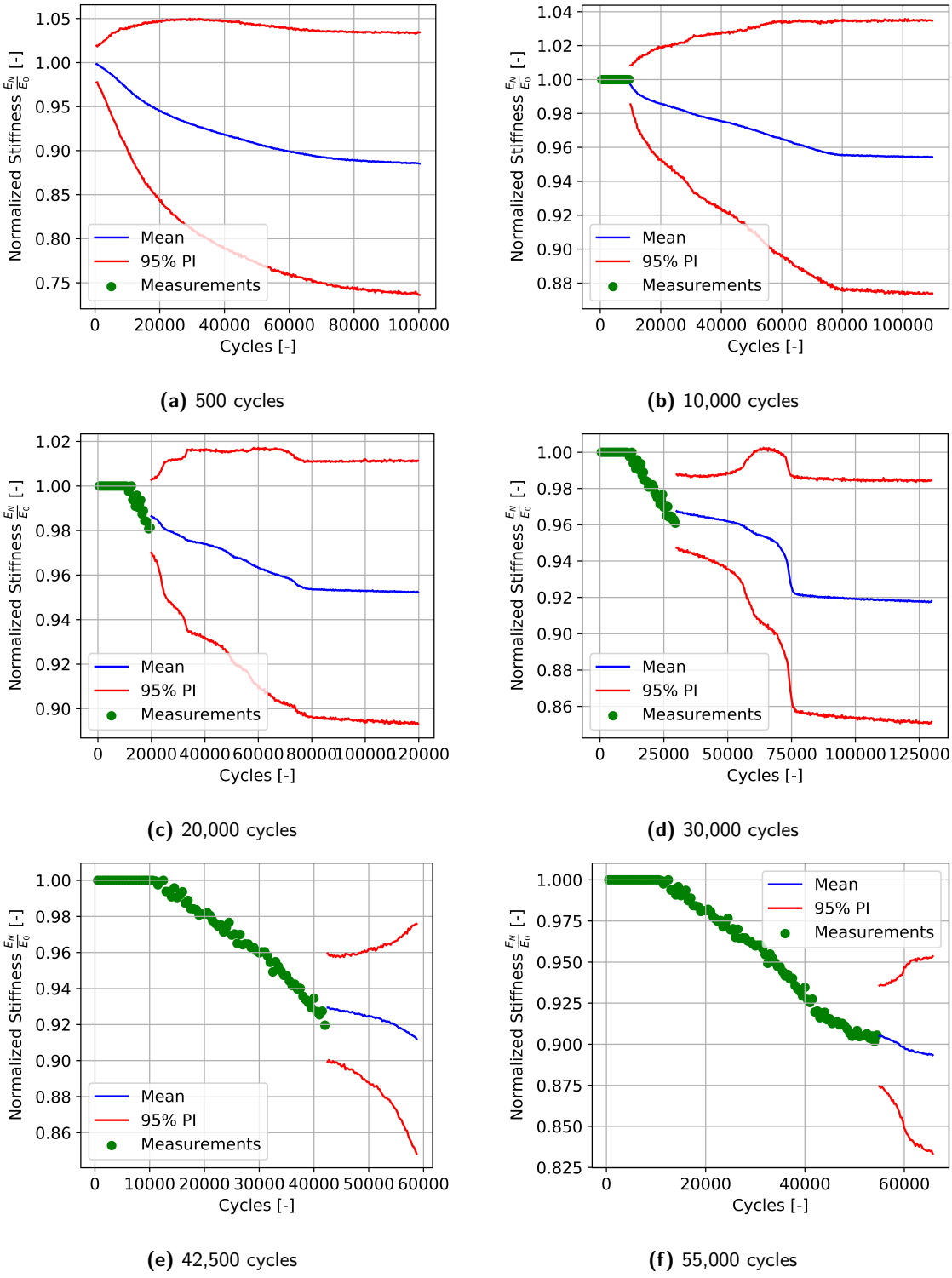

(a) 500 cycles

(b) 10,000 cycles

(c) 20,000 cycles

(d) 30,000 cycles

(e) 42,500 cycles

(f) 55,000 cycles

Figure 5.21: Results of the prognostics at distinct cycles of the normalized stiffness $\frac{E_N}{E_0}$ for specimen 2-2 with indicative weighted mean and 95% prediction interval (PI) of the N_s particles.

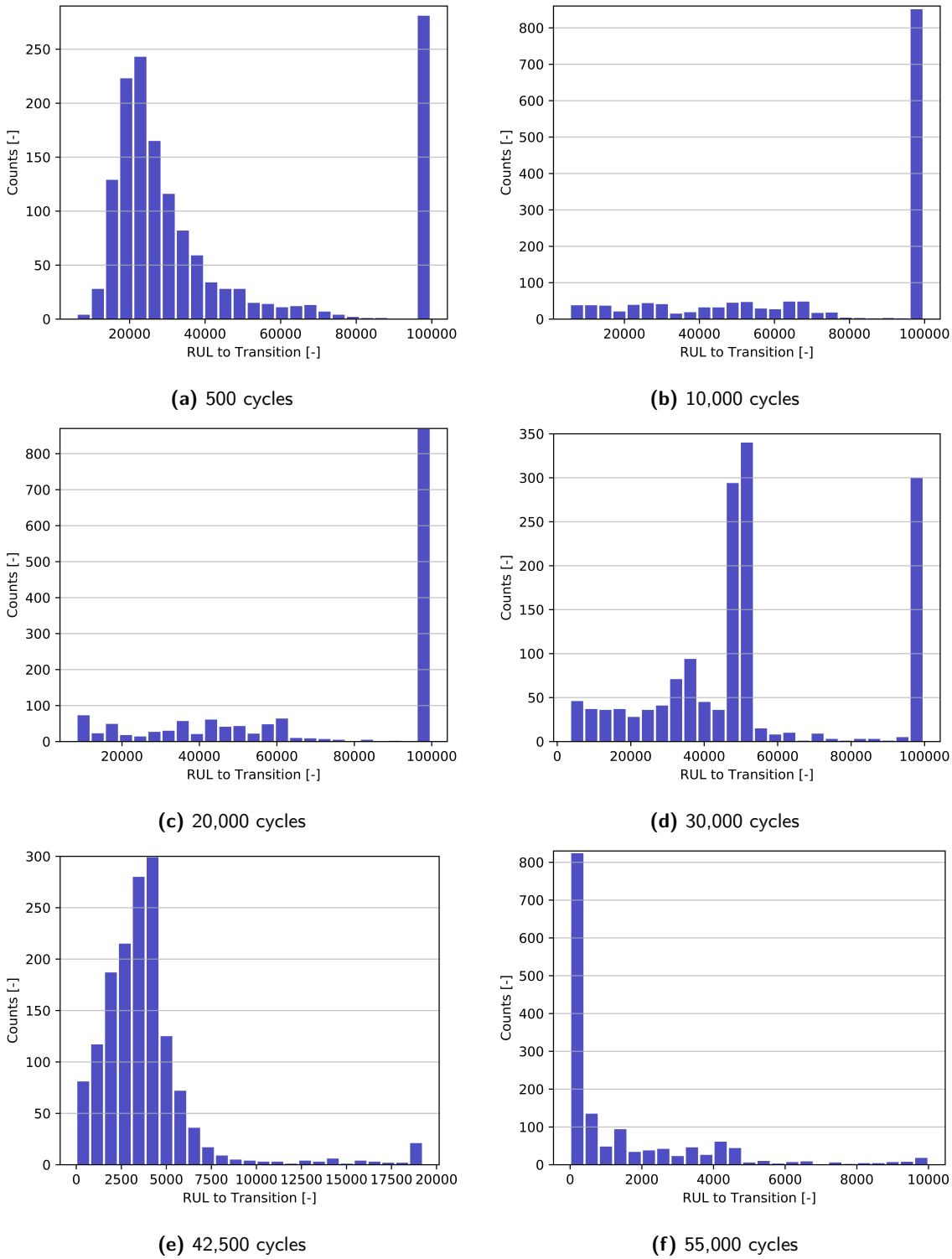

(a) 500 cycles

(b) 10,000 cycles

(c) 20,000 cycles

(d) 30,000 cycles

(e) 42,500 cycles

(f) 55,000 cycles

Figure 5.22: Results of the prognostics at distinct cycles of the remaining useful life (RUL) for stage I to II transition for specimen 2-2 with a histogram presenting the distribution of the N_s particles.

5.5 Sensitivity Analysis

To answer the last sub-question of the research question, the influence of the PF input parameters on the PF algorithm performance is investigated for specimen 1-4 and 2-2. As a baseline, the input parameters are identical to those presented in Table 5.1. However, to perform a sensitivity analysis, the identified hyperparameters in section 5.2 are altered one by one. First, the effect of increasing or decreasing the sample size N_s is demonstrated. After this, the effect of changing the threshold effective sample size N_{eff} and the random walk rate of convergence P^* are elaborated upon.

5.5.1 Sample Size

The effect of the sample size N_s is investigated for sample sizes of 75, 150, 300, 600, 1,000, 1,500, 2,000 and 4,000. For these sample sizes, the results for the RUL estimations of the PF algorithm are generated to quantify the performance metrics. In Table 5.7 and 5.8, the results are shown for specimen 1-4 and 2-2 respectively.

Table 5.7: Performance Metrics Results for Specimen 1-4 with Varying N_s

N_s	Precision	RMSE	MAPE	CRA	Convergence
75	11,359.297	15,359.66	76.16	0.238	22,821.942
150	12,250.473	15,710.47	82.031	0.18	23,091
300	10,661.861	11,730.299	53.665	0.463	19,967.788
600	10,466.481	11,022.072	57.844	0.422	19,977.507
1,000	7,408.518	7,806.619	38.661	0.613	17,973.822
1,500	**6,646.292**	**6,685.92**	**39.185**	**0.608**	**19,941.175**
2,000	6,665.319	6,670.143	39.237	0.608	20,849.974
4,000	7,338.914	7,361.915	42.613	0.574	20,915.41

Table 5.8: Performance Metrics Results for Specimen 2-2 with Varying N_s

N_s	Precision	RMSE	MAPE	CRA	Convergence
75	26,063.126	29,577.205	89.125	0.109	33,142.372
150	25,649.756	30,069.538	84.596	0.154	30,883.334
300	24,655.117	28,729.466	84.394	0.156	30,774.064
600	18,791.784	19,739.124	62.215	0.379	27546.633
1,000	17,304.741	17430.158	58.985	0.410	27,571.061
1,500	**17,107.874**	**18,426.185**	**59.924**	**0.401**	**27,338.085**
2,000	17,910.443	18,959.143	59.757	0.402	27,250.999
4,000	18,784.820	19,590.064	59.208	0.408	27,195.296

One can observe that the PF performance metrics score worse for both specimens when the sample size is low (≤ 600). This is clearly visible for the measure of spread, the precision. Additionally, the accuracy metrics RMSE, MAPE and CRA support this observation. In the convergence metric, this trend is observed, though less explicit. However, for sample sizes $N_s =\geq 1,000$, the improvements in performance metrics become less expressive when increasing the sample size. While the specific sample size at which this plateau is reached is

dependent on the application, this behavior is consistent with observations in other articles utilizing PF (Wang and Chaib-Draa, 2012; Elvira et al., 2017).

The asymptotic behavior that is observed when increasing the sample size can be well explained by the basic concepts of PF. The PF has a certain associated degree of randomness. That means, each adaptive model parameter for each particle is initialized to a value drawn from a uniform distribution in this case. However, many different adaptive model parameters are present, and one aims to find the most feasible combination of those (the most feasible particle) using the updating step. One can imagine that, if the sample size is very small, the probability of having a reasonably likely set is smaller than when a large sample size is used. It is important to note that this is a generalization, for instance, $N_s = 150$ for specimen 1-4 in Table 5.7 still scores weaker in terms of the prognostics metrics than when $N_s = 75$.

5.5.2 Threshold Effective Sample Size

The effect of the threshold effective sample size $N_{threshold}$ is investigated for values of 0.5, 0.7, 0.85, 0.95 and 1. For these thresholds, the results for the RUL estimations of the PF algorithm are generated to quantify the performance metrics. In Table 5.9 and 5.10, the results are shown for specimen 1-4 and 2-2 respectively.

Table 5.9: Performance Metrics Results for Specimen 1-4 with Varying $N_{threshold}$

$N_{threshold}$	Precision	RMSE	MAPE	CRA	Convergence
0.5	8,541.237	8,655.258	48.057	0.519	19,749.721
0.7	5,901.922	6,054.172	41.409	0.586	23,272.541
0.85	7,373.912	7,420.334	42.119	0.579	20,415.333
0.95	**6,646.292**	**6,685.92**	**39.185**	**0.608**	**19,941.175**
1	9,212.491	9,594.895	50.172	0.498	19,899.463

Table 5.10: Performance Metrics Results for Specimen 2-2 with Varying $N_{threshold}$

$N_{threshold}$	Precision	RMSE	MAPE	CRA	Convergence
0.5	18,112.525	18,668.508	60.178	0.398	27,507.89
0.7	18,313.609	18,800.422	61.329	0.387	27,441.657
0.85	18,154.996	19,085.941	60.262	0.397	27,203.267
0.95	**17,107.874**	**18,426.185**	**59.924**	**0.401**	**27,338.085**
1	18,009.439	18,817.91	58.983	0.41	27,263.577

One can observe that the PF precision, RMSE and MAPE performance metrics (minimizing is desirable) show a convex behavior for specimen 1-4. On the other hand, the CRA performance metric (maximizing is desirable) shows a clear concave behavior. This is expected due to the trade-off between weight degeneracy and sample impoverishment as mentioned in the resampling methodology (subsection 4.4.3). Therefore, both very high and low $N_{threshold}$ perform weaker than the other predictions. When $N_{threshold} = 0.85$, a higher precision and RMSE is observed compared to those of $N_{threshold} = 0.7$ and $N_{threshold} = 0.95$. However, one should keep in mind the inherent randomness of a PF algorithm depending on the initialization, and the fact that the CRA and MAPE of $N_{threshold} = 0.85$ have similar results as the other

two, which makes it a modestly sensitive RUL prognostics result. For specimen 2-2, this behavior is less expressive when changing $N_{threshold}$, indicating a lower sensitivity for a weaker performing specimen.

5.5.3 Random Walk Rate of Convergence

Lastly, the effect of the random walk rate of convergence P^* is investigated for convergence rates of 1E-2, 1E-3 and 1E-4. For these convergence rates, the results for the RUL estimations of the PF algorithm are generated to quantify the performance metrics. In Table 5.11 and 5.12, the results are shown for specimen 1-4 and 2-2 respectively.

Table 5.11: Performance Metrics Results for Specimen 1-4 with Varying P

P^*	Precision	RMSE	MAPE	CRA	Convergence
1.00E-02	8,134.179	8,251.222	40.526	0.59	18,157.693
1.00E-03	**6,646.292**	**6,685.92**	**39.185**	**0.608**	**19,941.175**
1.00E-04	7,539.002	7,539.002	39.257	0.6074	19,465.52

Table 5.12: Performance Metrics Results for Specimen 2-2 with Varying P

P^*	Precision	RMSE	MAPE	CRA	Convergence
1.00E-02	19,964.56	22,208.09	70.26	0.2974	29,010.658
1.00E-03	**17,107.87**	**18,426.19**	**59.924**	**0.401**	**27,338.085**
1.00E-04	18,664.98	20,652.99	67.147	0.329	27,992.165

One can observe that considerable sensitivity is present based on the CRA, MAPE, RMSE and precision metrics of specimen 2-2. According to those, $P^* = 1E-3$ is preferable to maximize the first mentioned metric and minimize the other three. Additionally, for specimen 1-4, a similar observation can be made, most explicitly in the RMSE results. In order to explain the sensitivity caused by the rate of convergence of the random walk, Equation 4.26 is used. Here, it is observed that a smaller value for P^* causes slower shrinkage of the random walk standard deviation $\sigma_{\xi_{n,j}}$, while for a larger P^* the standard deviation shrinks faster. In this case, a larger $P^* = 1E-2$ is consistent with converging too soon. This means that not enough variability is allowed for the model parameters when characteristic damage patterns occur at a larger amount of cycles. This mostly applies to the growth in delamination ratio, which often remains at a value close to 0 up to 20,000 cycles or more in this case study. On the other hand, the $P^* = 1E-4$ is consistent with insufficient convergence. This means that too much variability is still allowed when approaching EOEFL. In this case study for specimen 1-4 and 2-2, $P^* = 1E-3$ comes out as most suitable to balance the two aforementioned consequences.

Chapter 6

Conclusions and Recommendations

This last chapter concludes the thesis by pointing out the most significant findings that are related to the research (sub-)questions. Additionally, recommendations for future research in the field of prognostics of the remaining useful life and properties for composites are formulated based on these findings.

6.1 Conclusions

Due to the ever-increasing need to make aviation more sustainable, the focus is moving rapidly to high performance lightweight structures. While the answer for this weight reduction is often found in continuous fiber-reinforced composites, challenges remain for the online prognostics of the remaining useful life (RUL) and remaining useful properties (RUP) in order to facilitate condition-based maintenance of these damage-sensitive structures. As significant stiffness degradation manifests itself in early fatigue life, it was decided in this thesis to predict the RUP and RUL to end-of-early-fatigue life (EOEFL), defined as stage I to stage II transition. Recent observations have shown that not only matrix cracking is present in early fatigue life, but that both delamination and matrix cracking occur simultaneously. Keeping in mind the identified potential of particle filtering (PF) to deal with inherent uncertainties and variability in composite degradation, it was decided to combine the PF with phenomenological relations that predict both crack growth and delamination growth. Therefore, the main research question that is addressed, with several sub-questions along the way, is formulated as such:

To what extent can the remaining useful life and properties of cross-ply composites in early fatigue life be predicted using online sequential training of phenomenological model(s) embedded into a particle filter?

Using the case study data at hand, the PF framework is set up. It is recognized that the PF can be used to perform online training of non-linear least squares pre-trained phenomenological relations with high variance. Such pre-trained relations can be obtained with only

a small training dataset, immediately indicating the considerable benefit of a model-based approach compared to a data-driven approach. Along the way, sub-questions dealing with the implementation and model performance are re-iterated here.

- **Which measurable damage properties can be used to construct phenomenological relations for damage evolution of composites in early fatigue life?**

  Recent observations in literature identify transverse matrix cracking and delamination as dominant damage properties in damage evolution. These are both provided in the case study dataset and used to define phenomenological growth relations. For $\rho(\mathrm{N})$, which after differentiation yields $\Delta\rho(\mathrm{N}, \Delta\mathrm{N})$ in the PF algorithm, exponential behavior is identified. For $d_r(\mathrm{N})$ on the other hand, which after differentiation yields $\Delta d_r(N, \Delta N)$, a logistic behavior is observed. Aforementioned relations are fit using non-linear least squares and describe the trend well for each specimen separately. However, they do not generalize for all specimens, which means these model parameters are adaptive in PF.

- **How can the multicausality of stiffness degradation in early fatigue life be accounted for in a PF algorithm?**

  Composite degradation is described in terms of a normalized stiffness degradation. It is found that the crack- and delamination growth relations can be combined in the PF using the data provided on crack- and delamination induced stiffness degradation. For that purpose, $D_{tc}(\rho)$ and $D_{del}(d_r)$ are introduced as linear and exponential phenomenological relations respectively. However, due to the low variability observed between specimens, these are static model parameters in the PF. A single additional adaptive model parameter m is required in the relation $\frac{E_N}{E_0}(D_{tc}, D_{del})$ to relate stiffness degradation as a percentage of stage I stiffness degradation from the dataset to a total normalized stiffness.

- **How well does the model behave on case study data to predict the RUL in terms of prognostic evaluation metrics?**

  The RUL prognostics in terms of the performance metrics show significant differences between specimens. As such, a considerably good specimen (1-4) and weak specimen (2-2) are treated in extensive detail. It is apparent that model parameter m has a significant influence as it controls the combined normalized stiffness based on the crack density and delamination ratio. A lower value of m quickly decreases the normalized stiffness. For specimen 1-4, the range over which parameter m changes is smaller ($\approx$ 0.03) compared to specimen 2-2 ($\approx$ 0.1). It is observed that when the delamination ratio is larger than expected, it is compensated by the parameter m to match the incoming stiffness measurement in the filtering step. Therefore, recommendations are formulated below to get rid of model parameter m using another stiffness relation.

  The aforementioned delamination ratio is harder to predict than the crack density as observed from the comparison with actual offline data. This is expected as the delamination ratio measurement is not used to update the PF model parameters. A likelihood estimate of these model parameters is only made via the normalized stiffness $\frac{E_N}{E_0}$ likelihood, which also depends on crack growth model parameters and model parameter

m. However, it is promising to see in specimen 1-4 (with small variation in model parameter m) that even without using an in-situ delamination measurement, the RUP for the delamination damage property at future states is quite reliable. One should note that with the asymptote in the current $D_{del}(d_r)$ relation, the upper plateau of $d_r(N)$ cannot be reliably predicted (increase in d_r no longer reflected in the stiffness).

Aside from the discussion focusing on delaminations above, the PF algorithm manages to adapt based on characteristic damage behavior early in the lifetime when encountered in the crack measurements. This is clearly visible in the crack growth filtering results, for which model parameter c quickly adapts to a sudden exponential behavior.

Apart from the conclusions on the RUP prognostics, it is important to stress that an atypical type of failure criterion is used for RUL prognostics to EOEFL. Due to the large variability observed in stage transition stiffness $\frac{E_I}{E_0}$, a fixed threshold cannot be identified to define EOEFL. However, an asymptotic region characterizes stage II, which makes it possible to detect EOEFL in the PF when the normalized stiffness degrades less than 0.001 over 2500 cycles. This type of failure criterion on the degradation rate is rather atypical in PF and added by using a failure vector that is passed between subsequent filtering iterations, each particle with its corresponding prognostics. However, it is observed that the asymptotic type of failure criterion for RUL prognostics to EOEFL has disadvantages in terms of transparency and computational efficiency. The need for such failure criterion can be circumvented using strategies stated below as recommendations. It is also observed that 95% prediction intervals of RUP and RUL predictions are sometimes negative. This does not necessarily mean that particles have an actual negative value for that property, but it rather shows the limitations of estimating properties by assuming a normal distribution.

- **Which influence do the input parameters of the PF algorithm have on the model performance?**

  The influence of PF input parameters is evaluated using a sensitivity analysis on specimen 1-4 and 2-2. First, an asymptotic behavior is observed when increasing the sample size N_s, which is well explained. This is the case as for a small sample size, the probability of having an initially reasonably likely set is smaller than when a larger sample size is used. Secondly, a sensitivity analysis on the threshold effective sample size $\mathrm{N}_{threshold}$ shows convex behavior of metrics for which minimization is desirable and concave for the opposite case. This indicates a 'sweet spot' (very clear for specimen 1-4) in which weight degeneracy and sample impoverishment are balanced. Finally, it is found that a moderate rate of convergence of the random walk P^* is desirable. This is consistent with extremely low and high values of P^* that cause convergence to happen too soon (before characteristic damage behavior of delamination growth) and too late respectively.

It is concluded in this thesis that the potential of PF to offer adaptivity required for RUP prognostics of composites is identified, definitely for damage properties showing characteristic behavior in the early lifetime. However, reliable RUL estimation to EOEFL with the methodology set out in this thesis remains difficult. Especially the stiffness degradation model and the failure criterion for EOEFL generate difficulties. These are addressed in the subsequent recommendations to build towards robust and reliable RUL prognostics for composites.

6.2 Recommendations

Although all research questions have been answered in this thesis, other thoughts emerged in the process. Besides, due to the rather limited experience in industry with these models, it is likely that performance enhancements can be achieved based on this methodology. Unfortunately, due to the finite time resources allocated to this thesis, these ideas and observations are stated as recommendations for future work.

- When building future phenomenological models for properties with very small growth (crack growth and delamination growth in this case), it is recommended to use a log-scale to improve readability and reduce the risk of encountering overflow in computer software.
- Using the existing methodology, one could improve the initialization of particles when a larger dataset becomes available. This would give the option to use the established framework in which initialization can be done based on the best fit pre-training statistical distribution of a certain adaptive model parameter.
- It is observed that the asymptotic type of failure criterion for RUL prognostics to EOEFL has disadvantages in lacking transparency and decreasing computational efficiency (stiffness results stored for multiple filtering steps). Another corresponding difficulty is that, when resampling occurs, a resampled particle is passing the boolean for failure of the previous filtering step, while in fact the model parameters can evolve. Therefore, it is suggested as a recommendation that a fixed threshold is preferable in future PF algorithms, if the specific application allows this. If one would only be interested in the RUP, a feasible approach would be to always predict a pre-defined number of states ahead.
- For now, RUP and RUL prognostics are performed up to EOEFL. Therefore, a suitable next step would be to extend the methodology (with additional/different phenomenological relations) towards stage II, III or macroscopic failure. The latter would also allow for a fixed stiffness threshold for end-of-life as desirable according to the aforementioned recommendation.
- The reliability of the RUP and RUL prognostics is compromised by the dependency on model parameter m. Therefore, it would be desirable to combine the existing or similar phenomenological relations for crack and delamination growth using an alternative model to obtain the normalized stiffness. A feasible approach would be to train a surrogate model on synthetic data, generated with finite element modeling simulations. Model parameters of such surrogate model can serve as adaptive model parameters in the PF framework presented in this thesis.

Bibliography

Ageyeva, T., Bárány, T., and Karger-Kocsis, J. (2019). *Composites*, pages 481–578. Springer International Publishing, Cham.

Andrieu, C., Doucet, A., and Holenstein, R. (2010). Particle Markov chain Monte Carlo methods. *Royal Statistical Society*, 72:269–342.

Barber, D. (2012). *Bayesian Reasoning and Machine Learning*. Cambridge University Press.

Brunner, A. J. (2018). Scatter, Scope and Structures: What fatigue fracture testing of fiber polymer composites is all about. *IOP Conference Series: Materials Science and Engineering*, 388(1).

Cadini, F., Sbarufatti, C., Corbetta, M., Cancelliere, F., and Giglio, M. (2019). Particle filtering-based adaptive training of neural networks for real-time structural damage diagnosis and prognosis. *Structural Control and Health Monitoring*, 26(12):1–19.

Callister, W. D. and Rethwisch, D. G. (2014). *Materials Science and Engineering: an Introduction*. Wiley, 9 edition.

Candy, J. V. (2016). *Bayesian Signal Processing: Classical, Modern,and Particle Filtering Methods*. Wiley, Hoboken, New Jersey, 2 edition.

Chiachío, J., Chiachío, M., Sankararaman, S., Saxena, A., and Goebel, K. (2015a). Condition-based prediction of time-dependent reliability in composites. *Reliability Engineering and System Safety*, 142:134–147.

Chiachío, J., Chiachío, M., Saxena, A., Sankararaman, S., Rus, G., and Goebel, K. (2015b). Bayesian model selection and parameter estimation for fatigue damage progression models in composites. *International Journal of Fatigue*, 70:361–373.

Chiachío Ruano, M. and Rus Carlborg, G. (2014). *Methods for Prognostics and Reliability in Composite Materials Using Structural Health Monitoring*. PhD thesis, Unversidad de Granada.

Corbetta, M., Sbarufatti, C., Giglio, M., Saxena, A., and Goebel, K. (2018). A Bayesian framework for fatigue life prediction of composite laminates under co-existing matrix cracks and delamination. *Composite Structures*, 187:58–70.

Daigle, M. J. and Goebel, K. (2013). Model-based prognostics with concurrent damage progression processes. *IEEE Transactions on Systems, Man, and Cybernetics Part A:Systems and Humans*, 43(3):535–546.

Daniel, I. M. and Ishai, O. (2006). *Engineering mechanics of composite materials*. Oxford University Press, New York.

de Myttenaere, A., Golden, B., Le Grand, B., and Rossi, F. (2016). Mean Absolute Percentage Error for regression models. *Neurocomputing*, 192:38–48.

Derriso, M. M., McCurry, C. D., and Schubert Kabban, C. M. (2016). A novel approach for implementing structural health monitoring systems for aerospace structures. *Structural Health Monitoring (SHM) in Aerospace Structures*, pages 33–56.

EASA (2017). Certification, Type Design Definition, Material and Process Qualification for Composite Light Aircraft CM-S-006.

Elattar, H. M., Elminir, H. K., and Riad, A. M. (2016). Prognostics: a literature review. *Complex & Intelligent Systems*, 2(2):125–154.

Eleftheroglou, N. (2020). *Adaptive prognostics for remaining useful life of composite structures*. PhD thesis, Delft University of Technology.

Eleftheroglou, N., Zarouchas, D., Loutas, T., Alderliesten, R., and Benedictus, R. (2018). Structural health monitoring data fusion for in-situ life prognosis of composite structures. *Reliability Engineering and System Safety*.

Elvira, V., Miguez, J., and Djurie, P. M. (2017). Adapting the Number of Particles in Sequential Monte Carlo Methods Through an Online Scheme for Convergence Assessment. *IEEE Transactions on Signal Processing*, 65(7):1781–1794.

Farrar, C. R. and Lieven, N. A. (2006). Damage prognosis: The future of structural health monitoring. *Philosophical Transactions of the Royal Society A: Mathematical, Physical and Engineering Sciences*, 365(1851):623–632.

Gamstedt, E. K. and Sjögren, B. A. (1999). Micromechanisms in tension-compression fatigue of composite laminates containing transverse plies. *Composites Science and Technology*, 59(2):167–178.

Gavin, H. P. (2019). The Levenburg-Marqurdt Algorithm For Nonlinear Least Squares Curve-Fitting Problems. *Duke University*, pages 1–19.

Ghoshal, A., Sundaresan, M. J., Schulz, M. J., and Frank Pai, P. (2000). Structural health monitoring techniques for wind turbine blades. *Journal of Wind Engineering and Industrial Aerodynamics*, 85(3):309–324.

Giurgiutiu, V. (2020). Structural health monitoring (SHM) of aerospace composites. In *Polymer Composites in the Aerospace Industry*. Elsevier Ltd.

Goebel, K., Saxena, A., Saha, S., Saha, B., and Celaya, J. (2012). Prognostic Performance Metrics. *Machine Learning and Knowledge Discovery for Engineering Systems Health Management*, pages 147–177.

Gordon, N., Salmond, D., and Smith, A. (1993). Novel approach to nonlinear and linear Bayesian state estimation.

Hamdan, A., Sultan, M., and Mustapha, F. (2019). Structural health monitoring of biocomposites, fibre-reinforced composites, and hybrid composite. *Structural Health Monitoring of Biocomposites, Fibre-Reinforced Composites and Hybrid Composites*, pages 227–242.

Hu, Y., Liu, S., Lu, H., and Zhang, H. (2019). Remaining Useful Life Model and Assessment of Mechanical Products: A Brief Review and a Note on the State Space Model Method. *Chinese Journal of Mechanical Engineering (English Edition)*, 32(1).

Jollivet, T., Peyrac, C., and Lefebvre, F. (2013). Damage of composite materials. *Procedia Engineering*, 66:746–758.

Kassapoglou, C. (2013). *Review of Classical Laminated Plate Theory*, chapter 3, pages 33–53. John Wiley & Sons, Ltd.

Khan, T. A., Kim, H., and Kim, H.-J. (2019). Fatigue delamination of carbon fiber-reinforced polymer-matrix composites. *Failure Analysis in Biocomposites, Fibre-Reinforced Composites and Hybrid Composites*, pages 1–28.

Kim, N. H., Choi, J. H., and An, D. (2016). *Prognostics and health management of engineering systems: An introduction*. Springer International Publishing.

Knab, D., Baban, S. C., Schlosser, A., Seidel, P., Lok, C., and Knoblinger, T. (2018). What's next for aerospace composites? Technical report, Arthur D. Little Luxembourg S.A., Luxembourg.

Kollár, L. P. and Springer, G. S. (2003). Laminated Composites. In *Mechanics of Composite Structures*, pages 63–88. Cambridge University Press.

Kuan, C.-M. (2004). Nonlinear Least Squares Theory.

Kupski, J., Teixeira de Freitas, S., Zarouchas, D., Camanho, P. P., and Benedictus, R. (2019). Composite layup effect on the failure mechanism of single lap bonded joints. *Composite Structures*, 217(February):14–26.

Li, T., Bolic, M., and Djuric, P. M. (2015). Resampling Methods for Particle Filtering: Classification, implementation, and strategies. *IEEE signal processing magazine*, 32(3):70–86.

Li, T., Sattar, T. P., and Tang, D. (2013). A Fast Resampling Scheme for Particle Filters. (April 2014).

Li, X., Kupski, J., Teixeira De Freitas, S., Benedictus, R., and Zarouchas, D. (2020). Unfolding the early fatigue damage process for CFRP cross-ply laminates. *International Journal of Fatigue*, 140(April).

Loutas, T., Eleftheroglou, N., and Zarouchas, D. (2017). A data-driven probabilistic framework towards the in-situ prognostics of fatigue life of composites based on acoustic emission data. *Composite Structures*.

Mangalgiri, P. D. (1999). Composite materials for aerospace applications. *Bulletin of Materials Science*, 22(3):657–664.

Marseguerra, M., Zio, E., and Podofillini, L. (2002). Condition-based maintenance optimization by means of genetic algorithms and Monte Carlo simulation. *Reliability Engineering & System Safety*, 77(2):151–165.

Matplotlib. Available at https://matplotlib.org/.

McCarthy, C. and Vaughan, T. (2015). Micromechanical failure analysis of advanced composite materials. *Numerical Modelling of Failure in Advanced Composite Materials*, pages 379–409.

Numpy. Available at https://numpy.org/.

Orhan, E. (2012). Particle Filtering.

Pandas. Available at https://pandas.pydata.org/.

Persson, H. J. and Ståhl, G. (2020). Characterizing uncertainty in forest remote sensing studies. *Remote Sensing*, 12(3).

Pusch, J. and Wohlmann, B. (2018). Chapter 2 - Carbon Fibers. In Mahltig, B. and Kyosev, Y., editors, *Inorganic and Composite Fibers*, The Textile Institute Book Series, pages 31–51. Woodhead Publishing.

Python. Available at https://www.python.org/.

Ribeiro, M. L., Tita, V., and Vandepitte, D. (2011). Failure models for composite structures under compression loading. In *Proceedings of COBEM 2011*, volume 1.

Sankararaman, S. (2012). *Uncertainty Quantification and Integration in Engineering Systems*. Vanderbilt University.

Sankararaman, S. and Goebel, K. (2013). Why is the remaining useful life prediction uncertain? *PHM 2013 - Proceedings of the Annual Conference of the Prognostics and Health Management Society 2013*, 4(January 2013):337–349.

SciPy. Available at https://www.scipy.org/.

Scott, D. W. (2009). Sturges' rule. *WIREs Computational Statistics*, 1(3):303–306.

Shufeng, L., Xiaoquan, C., Yunyan, X., Jianwen, B., and Xin, G. (2015). Study on impact performances of scarf-repaired carbon fiber reinforced polymer laminates. *Journal of Reinforced Plastics and Composites*, 34(1):60–71.

Srini, S. (2019). Particle Filter : A hero in the world of Non-Linearity and Non-Gaussian.

Talreja, R. (2003). Modern Trends in Composite Laminates Mechanics. In *Modern Trends in Composite Laminates Mechanics*, chapter 3, pages 281–294. Springer-Verlag Wien, 1 edition.

Taylor, J. R. and Thompson, W. (1998). An Introduction to Error Analysis: The Study of Uncertainties in Physical Measurements.

Tibaduiza, D., Torres-Arredondo, M. Á., Vitola, J., Anaya, M., and Pozo, F. (2018). A Damage Classification Approach for Structural Health Monitoring Using Machine Learning. *Complexity*, 2018.

Wang, Y. and Chaib-Draa, B. (2012). A marginalized particle Gaussian process regression. *Advances in Neural Information Processing Systems*, 2:1187–1195.

Wicaksono, S. and Chai, G. B. (2013). A review of advances in fatigue and life prediction of fiber-reinforced composites. *Proceedings of the Institution of Mechanical Engineers, Part L: Journal of Materials: Design and Applications*, 227(3):179–195.

Worden, K., Farrar, C. R., Manson, G., and Park, G. (2007). The fundamental axioms of structural health monitoring. *Proceedings of the Royal Society A: Mathematical, Physical and Engineering Sciences*, 463(2082):1639–1664.

Appendix A

Remaining Useful Properties Prognostics Results of Other Specimens

A.1 Specimen 1-1

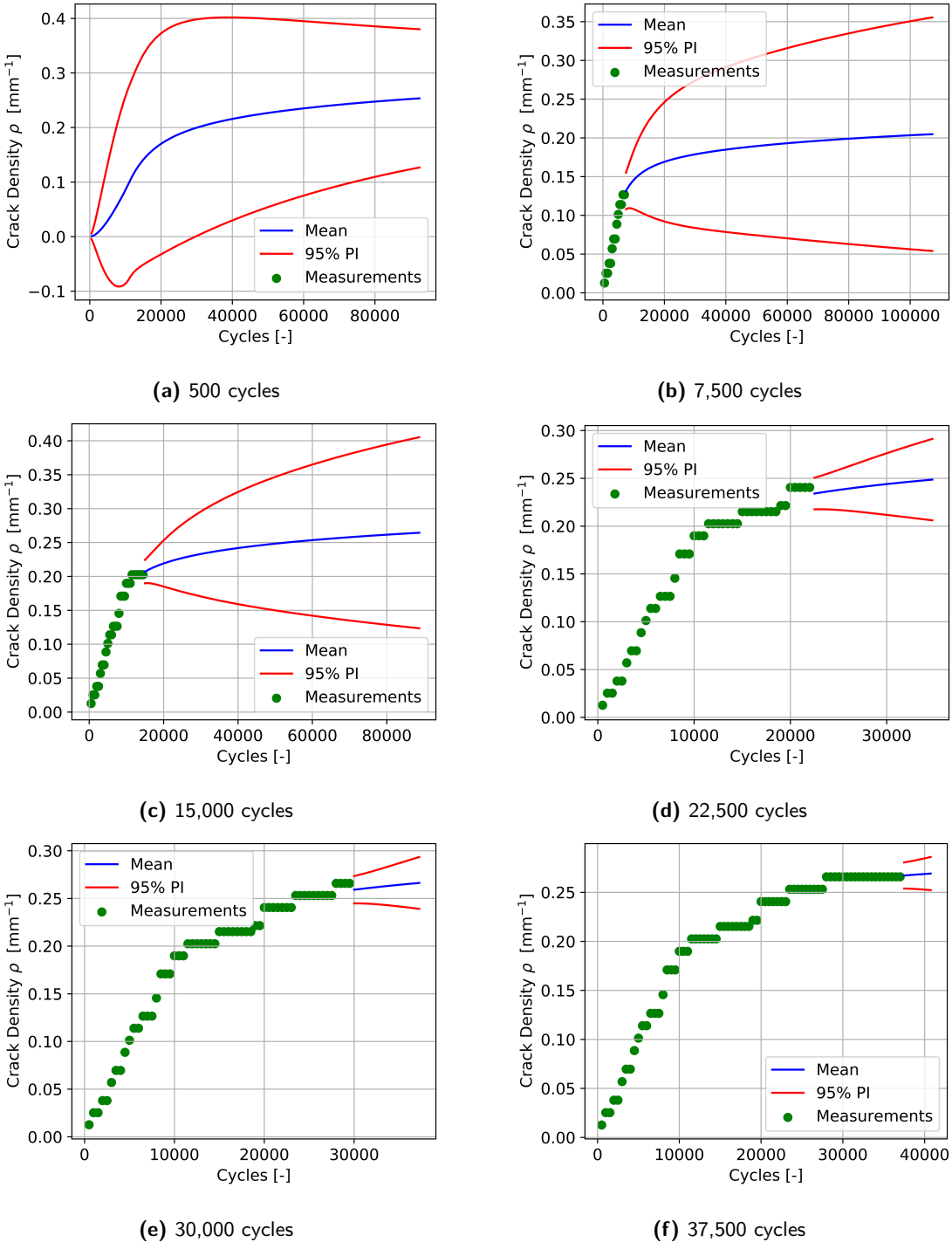

(a) 500 cycles

(b) 7,500 cycles

(c) 15,000 cycles

(d) 22,500 cycles

(e) 30,000 cycles

(f) 37,500 cycles

Figure A.1: Results of the prognostics at distinct cycles of the transverse matrix crack density ρ for specimen 1-1 with indicative weighted mean and 95% prediction interval (PI) of the N_s particles.

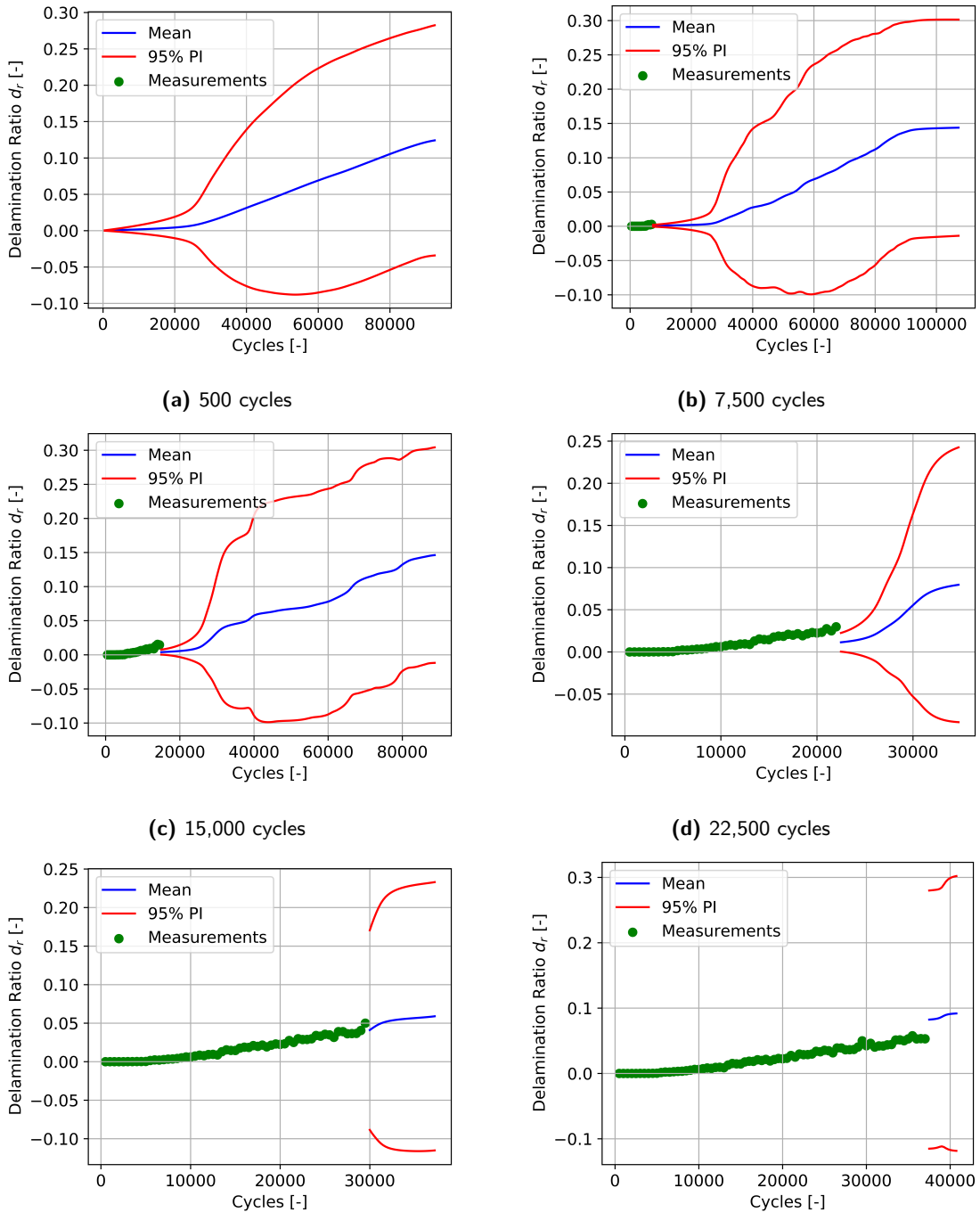

(a) 500 cycles

(b) 7,500 cycles

(c) 15,000 cycles

(d) 22,500 cycles

(e) 30,000 cycles

(f) 37,500 cycles

Figure A.2: Results of the prognostics at distinct cycles of the delamination ratio d_r for specimen 1-1 with indicative weighted mean and 95% prediction interval (PI) of the N_s particles.

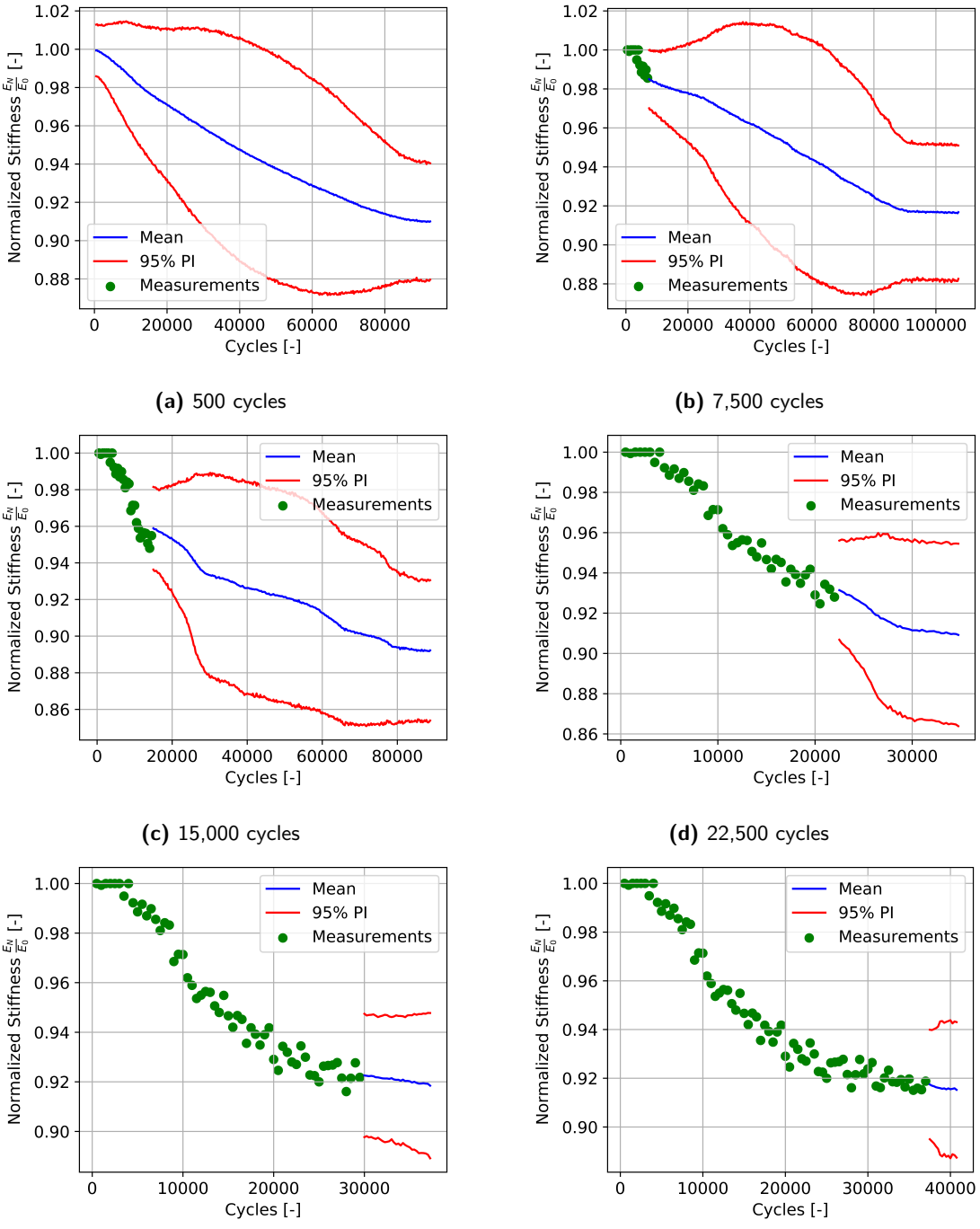

(a) 500 cycles

(b) 7,500 cycles

(c) 15,000 cycles

(d) 22,500 cycles

(e) 30,000 cycles

(f) 37,500 cycles

Figure A.3: Results of the prognostics at distinct cycles of the normalized stiffness $\frac{E_N}{E_0}$ for specimen 1-1 with indicative weighted mean and 95% prediction interval (PI) of the N_s particles.

A.2 Specimen 1-2

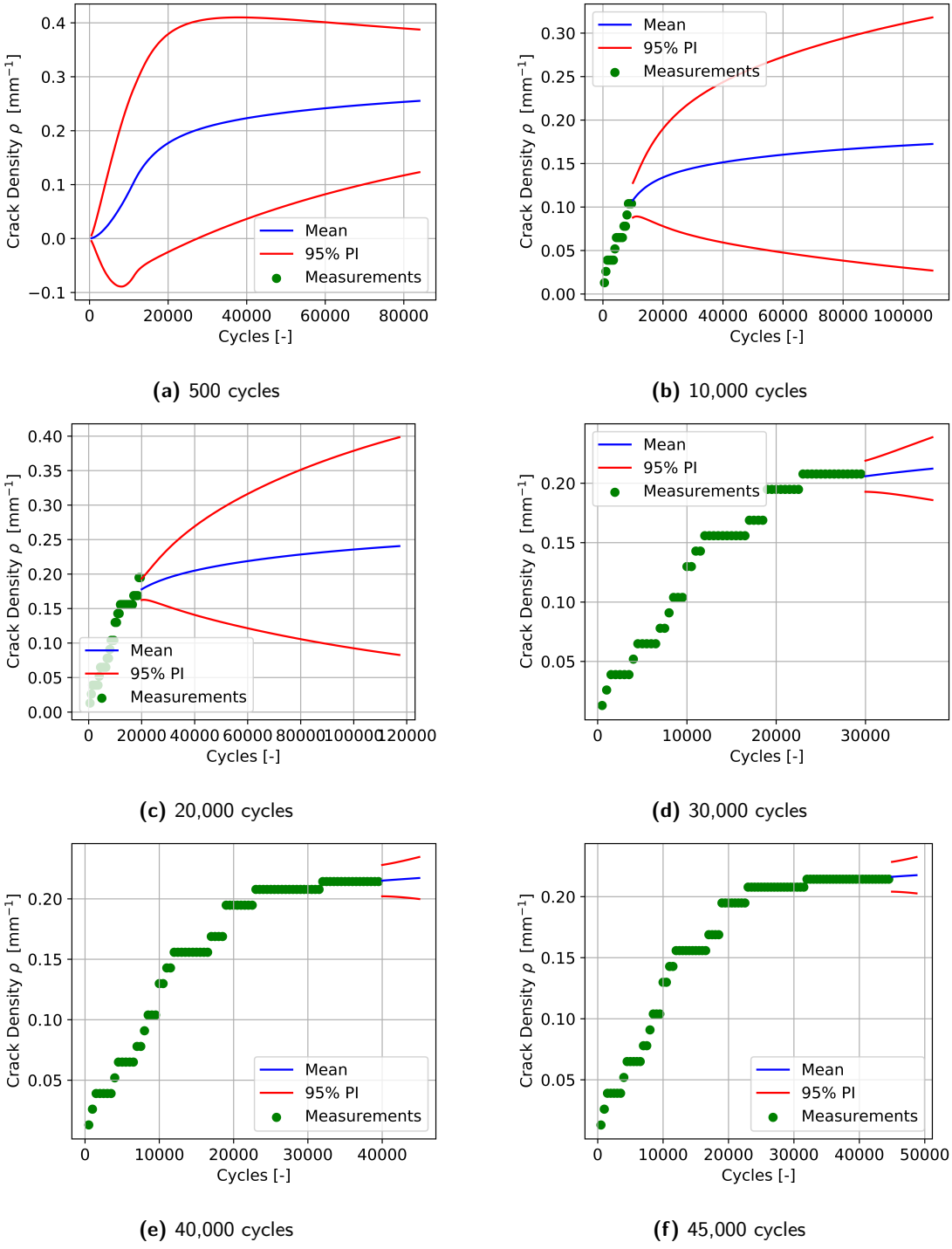

(a) 500 cycles

(b) 10,000 cycles

(c) 20,000 cycles

(d) 30,000 cycles

(e) 40,000 cycles

(f) 45,000 cycles

Figure A.4: Results of the prognostics at distinct cycles of the transverse matrix crack density ρ for specimen 1-2 with indicative weighted mean and 95% prediction interval (PI) of the N_s particles.

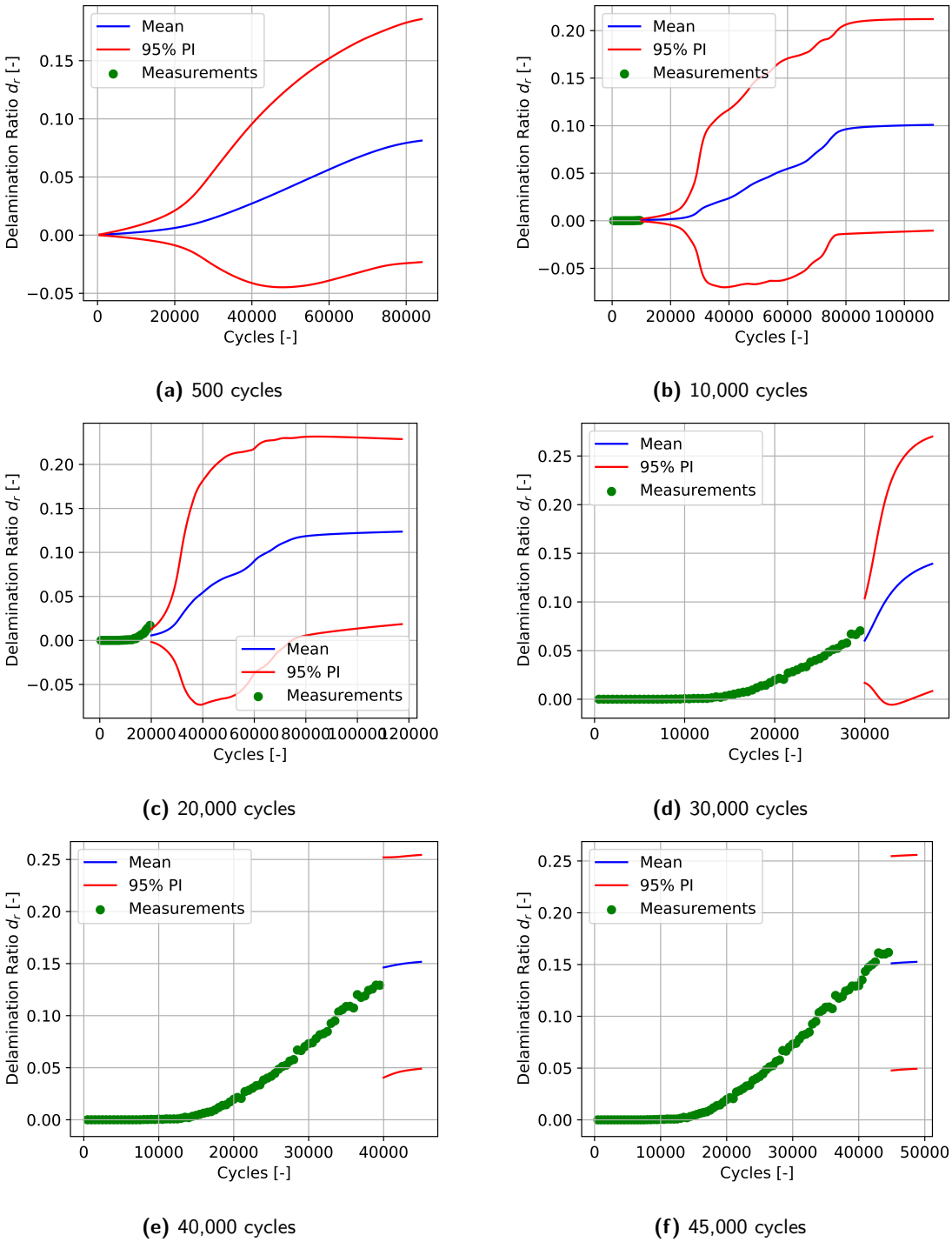

(a) 500 cycles

(b) 10,000 cycles

(c) 20,000 cycles

(d) 30,000 cycles

(e) 40,000 cycles

(f) 45,000 cycles

Figure A.5: Results of the prognostics at distinct cycles of the delamination ratio d_r for specimen 1-2 with indicative weighted mean and 95% prediction interval (PI) of the N_s particles.

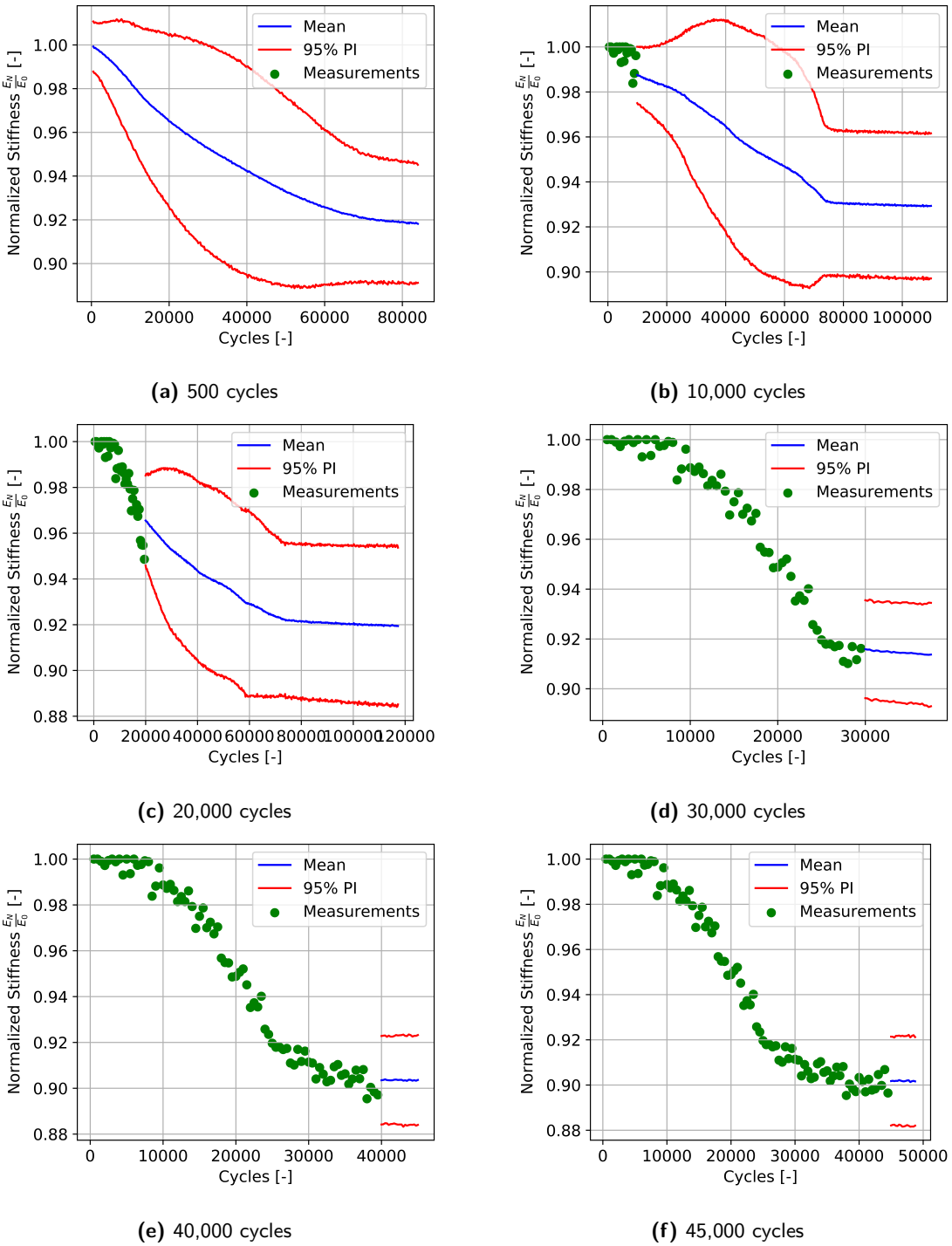

(a) 500 cycles

(b) 10,000 cycles

(c) 20,000 cycles

(d) 30,000 cycles

(e) 40,000 cycles

(f) 45,000 cycles

Figure A.6: Results of the prognostics at distinct cycles of the normalized stiffness $\frac{E_N}{E_0}$ for specimen 1-2 with indicative weighted mean and 95% prediction interval (PI) of the N_s particles.

A.3 Specimen 1-3

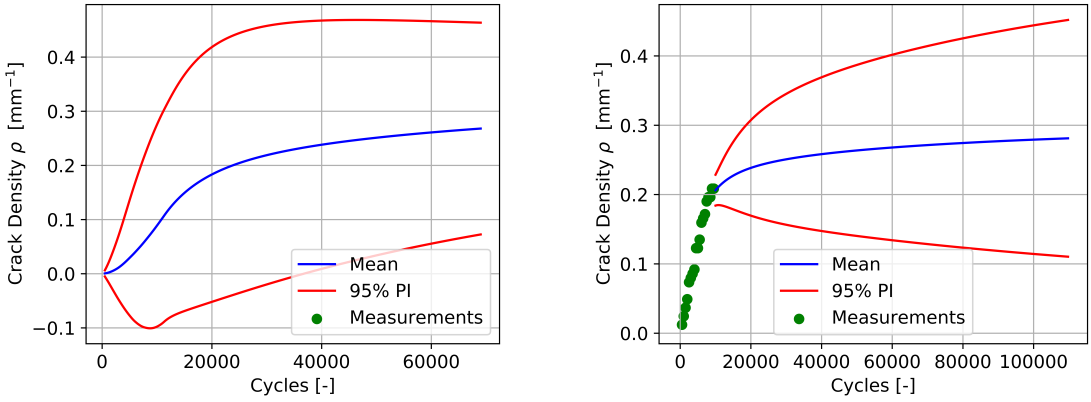

(a) 500 cycles

(b) 10,000 cycles

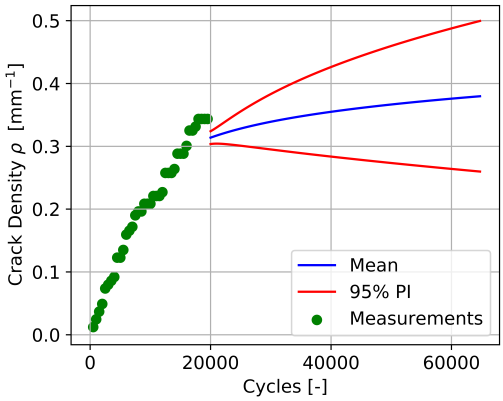

(c) 20,000 cycles

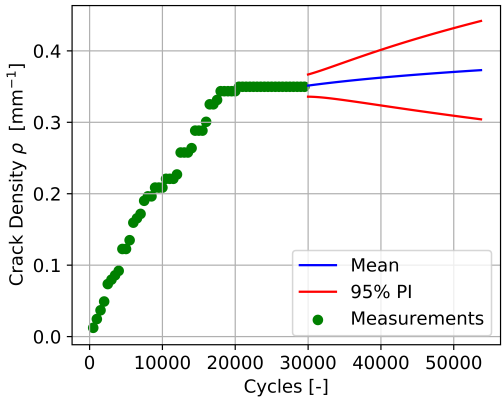

(d) 30,000 cycles

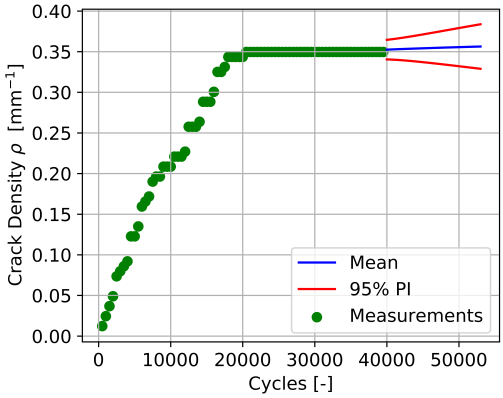

(e) 40,000 cycles

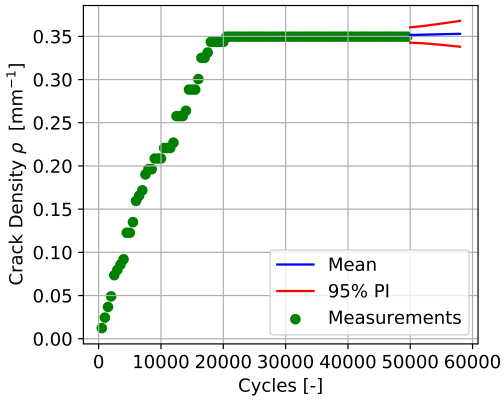

(f) 50,000 cycles

Figure A.7: Results of the prognostics at distinct cycles of the transverse matrix crack density ρ for specimen 1-3 with indicative weighted mean and 95% prediction interval (PI) of the N_s particles.

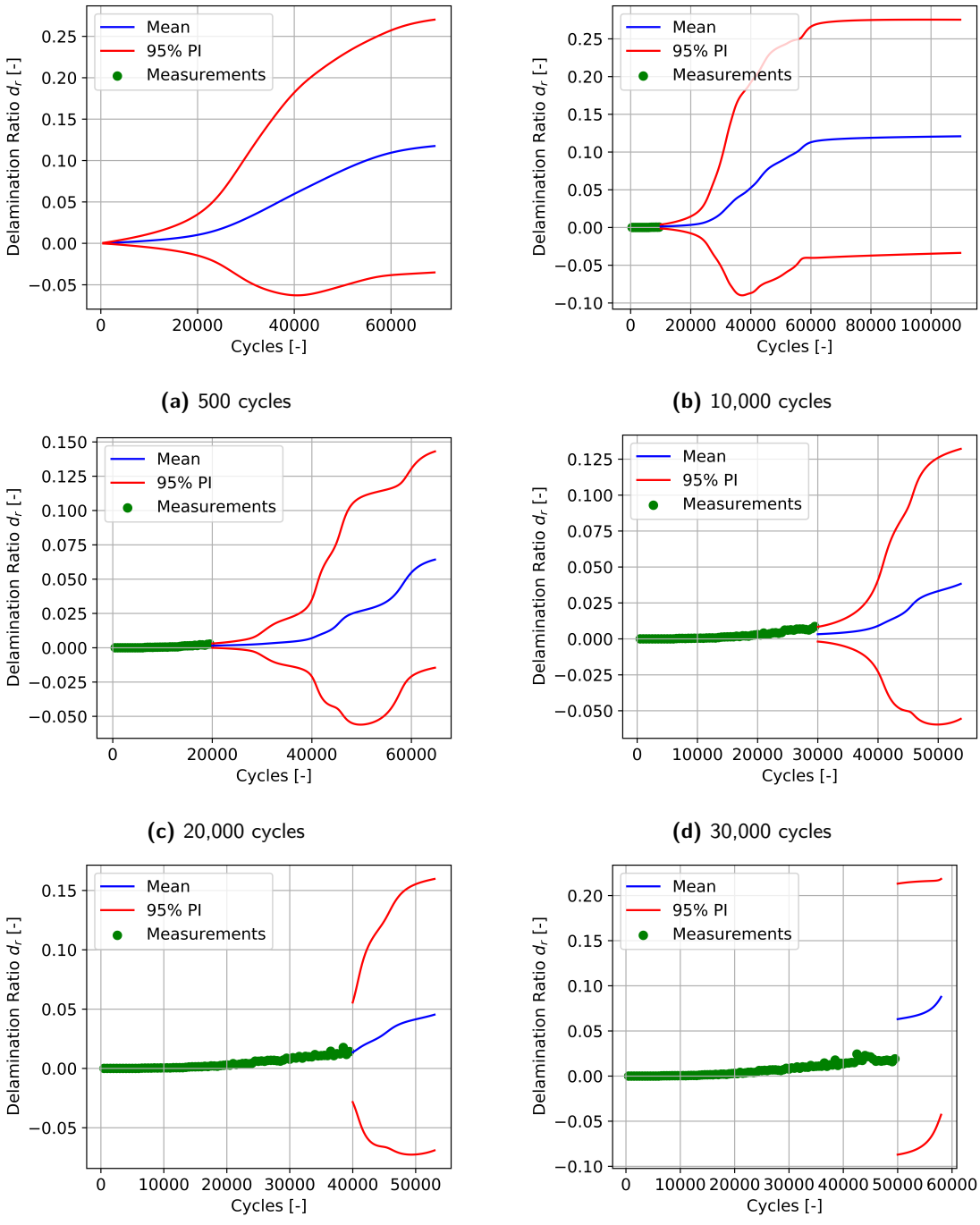

(a) 500 cycles

(b) 10,000 cycles

(c) 20,000 cycles

(d) 30,000 cycles

(e) 40,000 cycles

(f) 50,000 cycles

Figure A.8: Results of the prognostics at distinct cycles of the delamination ratio d_r for specimen 1-3 with indicative weighted mean and 95% prediction interval (PI) of the N_s particles.

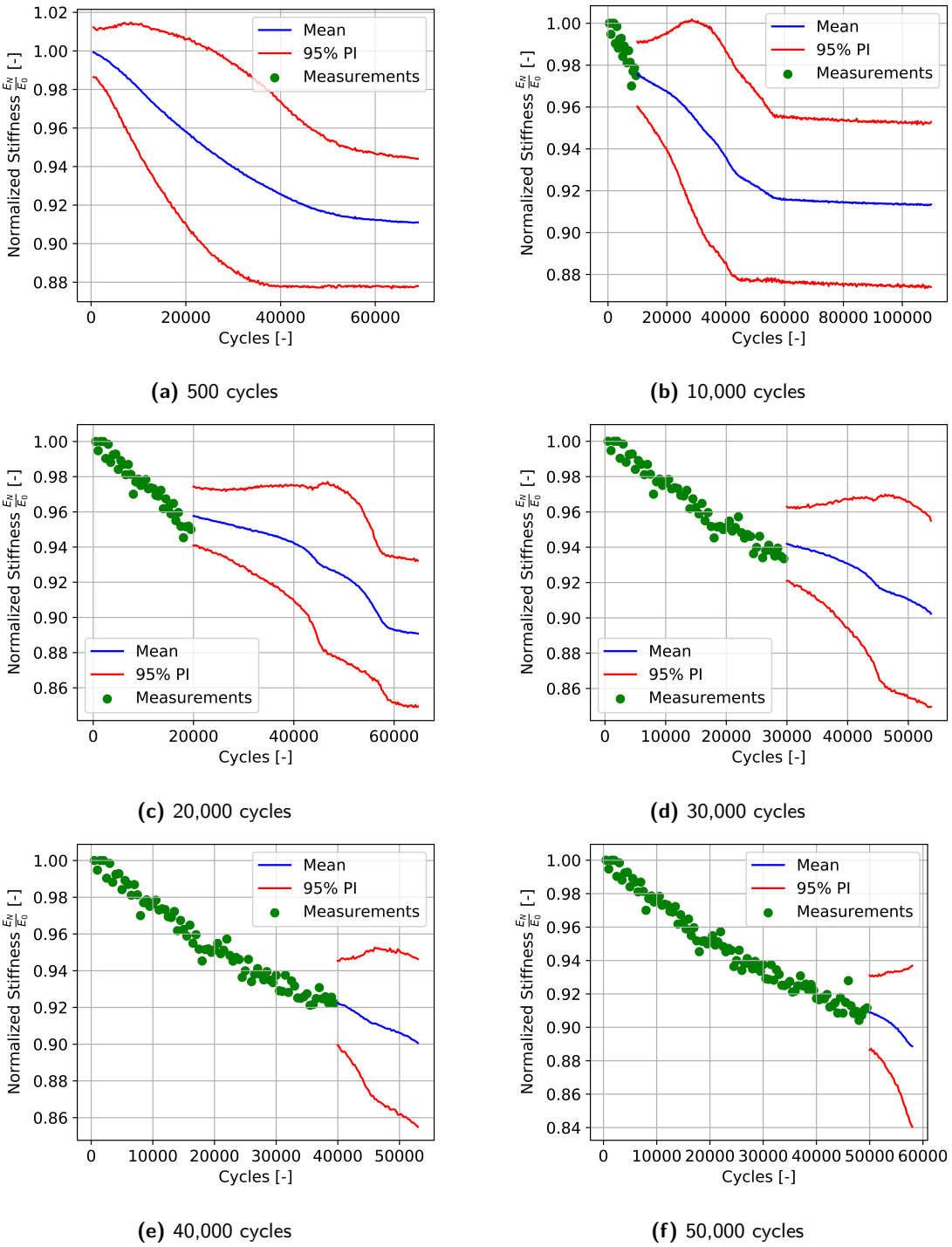

(a) 500 cycles

(b) 10,000 cycles

(c) 20,000 cycles

(d) 30,000 cycles

(e) 40,000 cycles

(f) 50,000 cycles

Figure A.9: Results of the prognostics at distinct cycles of the normalized stiffness $\frac{E_N}{E_0}$ for specimen 1-3 with indicative weighted mean and 95% prediction interval (PI) of the N_s particles.

A.4 Specimen 2-1

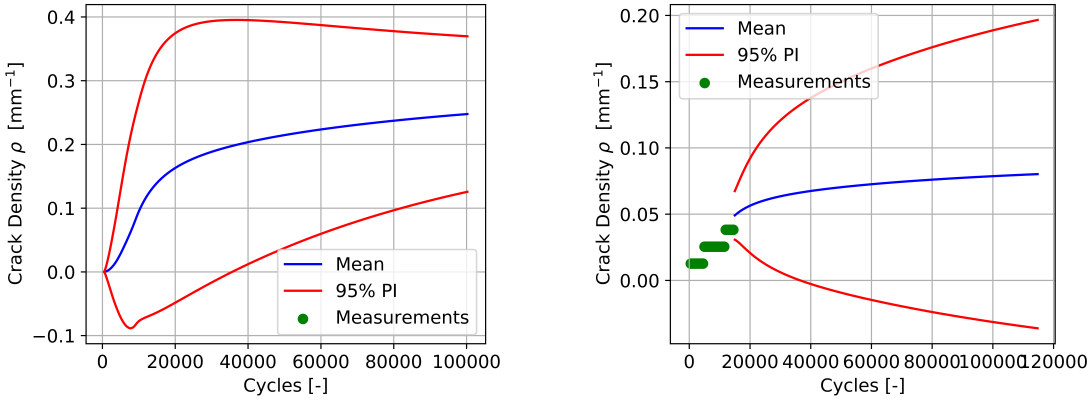

(a) 500 cycles

(b) 15,000 cycles

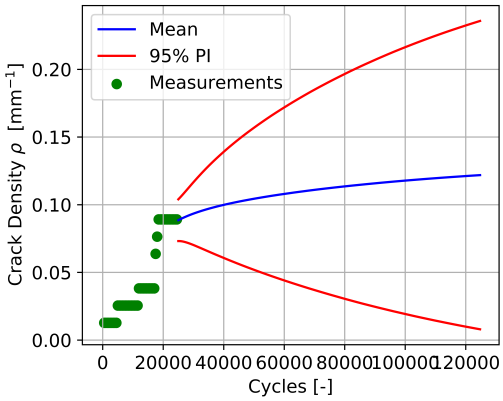

(c) 25,000 cycles

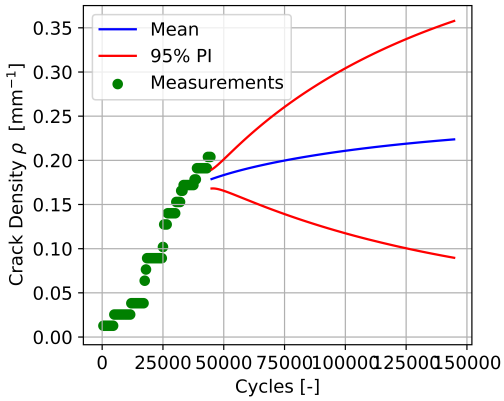

(d) 45,000 cycles

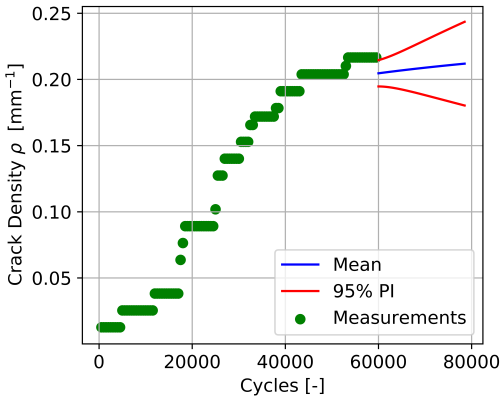

(e) 60,000 cycles

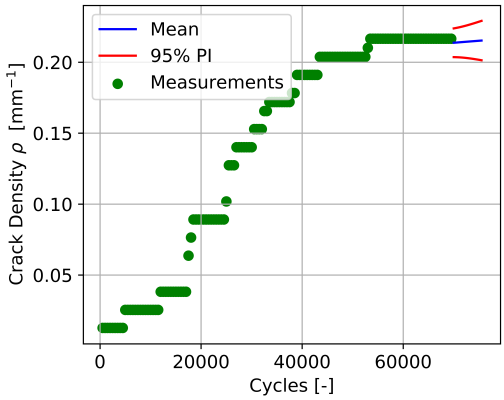

(f) 70,000 cycles

Figure A.10: Results of the prognostics at distinct cycles of the transverse matrix crack density ρ for specimen 2-1 with indicative weighted mean and 95% prediction interval (PI) of the N_s particles.

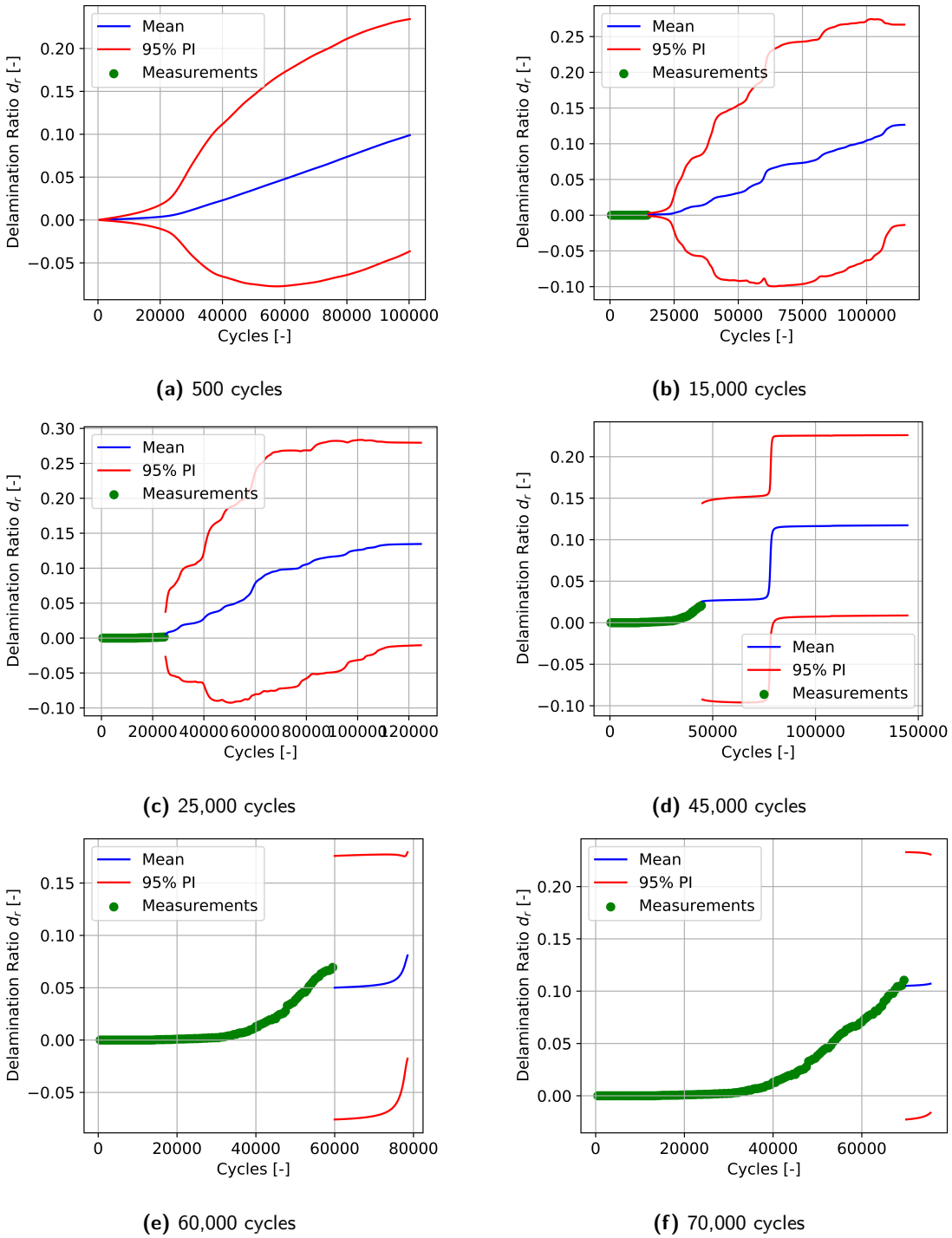

(a) 500 cycles

(b) 15,000 cycles

(c) 25,000 cycles

(d) 45,000 cycles

(e) 60,000 cycles

(f) 70,000 cycles

Figure A.11: Results of the prognostics at distinct cycles of the delamination ratio d_r for specimen 2-1 with indicative weighted mean and 95% prediction interval (PI) of the N_s particles.

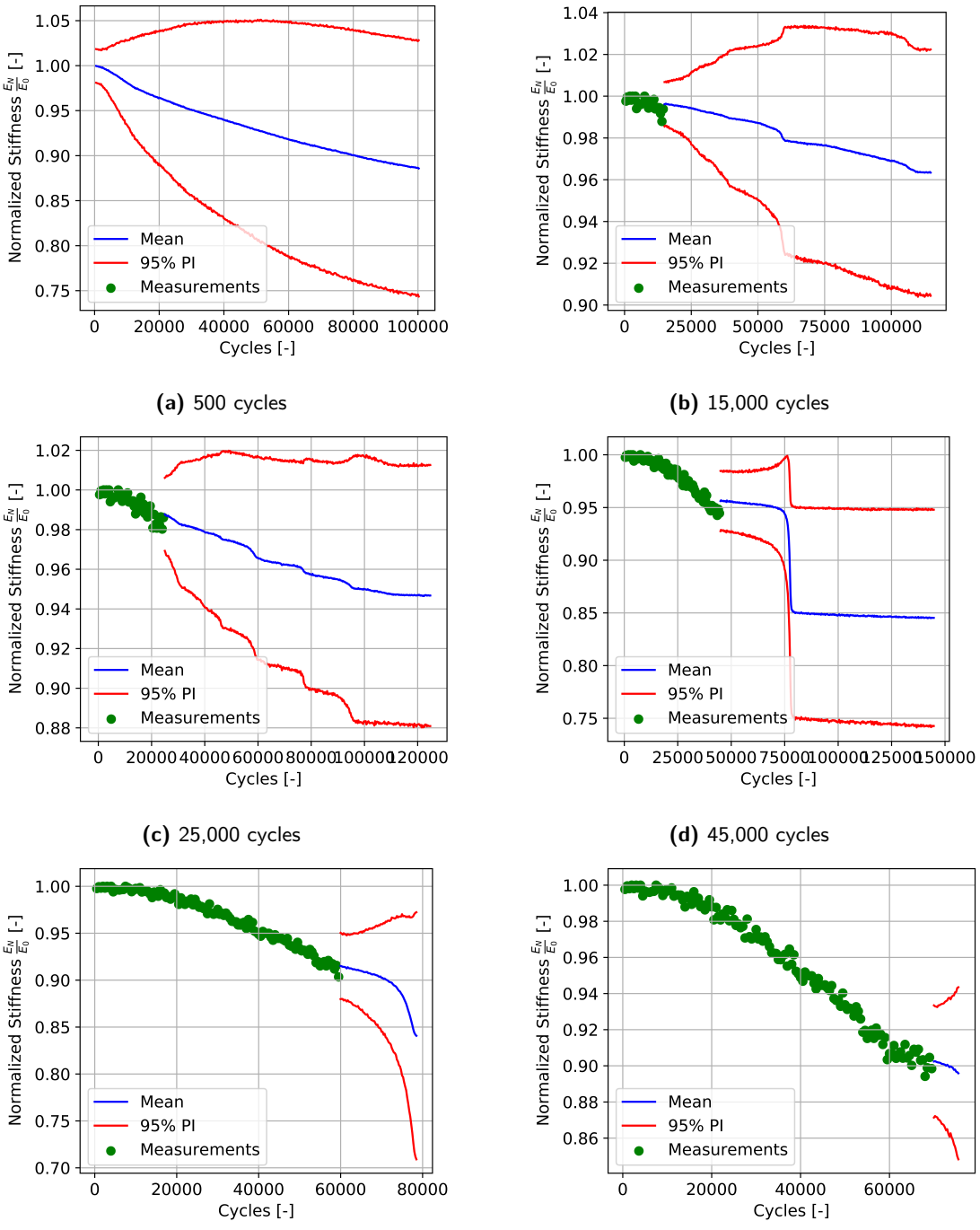

(a) 500 cycles

(b) 15,000 cycles

(c) 25,000 cycles

(d) 45,000 cycles

(e) 60,000 cycles

(f) 70,000 cycles

Figure A.12: Results of the prognostics at distinct cycles of the normalized stiffness $\frac{E_N}{E_0}$ for specimen 2-1 with indicative weighted mean and 95% prediction interval (PI) of the N_s particles.

A.5 Specimen 2-3

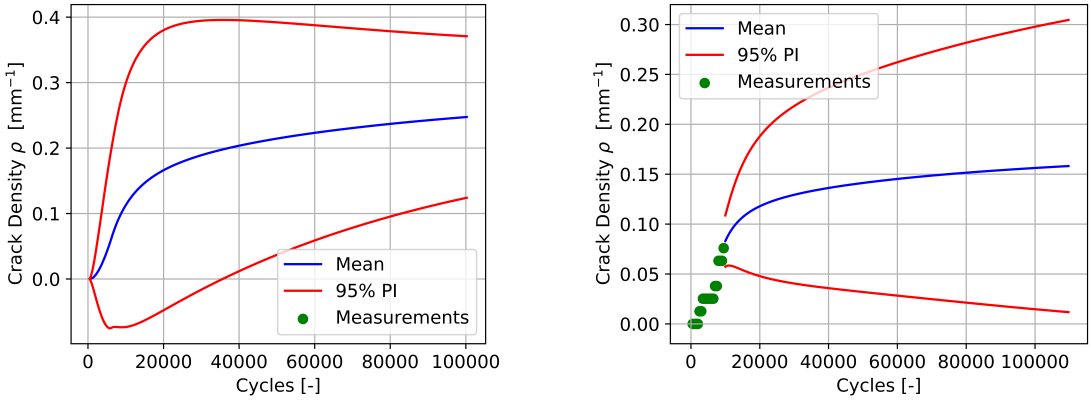

(a) 500 cycles

(b) 10,000 cycles

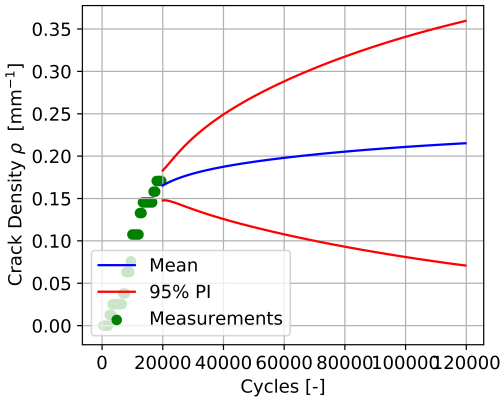

(c) 20,000 cycles

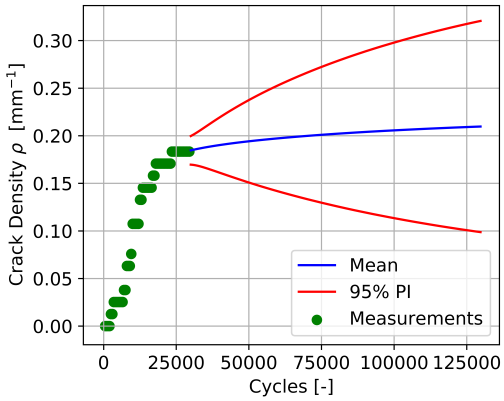

(d) 30,000 cycles

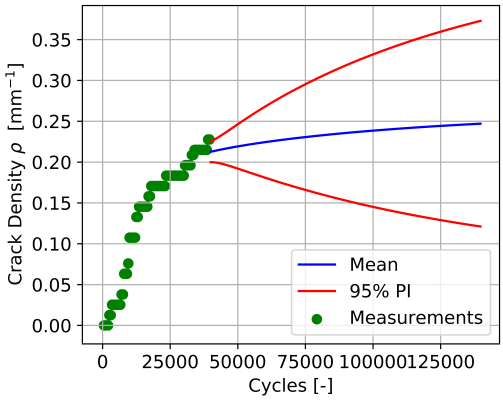

(e) 40,000 cycles

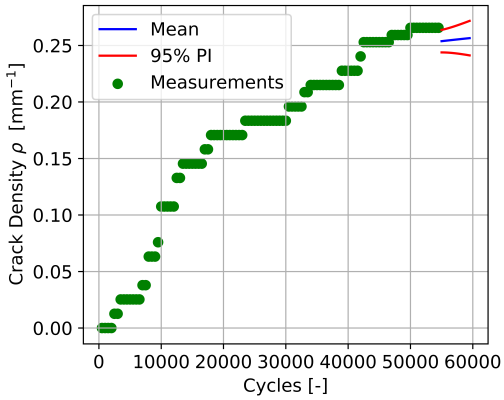

(f) 55,000 cycles

Figure A.13: Results of the prognostics at distinct cycles of the transverse matrix crack density ρ for specimen 2-3 with indicative weighted mean and 95% prediction interval (PI) of the N_s particles.

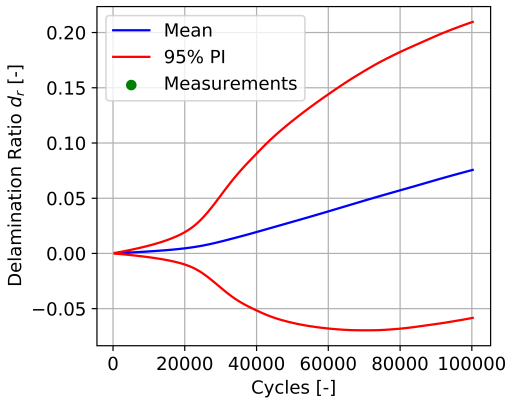

(a) 500 cycles

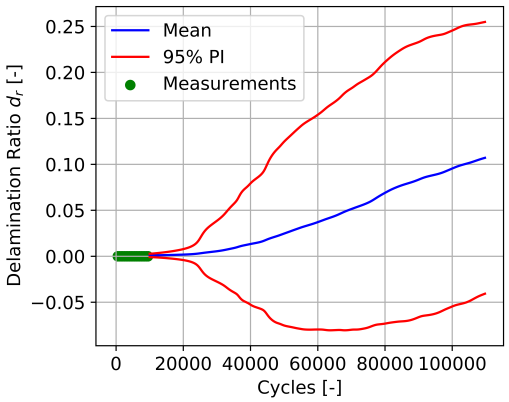

(b) 10,000 cycles

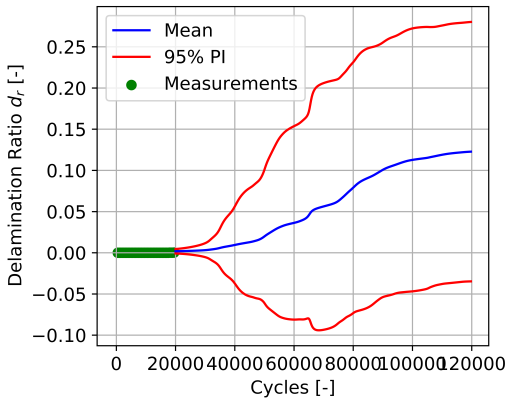

(c) 20,000 cycles

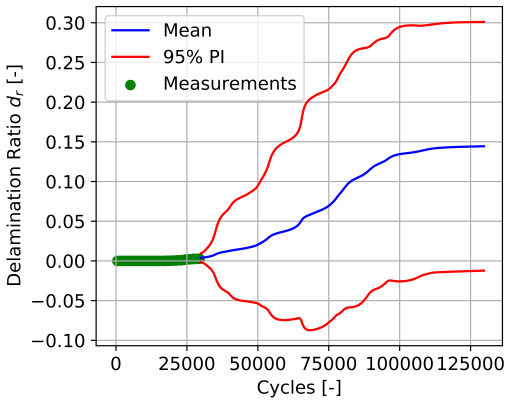

(d) 30,000 cycles

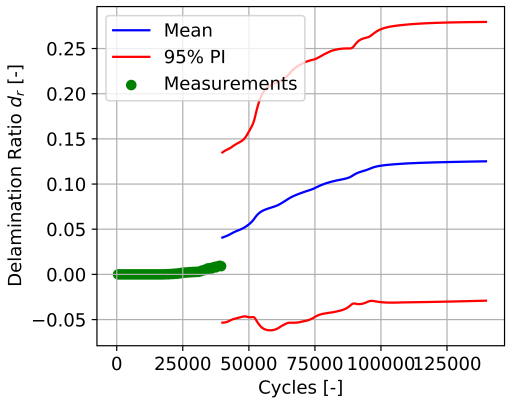

(e) 40,000 cycles

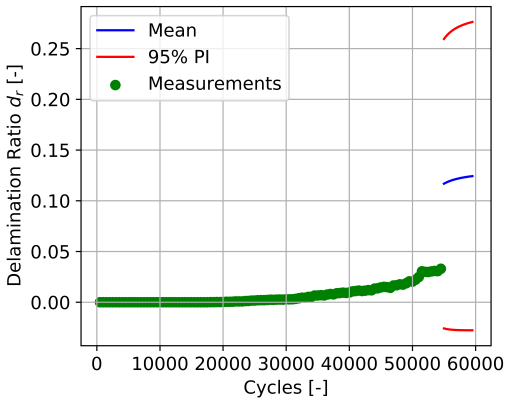

(f) 55,000 cycles

Figure A.14: Results of the prognostics at distinct cycles of the delamination ratio d_r for specimen 2-3 with indicative weighted mean and 95% prediction interval (PI) of the N_s particles.

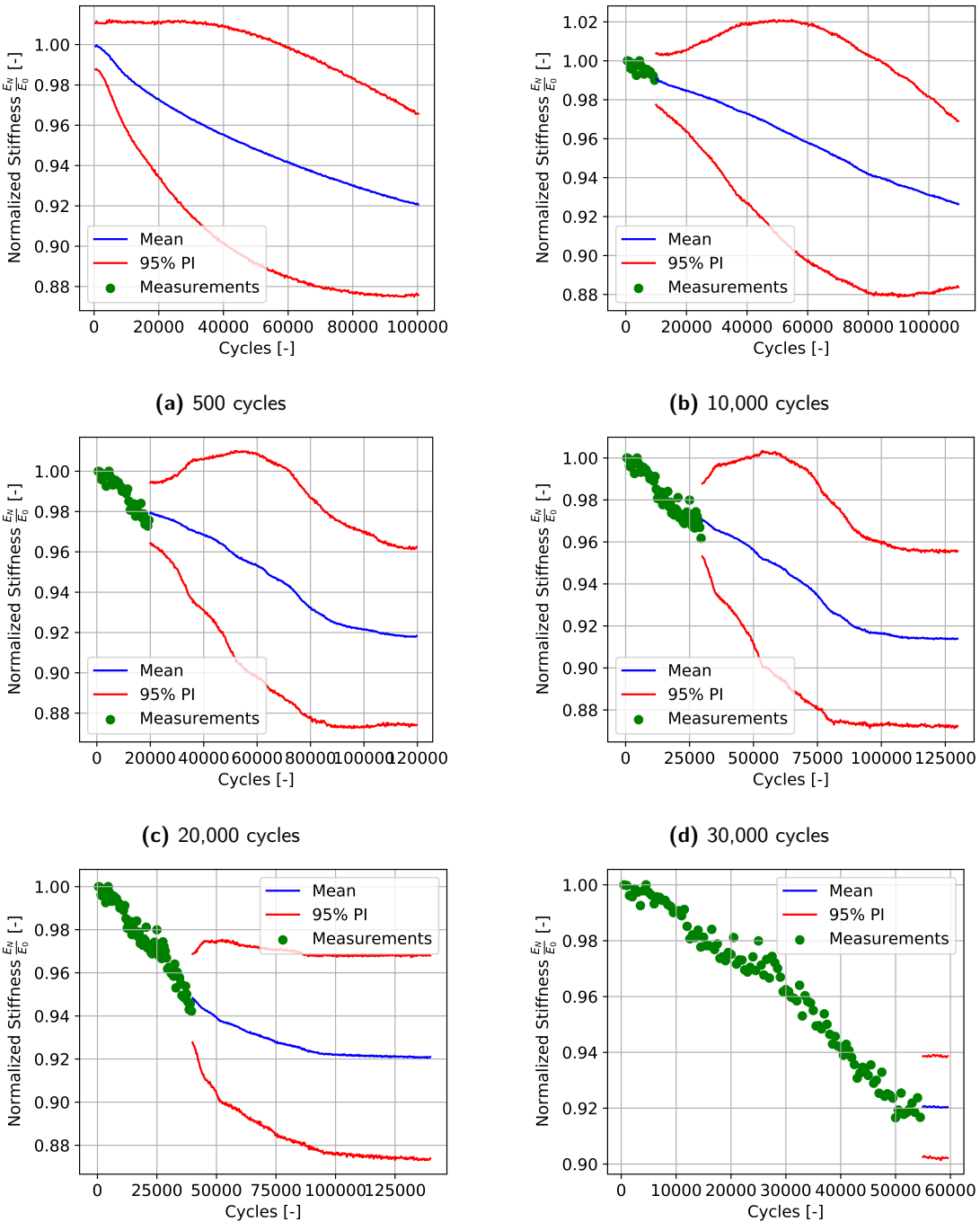

(a) 500 cycles

(b) 10,000 cycles

(c) 20,000 cycles

(d) 30,000 cycles

(e) 40,000 cycles

(f) 55,000 cycles

Figure A.15: Results of the prognostics at distinct cycles of the normalized stiffness $\frac{E_N}{E_0}$ for specimen 2-3 with indicative weighted mean and 95% prediction interval (PI) of the N_s particles.